PSFC/RR-98-3 DOE/ET-51013-328

Fast Ion Tails during Radio Frequency Heating on the Alcator C-Mod Tokamak

Rost, J.C.

April 1998

Plasma Science and Fusion Center
Massachusetts Institute of Technology
Cambridge, MA 02139 USA

This work was supported by the U.S. Department of Energy, Contract No. DE-AC02-78ET51013. Reproduction, translation, publication, use, and disposal, in whole or in part, by or for the United States government is permitted.

Fast Ion Tails during Radio Frequency Heating on the Alcator C-Mod Tokamak

by

Jon Christian Rost

B.S., Physics
B.S., Electrical Engineering
University of Maryland, College Park, 1991

Submitted to the Department of Physics in Partial Fulfillment of the Requirements for the Degree of

Doctor of Philosophy in Physics

at the

Massachusetts Institute of Technology

June 1998

Signature of Author: _____

Department of Physics
April 10, 1998

Certified by: _____

Miklos Porkolab
Professor of Physics
Thesis Supervisor

Accepted by: _____

Thomas J. Greytak
Associate Department Head for Education

Fast Ion Tails during Radio Frequency Heating on the Alcator C-Mod Tokamak

by

Jon Christian Rost

Submitted to the Department of Physics
on April 10, 1998 in Partial Fulfillment of the
Requirements for the Degree of
Doctor of Philosophy in Physics

Abstract

Observations of ion tails in the plasma edge during radio frequency heating on the Alcator C-Mod tokamak have been made using a toroidally and poloidally scanning charge-exchange neutral particle analyzer. The ion tails create a large flux of charge-exchange neutrals (hydrogen and deuterium) at suprathermal energies. The neutral particle flux is characterized by: fast rise and decay times, much faster than the time for changes in the bulk plasma; dependence on plasma conditions and magnetic field in the scrape-off layer; a threshold in electric field near the antenna; and no correlation with bulk plasma parameters. During hydrogen minority heating, edge ion heating may occur at power levels above approximately 500 kW. When the heating frequency is at an ion cyclotron harmonic in the edge, edge heating occurs at power levels lower than 10 kW. Dedicated experiments showed that edge ion heating does not generate impurities or cause loss of heating efficiency. Using the pitch-angle dependence of the fast particles, the total parasitic power loss to the edge is estimated at less than 0.1% during standard heating schemes, but up to 5% with a cyclotron resonance in the edge.

Evidence of Parametric Decay Instability (PDI) into an ion Bernstein wave and an ion cyclotron quasimode has been found on C-Mod using RF probes. Calculations of convective thresholds for PDI have been made for a range of edge parameters and magnetic fields. Calculated theoretical thresholds for PDI in the antenna near field are consistent with experimentally observed thresholds for edge heating, and observed dependence on toroidal field and changes at H-mode transitions.

Thesis Supervisor: Miklos Porkolab
Title: Professor of Physics

Acknowledgements

I would first like to thank Professor Miklos Porkolab, who was my research advisor for four years. His classes in plasma physics formed the foundation of my knowledge of waves in plasmas. Most importantly, he interceded at a difficult time for me, probably saving my graduate career and giving me the opportunity to work with him and the Alcator Group.

Dr. Réjean Boivin worked closely with me throughout my time on Alcator. He had nearly completed the PCX diagnostic when I arrived at Alcator, and all of the data used in this thesis was acquired and analyzed with his help. He taught me a lot about how to be an effective experimental physicist. Réjean also spent uncountable hours working with me on my thesis, and helping me organize posters and talks. He was the one who was there on a day-to-day basis to discuss the results from the most recent data, analysis, or calculation, or just my problems navigating the waters of graduate school.

This thesis would not exist today if I had not had the help of these two men.

The RF probe data were taken with probes built and operated by my fellow graduate student and good friend, James Christian Reardon.

The intelligence and hard work of the members of the Alcator Group never ceased to amaze me. I think Alcator will forever define for me the standard for how physics should be done. I also appreciate the unique level of support Alcator gives to graduate students in machine time and equipment.

The advice and enthusiasm of Dr. Robert Pinsker helped immensely in planning, running, and interpreting these experiments.

I cannot begin to list the other friends who have been with me during my time through graduate school, giving me a life outside the lab.

I must finally thank my parents who have always supported my decisions about what path to take in life.

Contents

Chapter 1

Introduction

This thesis describes the exploration of a phenomenon observed during ion cyclotron resonance frequency (ICRF) heating on the Alcator C-Mod tokamak. Measurements with a neutral particle analyzer showed the presence of ions with energy far above the thermal level in the plasma edge during RF heating. These fast ions are an unwanted side-effect of the RF heating. This work examines the effect the suprathermal edge ions have on the tokamak plasma and explains their source through the theory of a non-linear interaction between the plasma and the RF wave.

1.1 Ion Cyclotron Resonance Frequency Heating on Tokamaks

To the extent the that goal of tokamak research is to achieve a functioning fusion reactor[1], ion cyclotron resonance frequency heating is a critical part of the field. A reactor is expected to require a source of heating beyond the resistive heating from the plasma current, and possibly a means to control the distribution of particles and current in the plasma[2]. The two dominant methods of auxiliary heating are neutral beam injection[3] and ICRF heating[2], though electron cyclotron resonance heating

is also being developed. These methods are capable of coupling large amounts of power to the plasma, and each has its advantages and disadvantages.

On the Alcator C-Mod tokamak, several ICRF heating schemes are employed[4]. The goal of RF heating is to launch an RF wave from outside the plasma which penetrates to the plasma interior and is absorbed on either the ion or electron population.

There is a gap between the RF antenna and the plasma where the electromagnetic wave is evanescent. To reach the plasma interior, the RF power must cross this gap[5]. Various phenomena in the plasma edge can reduce the RF power to the plasma interior by absorption in the edge or by decreasing the coupling from the antenna to the plasma[6]. If RF power is absorbed in the edge, energy from the RF fields is transferred to ions or electrons. If the coupling is decreased, then more RF power is reflected from the antenna back into the RF transmission line.

1.2 The Alcator C-Mod Neutral Particle Analyzer

This work centers around measurements made by the neutral particle analyzer (NPA) on Alcator C-Mod. The neutrals observed result from charge exchange reactions and actually represent, in an indirect way, the velocity distribution of hydrogenic ions along the sight line.

Neutral particle analyzers are in general used to measure the ion temperature and distribution function in the plasma center, particularly during ICRF or neutral beam heating[7].

When the NPA was installed on Alcator C-Mod, with the intention of monitoring the central ion heating, it was found that the signals changed much too fast during ICRF heating to represent central heating, and that the apparent temperature implied by the signals was not consistent with results from other diagnostics.

We realized that this data represented an interaction between the RF heating

wave and the plasma edge, and that it was important to determine all the effects the edge heating may have on the plasma and to understand what mechanism was generating the fast ions.

1.3 Edge Ion Heating

The edge ion heating observed on Alcator C-Mod is characterized by a large increase in the flux of neutral particles with energies above a few keV. The increase occurs when the ICRF power is applied, and is much faster than other changes in the plasma. The edge heating has a threshold in RF electric field, which is sensitive to changes in temperature, density, and magnetic field in the plasma edge. The data suggest that the edge heating occurs in the near field of the RF antenna in the outer scrape-off layer of the plasma.

Ion edge heating in Alcator does not generate impurities, and does not affect the coupling of RF heating power to the plasma. The total power absorbed by the edge through this mechanism is at most a few percent.

1.4 Parametric Decay Instability

RF probe spectra typical of parametric decay instability (PDI)[8] have been observed during RF heating on C-Mod. The RF electric field threshold for decay into an ion cyclotron quasimode and an ion Bernstein wave have been calculated for C-Mod edge plasmas. The change in observed edge ion heating at different parameters is consistent with predictions of PDI theory, particularly the dependence on the magnetic field in the edge.

1.5 Outline of this Work

Throughout this thesis, two threads are, by necessity, intertwined. The first is the study of the effects edge ion heating has on the plasma, and the second is the search for a mechanism responsible for edge heating. Because certain topics, such as particle dynamics, are relevant to several parts in this work, topics are grouped thematically: Alcator C-Mod and its diagnostics; particle dynamics and confinement; observations; causes of edge heating.

More specifically, Chapter 2 of this thesis describes the basic operation of Alcator C-Mod including the details of diagnostics and systems that are specifically referred to later. The data from the neutral particle analyzer, covered in Chapter 3, is the basis of this work. Chapter 4 presents dynamics of fast particles in the plasma edge, focusing on energy and pitch-angle ranges of interest with respect to the energetic edge ions. In Chapter 5, we review observations of fast ions in the plasma edge during ICRF heating that have been made on other tokamaks. The various measurements of edge ion heating and its effects that have been made on Alcator C-Mod are described in Chapter 6. In Chapter 7, the various mechanisms that can produce suprathermal ions in the edge are considered. A brief introduction to parametric decay, the methods and results of calculations, and their correspondence to the data are found in Chapter 8. In Chapter 9, we summarize the work and draw conclusions.

Units and Conventions

All equations are expressed in the MKS system. Temperatures are assumed to include the Boltzmann constant, so T in an equation is a value expressed in joules. In text only, plasma temperatures are given in electronvolts (eV), as is customary in plasma physics.

Unit vectors are represented by a "hat". For example $\hat{x}$ is the unit vector in the x direction.

Chapter 2

Plasma operation on Alcator C-Mod

2.1 Sample Alcator C-Mod Shot

The magnetic geometry and basic operation of the tokamak are well known[9]. Data from a fiducial, shot 960207004[1], is included as representative of Alcator data to show typical time evolution of a shot and typical radial profiles. Discharges with a particular set of controlled plasma parameters are frequently repeated to monitor machine conditions; these shots are called fiducials. Fiducials use ICRF heating in the hydrogen minority regime at $B_0 = 5.3$ T. Figure 2.1 shows the time history of several important plasma parameters during the plasma shot. Time zero is when the toroidal electric field that drives the plasma current starts; the plasma begins to form within a few milliseconds after. From 0.5 to 1.1 s, the plasma is completely formed and parameters are stable; this period of time is the "flat-top". The ICRF heating is turned on at 0.79 s, and central ion temperature starts to rise. At approximately 0.84 s, the plasma enters a regime of improved energy and particle confinement, called

[1]The number of an Alcator discharge shows the date of the run, and which shot that day. 960207004 is the fourth shot on Feb. 7, 1996.

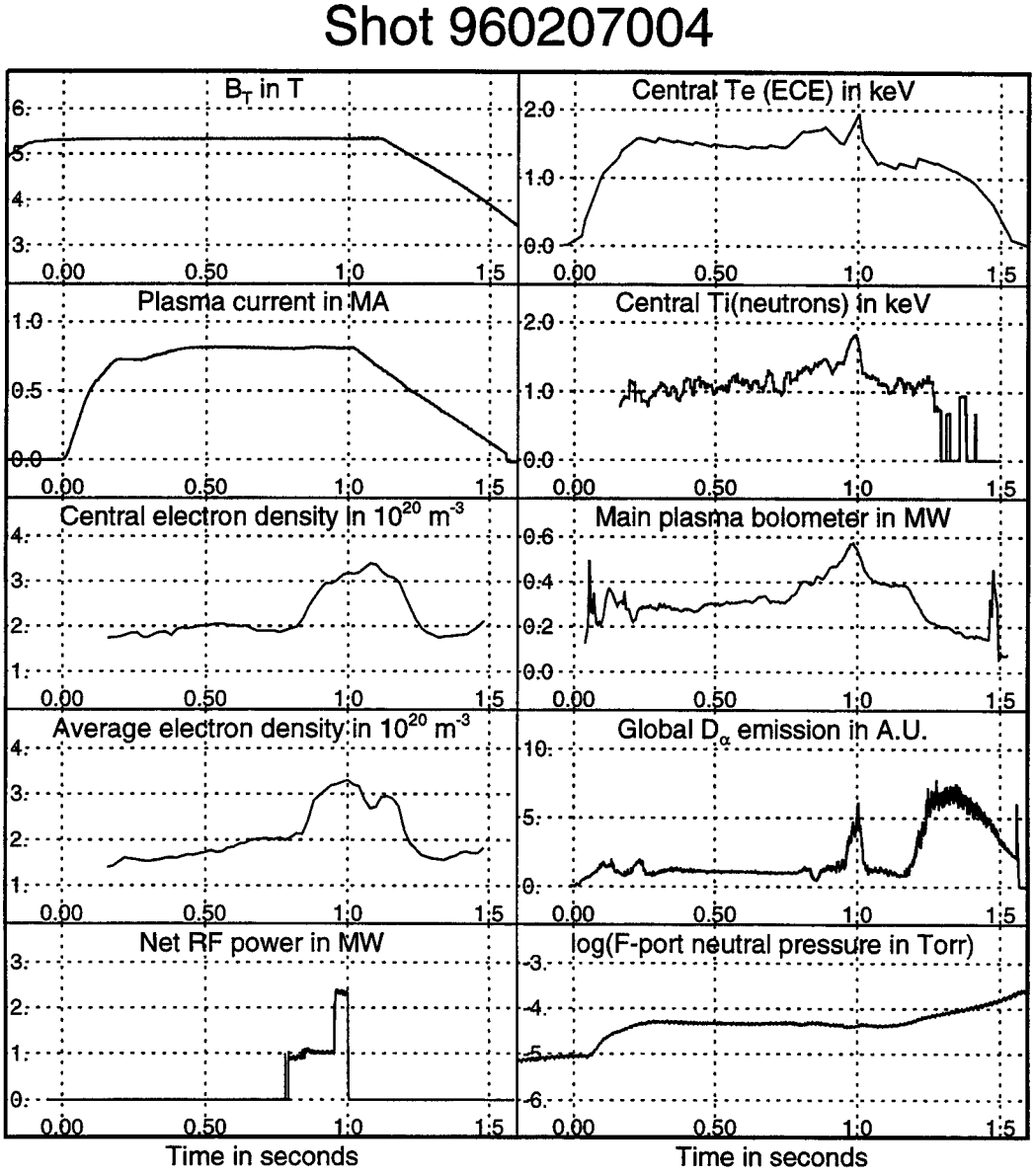

Figure 2.1: Time series data from fiducial, shot 960207004.

"H-mode". The confinement regime observed before 0.84 s is referred to as "L-mode". Because of the improved confinement, the plasma density and temperature increase. The level of impurities in the plasma also increases, as is shown by the increase in power emission detected by the bolometer array. The plasma current and the B_0 are ramped down starting at 1.0 s and 1.1 s, respectively.

Figure 2.2 shows midplane profiles of a few of the plasma parameters. The two vertical dotted lines show the location of the plasma center, at $R = 0.682$ m, and the last closed flux surface (LCFS), at $R = 0.890$ m. It can be seen that the current and electron temperature are sharply peaked, while the density is fairly flat. The plasma edge is much colder than the center, but the density at the edge is within a factor of two of that at the center. Edge parameters change with a much smaller scale length. Typical electron density and temperature outside the LCFS are shown in Fig. 2.3, taken from fast scanning probe data[10].

The flux surfaces of this plasma are plotted in Fig. 2.4. The plasma is fully diverted, with a single lower null. The poloidal limiters are represented as the right-hand side of the vessel on the drawing. These limiters are between F and G ports, and between A and B. The flux surfaces are reconstructed by the EFIT code[11] using data from magnetic pickup coils outside the plasma. The last closed flux surface (LCFS) is the outermost flux surface that does not intersect a material surface. The region outside this, excluding the divertor, is the scrape off layer (SOL).

Figure 2.5 shows a top view of the machine showing the limiters and port lettering system. Figure 2.6 shows the relative position of the RF antennas, the PCX, and the limiters.

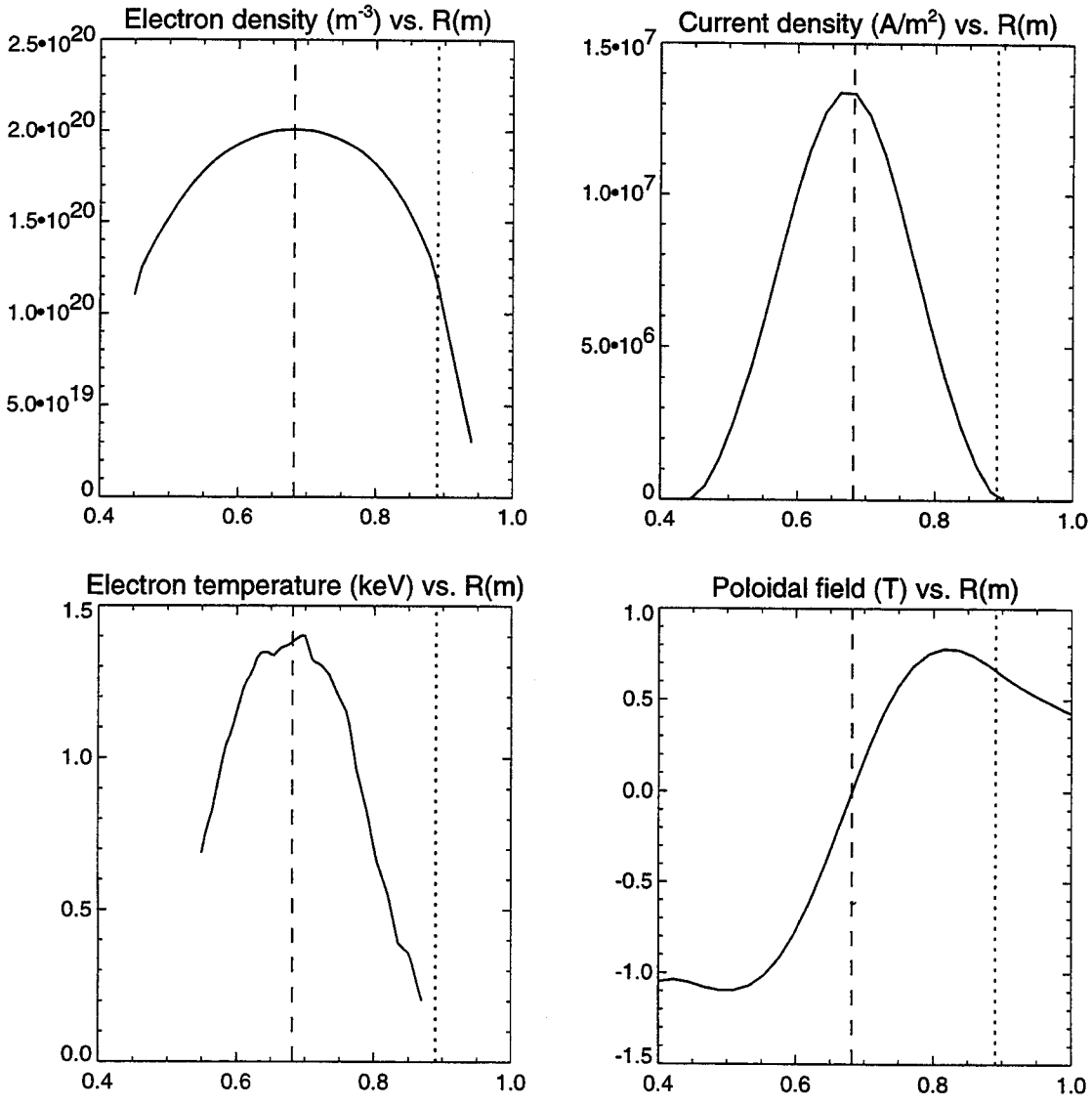

Figure 2.2: Midplane profile data from a fiducial, shot 960207004. Dashed line represents position of the magnetic axis; dotted line shows position of last closed flux surface.

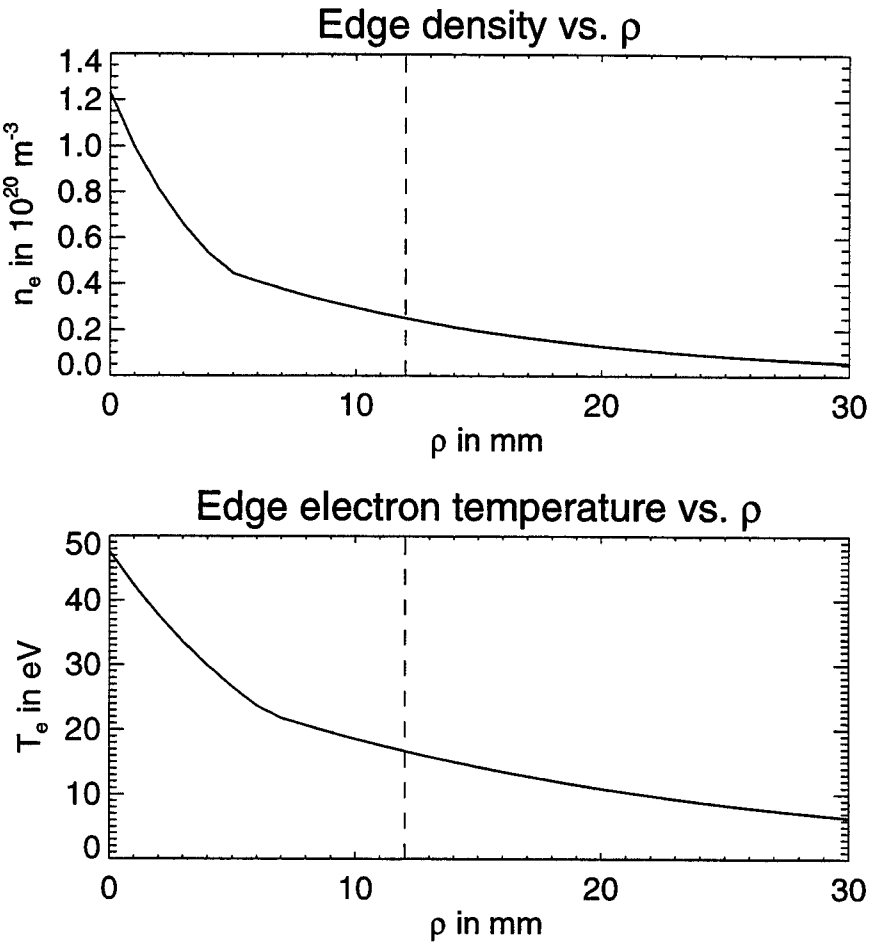

Figure 2.3: Midplane electron density and temperature profiles outside the LCFS. $\rho = 0$ corresponds to the LCFS. Dotted line shows location of the limiter. Profiles are fits to data taken by the fast scanning probe.

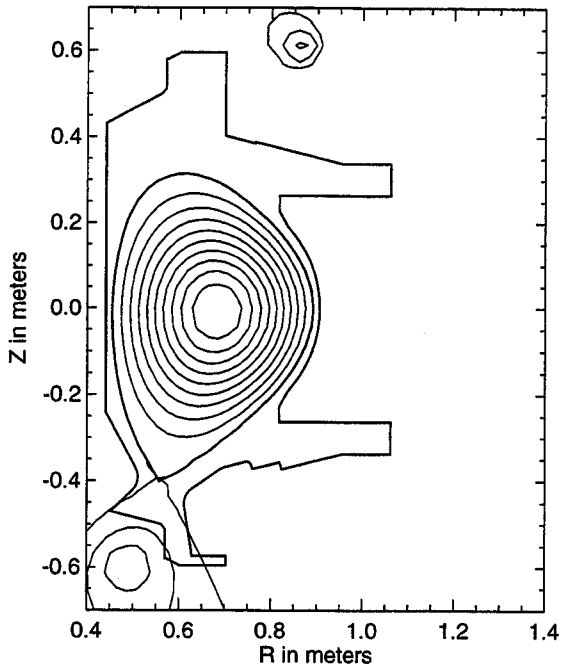

Figure 2.4: Flux surfaces from shot 960207004

2.2 Radio-frequency Heating

On Alcator C-Mod, up to 3.5 MW of RF power in the fast wave at 80 MHz is routinely used as auxiliary plasma heating[4]. This is in addition to the ohmic heating from the plasma current, which is in general on the order of 1 MW.

2.2.1 Heating Schemes

Both electron and ion heating schemes have been used on Alcator C-Mod[4].

During minority ion heating, the fundamental cyclotron resonance of the minority species is placed in the center of the plasma. In deuterium majority plasmas, minority heating of H at 5.3 T and ^{3}He at 8 T has been performed. During H-minority heating at 5.3 T with the cyclotron resonance at the plasma center, greater than 80% of the RF power is absorbed by the plasma. Ion heating can also occur when the minority

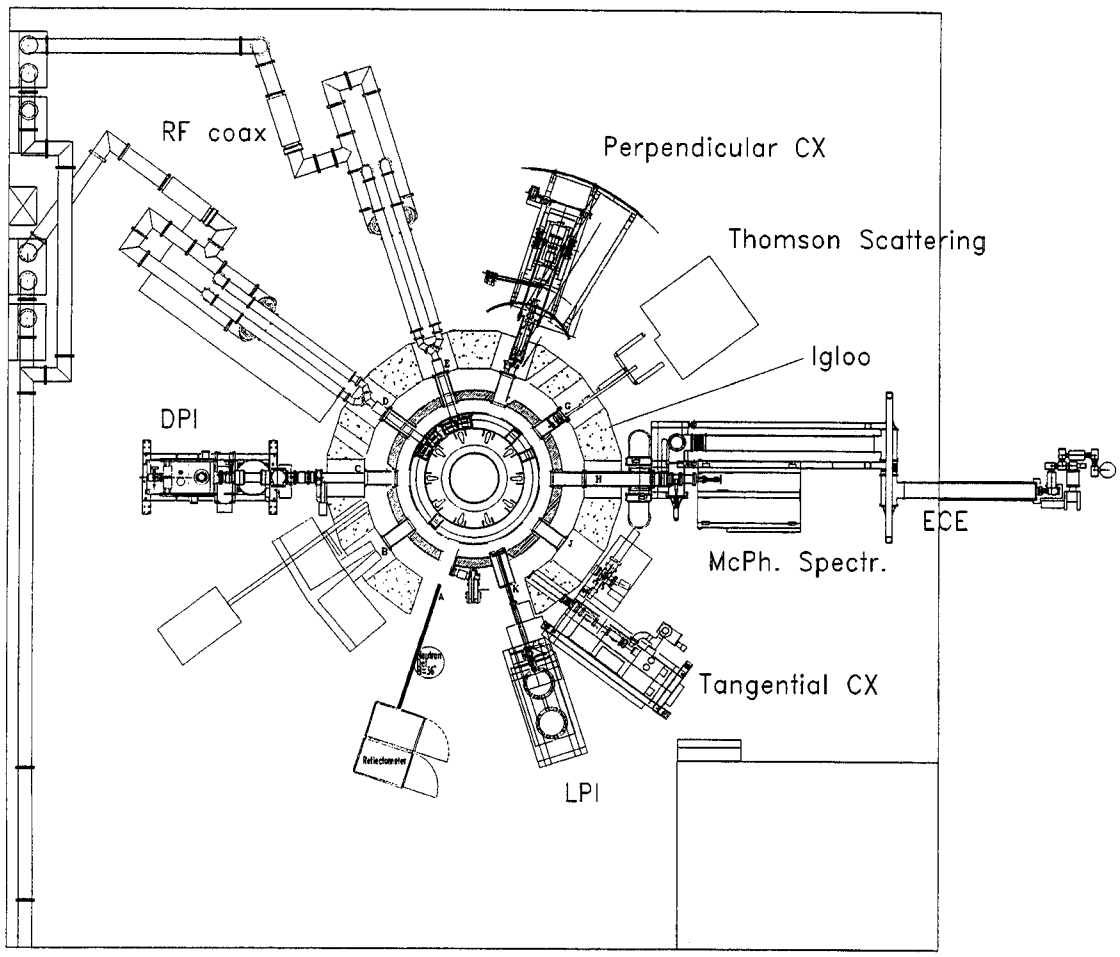

Figure 2.5: Top view of Alcator C-Mod cell, showing positions of RF system, neutral particle analyzer, and other diagnostics

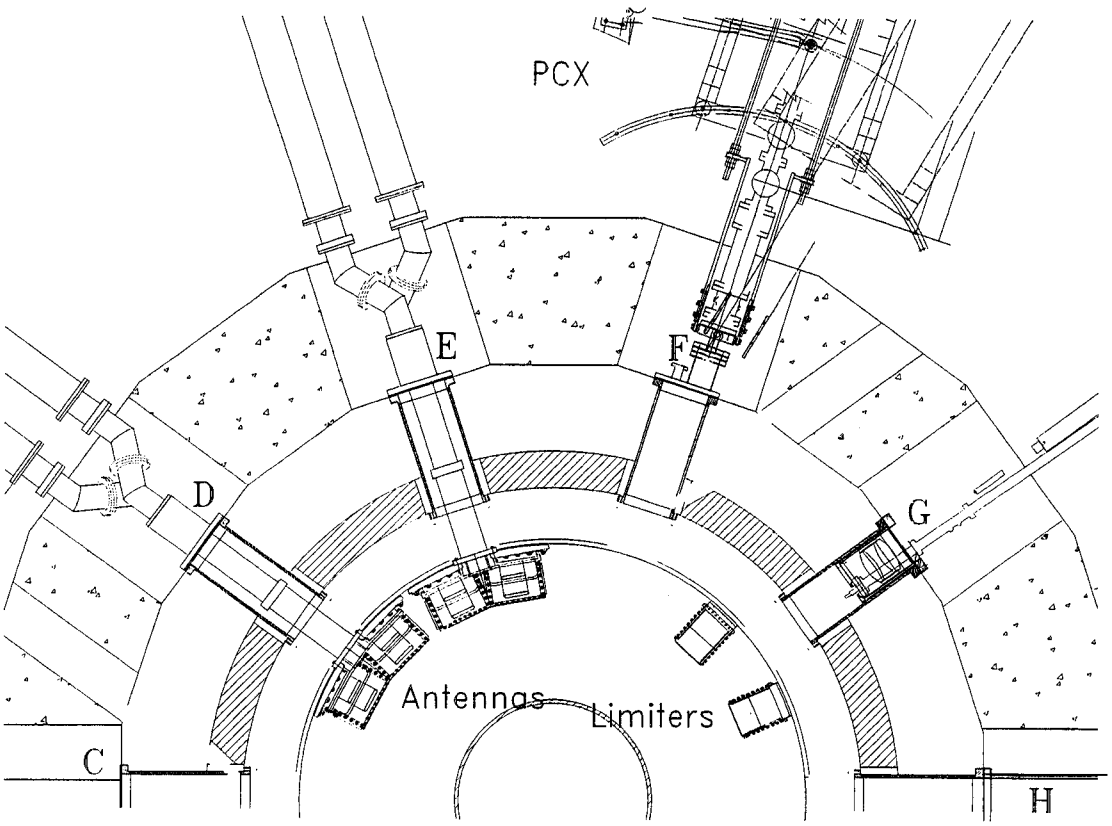

Figure 2.6: Top view of Alcator C-Mod, showing antennas, limiters, PCX sight line, and showing port lettering system

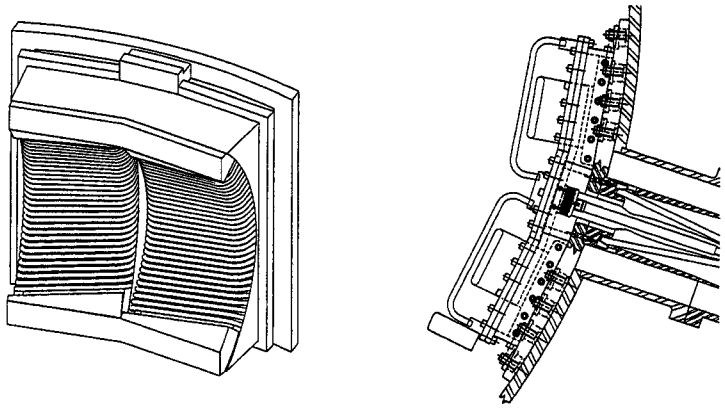

Figure 2.7: Double-strap RF antenna: Left figure shows Faraday shield. Right figure is a top view, showing current strap, Faraday screen, and protection tiles.

second harmonic is in the plasma, for example at 2.6 T with a hydrogen minority.

2.2.2 Antenna

There are two RF antennas on C-Mod, one in D-port and one in E-port. Drawings of the antenna in E port are shown in Fig. 2.7. Their centers are 0.57 m apart toroidally. Each antenna consists of two current straps, grounded at the center, fed out of phase at the ends. The straps are 0.102 m wide, and have a vertical extent of 0.416 m. The separation of the straps, 0.284 m, sets the dominant $k_{||}$ of the spectrum of power launched. The straps are curved to closely conform to the outer edge of the plasma. The two antennas are driven at frequencies that differ by 0.5 MHz in order to eliminate interaction between them.

Both antennas have Faraday shields, consisting of rods 9.5 mm in diameter, offset from horizontal by 10° to be approximately parallel to the magnetic field. The rods are separated by 3.4 mm, and are covered with a non-conductive coating. The rods are 7.9 mm in front of the current strap. The purpose of the Faraday screen is to shield components of the RF electric field parallel to the total magnetic field, and to protect the surface of the current strap from photons and energetic atoms and ions

from the plasma.

There are antenna protection tiles on the sides of the antennas that project 5 mm beyond the rods in the Faraday screen.

These tiles in turn are 5 mm behind the RF protection limiters, poloidal limiters located between G and H ports and between A and B port on the outboard side. In general, the gap between the LCFS and the limiters is from 5 to 15 mm.

Combining these measurements, the surface of the Faraday screen is approximately 20 mm from the LCFS, and the surface of the current strap is approximately 40 mm from the LCFS.

Directional couplers measure the power delivered to the antennas, and the power reflected. The difference between these is the total power radiated by the antenna. The fields in the coax that delivers the RF power from the transmitters to the antennas are measured by probes. Using these two quantities it is possible to calculate the current in the current straps and the loading resistance of the antenna. These measurements are made throughout every shot with a time resolution of 0.10 ms.

2.2.3 RF Fields in the Plasma Edge

The purpose of the antenna is to couple RF power into the center of the plasma, where it propagates as a fast wave[12] toward a cyclotron resonance or mode conversion layer. RF waves at 80 MHz have vacuum wavelengths too long to propagate inside the Alcator C-Mod vacuum vessel.

In studying nonlinear effects, it is necessary to know the magnitude of the electric field in various regions. There are no measurements, but the wave magnitude can be estimated using known quantities: the RF power flux and the fast wave dispersion relation. Details are in Appendix A. At 500 kW of injected RF power, we find that the electric field in the propagating part of the heating wave is approximately 12 kV/m in the plasma.

The fields from the antenna near fields are much larger than the fields due to the propagating part of the wave, however. The near field is due to the self-inductance of the antenna, and is not directly related to the power coupled to the plasma. Diagnostics in the antenna coax measure the maximum voltage in the transmission line, which is approximately equal to the voltage at the top of the antenna. For a 500 kW shot, the voltage from the top of the antenna to the center is around 25 kV. If the voltage in the current strap were uniform, then the vertical electric field would be approximately 120 kV/m. This is the best estimate that can be obtained without extensive modeling of the antenna, Faraday shield, and plasma. Since the field falls off on scale lengths much shorter than the antenna height, the near field of the current strap is similar to that of an infinite bar. The field should be approximately constant from the surface of the strap to 50 mm away, and then fall off like $\ln H/d$ where d is the distance from the current strap and H is the antenna height.

The Faraday screen causes even stronger fields in its vicinity[13][14]. The vertical electric field is shorted out inside the rod, and intensified between the rods. Since the rods are 9.5 mm thick, separated by 3.4 mm, the field between the rods is larger than the average field by a factor of $(9.5+3.4)/3.4 = 3.8$. An average vertical field of 120 kV/m leads to a field of 456 kV/m between the rods. This falls off to the average field in a distance on the order of the gap between the rods, 3.4 mm.

The approximate midplane profile of the electric near field is shown in Fig. 2.8. The details of this calculation are in Appendix C. As discussed there, the screening of the electric field by the plasma can be neglected in calculating the poloidal RF electric field in the SOL.

At 500 kW the electric near field of the current strap is about ten times larger than the field in the propagating wave, and the field near the Faraday screen is four times larger than that. This means that various interactions between particles in the edge and the RF power will be much stronger in the vicinity of the antennas.

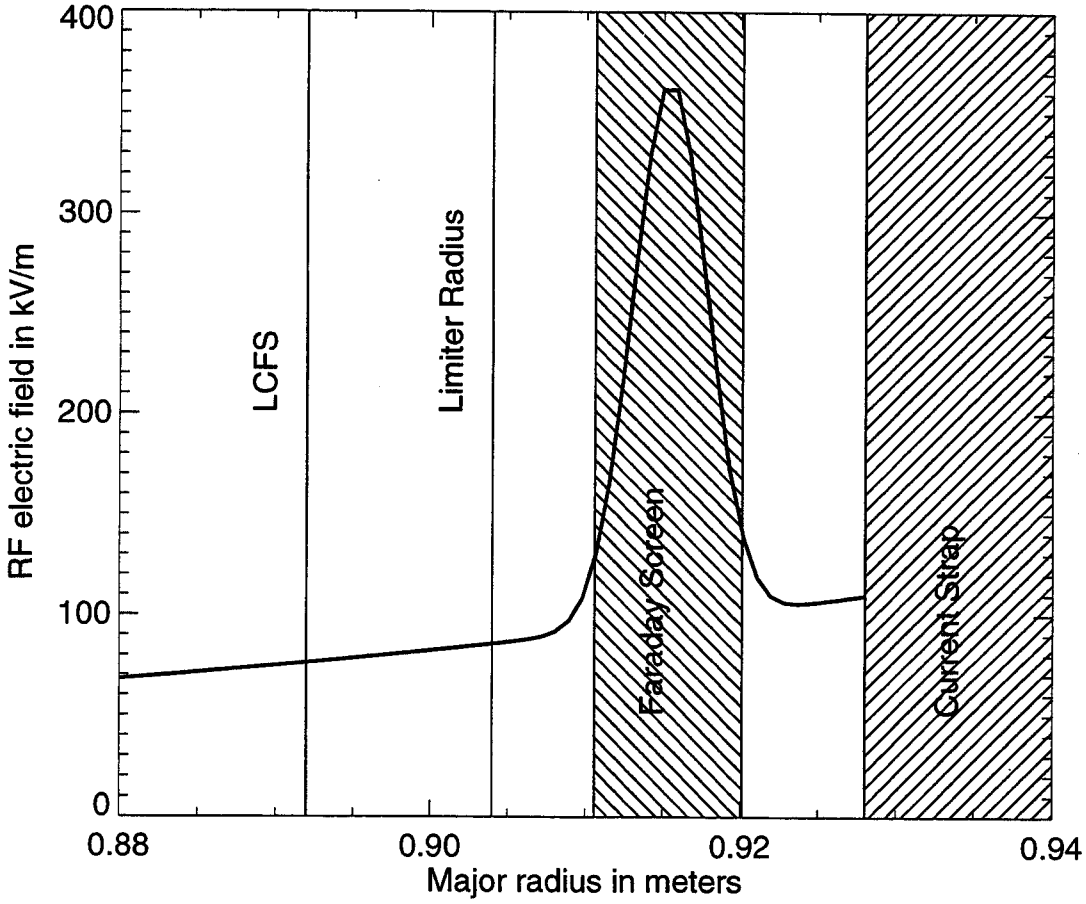

Figure 2.8: Midplane profile of RF electric field near the antenna.

However, if the antenna is putting power into global surface modes or propagating waves other than the fast wave, fields far from the antenna could be larger than estimated above[15].

2.3 Diagnostics

2.3.1 General diagnostics

As a world-class tokamak experiment in regular operation, Alcator C-Mod has an extensive array of diagnostics[16]. Many of these diagnostics are a necessary part of the control systems that operate the tokamak and shape and control the plasma. They also allow comparison of plasmas to monitor reproducibility. These core diagnostics include an interferometer for measuring electron density profiles[17], a Michelson interferometer measuring electron cyclotron emission to determine electron temperature profiles, and magnetic pickup coils to find the plasma position and shape. Ion temperature is calculated from neutron emission by the plasma, and spectroscopically.

2.3.2 RF Probes

RF probes are used to measure the propagation of the ICRF heating wave and observe a variety of nonlinear phenomena that can occur.

There are RF probes throughout the machine. There are two types. The "B-dot" probes consist of a pair of loops. The signal from these is $V = -NA\frac{d\vec{B}}{dt} \cdot \hat{n}$, where N is the number of loops of area A, and $\hat{n}$ is normal to the area. The probes are shielded from the plasma and wired like humbuckers to further prevent pickup of the electric component of waves. There are also Langmuir probes that are effective at radio frequencies to measure the electric component of RF waves. They are unbiased, and the voltage on them is measured directly. The tips of these probes are tungsten, and extend 2.5 mm beyond the molybdenum housing.

There are fixed Langmuir probes on the A-B limiter and the G-H limiter, above and below the midplane. There are fixed loop probes on the antennas behind the current straps. There are three sets of movable probes. In J-port, there are two probe heads with a total of 3 Langmuir probes, 2 B-dot probes normal to the poloidal direction, and 2 B-dot probes normal to the toroidal direction. These probes are 0.11 meters below the midplane and move horizontally. They are positioned within approximately 10 mm of the limiter radius. There is a probe head with 4 Langmuir probes mounted on the A-top port. It is at a major radius of 0.735 m. In A-port there is a probe with 4 Langmuir probes. It is situated 0.10 m above the midplane, and scans horizontally. Additionally, this probe can be scanned in and out during a shot, measuring a profile. The scan takes about 20 ms.

Signals from these probes are digitized by fast digitizers or a spectrum analyzer. The fast digitizers can be operated at a sampling rate up to 1 GHz. The spectrum analyzer can be run in several modes. It can be used to take low resolution frequency spectra continuously, it can take one higher resolution spectrum per shot, or it can follow the time dependence of power at one frequency. In the higher resolution spectra, the resolution is usually 300 kHz FWHM for a scan from 1 to 100 MHz.

2.3.3 Impurity Measurements

An important question addressed in Chapt. 5 of this work is whether the fast ions produced in the edge during ICRF heating generate impurities. While there is a wide range of measurements that are related to impurities, the bolometer arrays, the moly monitor, or the Z-meter would show the results of impurities generated by the edge ion heating, and are briefly described below.

Moly Monitor

The surfaces inside the vacuum vessel exposed to the plasma, including the divertor plates, limiters, and the inner wall, are covered by molybdenum tiles. Alcator C-Mod is unique in its high-Z metal plasma-facing surfaces. Because high-Z materials can potentially radiate large amounts of power, the level of molybdenum in the plasma is monitored. The diagnostic known as the "moly monitor" measures XUV light emitted in spectral lines of high charge states of molybdenum, from Mo XV to Mo XXXII[18]. There are three multilayer mirror-based polychromator channels, measuring three spectral lines at a time resolution of 0.2 to 1 ms.

Bolometers

Alcator C-Mod has arrays of bolometers viewing the main plasma and the divertor region[19]. For the main plasma, there are 16 channels which span the plasma toroidally at the midplane. They are sensitive to neutrals and photons from visible through x-ray energies. There are 8 bolometer channels viewing the divertor. The measurements are inverted to calculate emissivity profiles, which are then integrated to find the total radiated power in the divertor and main plasma.

There is also a diagnostic usually referred to as the "2π bolometer". This is in fact a single, uncollimated XUV photodiode, and not a bolometer, as it is sensitive only to photons. It gives a fast measure of the global radiation from the plasma.

Z-meter

The "Z-meter" is an array of detectors measuring visible bremsstrahlung emission from the plasma with a fast time response, 10 μs. Using the density and temperature profiles, the quantity $Z_{eff} \equiv \sum_i n_i Z_i^2 / n_e$, a measurement of the impurities in the plasma, is calculated.

2.3.4 Neutral Density

The "Ratiomatic" pressure gauge, a standard Bayard-Alpert gauge[20], measures the neutral density at the midplane far from the plasma. The Ratiomatic gauge has a time response of 17 ms.

There is evidence that a cold, tenuous plasma fills the volume around the confined plasma[10]. At typical parameters, $T_e = 10$ eV and $n_e = 1 \times 10^{19}$ m^{-3}, the mean free path of room-temperature neutrals is 0.03 m, much less than the distance between the vessel wall and the SOL. Because of this, the neutral pressure at the Ratiomatic will not be the same as that at the last closed flux surface.

Inside the bulk plasma, the profile can be modeled with the computer code FRANTIC[21], and spectroscopic measurements made over a sequence of identical discharges have shown good agreement[22]. In these discharges, the neutral density as measured by the Ratiomatic was 2×10^{17} m^{-3}. The measured neutral density at the LCFS was 1×10^{14} m^{-3}, showing that there is considerable screening of neutrals. We will consider the Ratiomatic measurement to be an upper limit on the neutral density at the LCFS.

Chapter 3

Perpendicular Charge Exchange Analyzer

Charge exchange reactions occur when an atom or ion captures an electron from a neighboring ion or atom. For example, a hydrogen ion may capture the electron from a nearby hydrogen atom. After this ion is neutralized, it is no longer confined by the magnetic fields in the plasma, and it will leave the plasma in a straight trajectory (barring collisions and reionization). Thus the measurements of the flux of energetic neutral particles from the plasma provides information about the population of ions in the plasma[7]. The particle measurements used in this study were made using a neutral particle analyzer we refer to as the perpendicular charge exchange analyzer (PCX). The PCX simultaneously measures hydrogen and deuterium flux in 39 energy channels and can be scanned poloidally and toroidally.

3.1 Source of CX Neutrals

To interpret the raw data from the PCX, an expression must be developed that relates the count rates of the different energy channels to the plasma parameters. In this section, an equation is presented for the energetic neutral flux that arrives at the

PCX beam line in terms of the volumetric source rate and the attenuation of the flux passing through the plasma.

In a charge exchange reaction, an ion captures an electron from another atom or ion. If the energy of the electron doesn't change, then the reaction is termed resonant charge exchange, and the momenta of the nuclei are, to a good approximation, unchanged.

Alcator C-Mod is operated with majority species of D, H, or ^{4}He, and minority species of D, H, or ^{3}He. The bulk of the experiments described here were done with a D majority, H minority plasma. Because the He gas in the stripping cell is only efficient at stripping D and H the PCX on Alcator C-Mod has so far only been used to measure these two species. Equations and discussion in this chapter are therefore simplified to apply only to charge exchange reactions involving hydrogen and deuterium ions and atoms.

3.1.1 Source Rate

The source rate of energetic neutrals with a given velocity, $\vec{v}_i$, is

$$S(\vec{v}_i, \vec{x}) = \int d^3v_0 f_i(\vec{v}_i, \vec{x}) f_0(\vec{v}_0, \vec{x}) \sigma_{cx}(|\vec{v}_i - \vec{v}_0|)|\vec{v}_i - \vec{v}_0|. \tag{3.1}$$

The distribution function for the ion species, D or H, is subscripted with i, and the 0 subscript is for the total of the hydrogenic neutral species. Since the PCX measurements are made at energies much higher than the neutral temperature, the velocities of the neutrals are not significant, simplifying Eq. 3.1 to

$$S(\vec{v}_i, \vec{x}) = f_i(\vec{v}_i, \vec{x}) n_0(\vec{x}) \sigma_{cx}(v_i) v_i. \tag{3.2}$$

The cross-section for the resonant charge exchange reaction for hydrogen is on the order of 10^{-19} m^2 for the energies of interest. The cross section as a function of energy

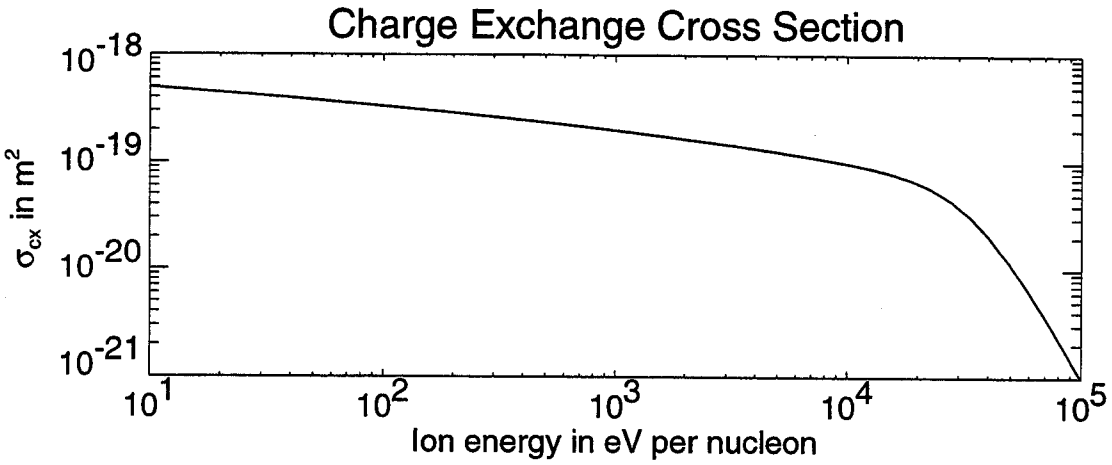

Figure 3.1: Charge Exchange Cross-section for Hydrogen

is plotted in Fig. 3.1[23].

3.1.2 Attenuation

Energetic neutrals produced at some position $\vec{x}$ in the plasma must travel through the plasma to be detected by the PCX. As these are neutrals, they are unaffected by the electric and magnetic fields. The neutrals may, however, be involved in another charge exchange reaction or be ionized in a collision, and thus "lost" from the outgoing flux. Collisions between neutrals can be neglected. For each point along the trajectory of the escaping neutrals, we can calculate the attenuation, α, as a function of position and velocity. If the flux is represented by Γ, then

$$\frac{d\Gamma}{dx} = -\alpha\Gamma. \tag{3.3}$$

The quantity α is the reciprocal of the mean free path, and is a function of plasma density and temperature. If the velocity of the escaping neutral, v, is significantly greater than the local ion thermal velocity, then the contribution to α from charge-exchange is approximately $n_0\sigma_{cx}$. Contributions from ionization reactions are more complicated. If $v_{te} \gg v_0$, then the term in α is $\int d^3v_e\sigma_i(v_e)v_e/v_0$. If x' is used to

parameterize the sight line, between the point $\vec{x}$ where the energetic neutrals are produced and the point of observation $\vec{x}_{obs}$, then the flux of neutrals reaching the observation point is reduced to

$$S_{obs} = Se^{\int_{\vec{x}}^{\vec{x}_{obs}} \alpha(x')dx'}. \tag{3.4}$$

This is the source rate of CX neutrals from a unit volume. To calculate the actual signal measured by the PCX, we must consider how the analyzer is constructed.

3.2 Apparatus

The heart of the PCX, the stripping cell and the main chamber, along with the microchannel plates and much of the electronics, was used on TFTR and has only minor modifications from the one developed and implemented on the PLT tokamak in 1984[24]. This instrument was brought to MIT, and new support structures, vacuum systems, and control electronics were designed and constructed[25].

An engineering drawing of the PCX is included as Fig. 3.2. The parts of the PCX are described below in the sequence that an incoming neutral particle passes through them.

3.2.1 Beam Line

The beam line serves simply to connect the main part of the PCX to the Alcator C-Mod vacuum vessel. The beam line has four baffles, copper gaskets with holes 7/8" in diameter, to reduce the influx of neutral thermal gas when the gate valve is opened during a shot. With this hole size, the baffles do not reduce the energetic particle flux to the detectors. The beam line has a separate vacuum pump. When neutral pressure in the beam line is above 0.1 mTorr, significant scattering of the incoming energetic neutral particles occurs and the data are not used.

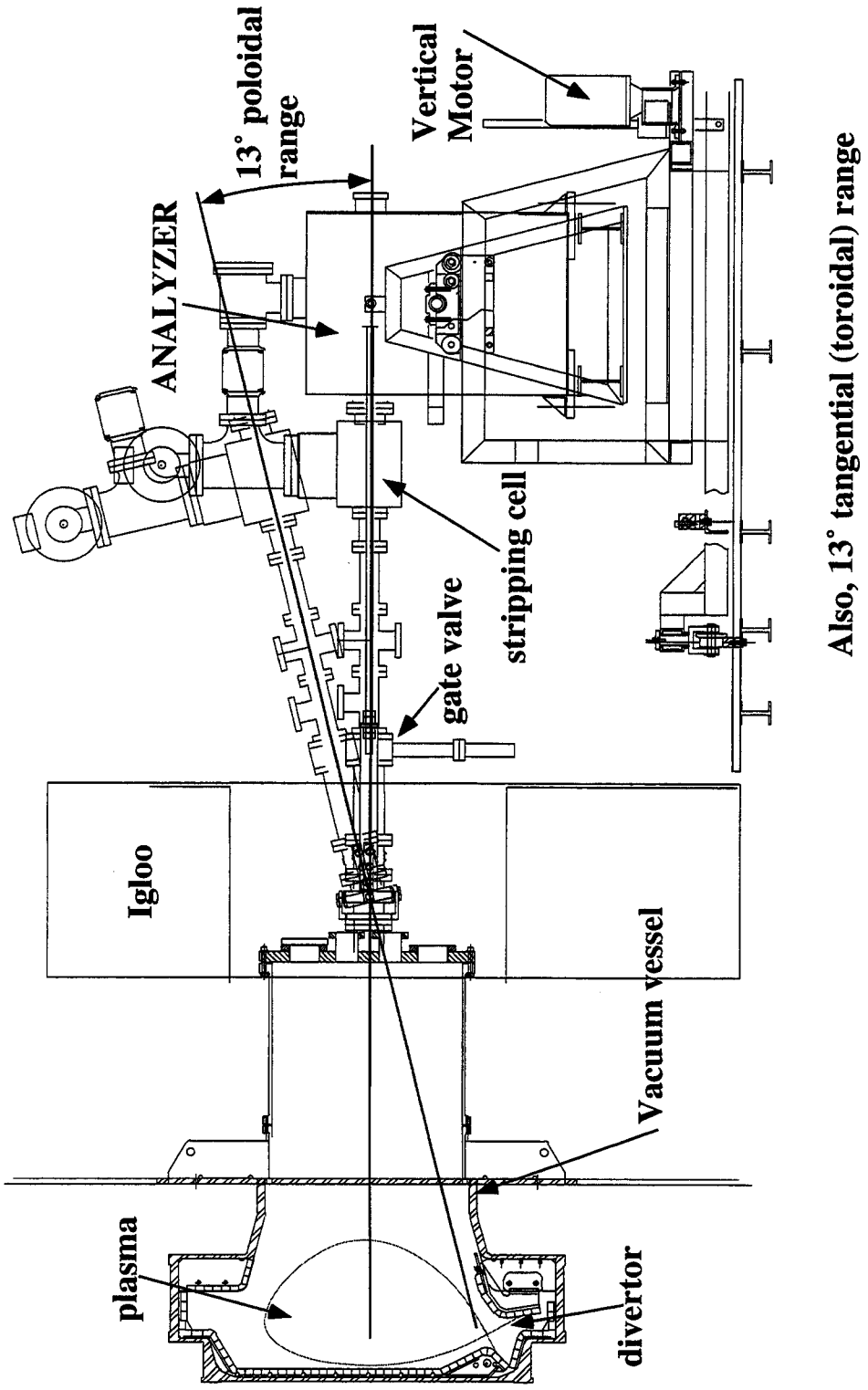

Figure 3.2: Engineering drawing of PCX. Beam line during poloidal scan is also shown.

3.2.2 Stripping Cell

At the ends of the stripping cell there are two rectangular apertures that set the étendue of the analyzer, limiting the incoming energetic neutrals to those with velocities very nearly parallel to the axis of the beam line. The collimation is necessary for accurate energy and mass measurements in the analyzer. The apertures are 1.3 mm by 2.4 mm and the length of the stripping cell is 0.248 m.

The stripping cell is kept at a constant pressure of approximately 1 mTorr of ^{4}He gas. The He gas serves to strip the electron from the incoming energetic neutral hydrogen atoms. The efficiency of the stripping cell for hydrogenic species in the region of interest is approximately 0.2, i.e. 20% of the incoming atoms are converted to bare protons or deuterons. More generally, the stripping efficiency is a function of incoming particle energy and the helium pressure in the stripping cell[26]. The He pressure in the stripping cell is measured by a vacuum gauge during the shot, so that the correct stripping efficiency is used in analysis.

3.2.3 Main Chamber

Particles passing through the stripping cell enter the main vacuum chamber of the PCX. This chamber is made of iron to shield out other fields from the tokamak and provide a return path for the magnet flux. Ion paths in the chamber are directed by parallel electric and magnetic fields generated by a pair of biased plates and a magnet. The fields are as close as possible to uniform, and have their axis oriented in the toroidal direction. The magnetic field (B) causes the incoming ions to execute one half a Larmor radius to the detectors, as shown in Fig. 3.3. This half orbit takes time $t_f = \pi m/qB$, regardless of particle velocity. The diameter of the half orbit is $r = vm/2qB$, so ions with different velocities finish a half orbit with different vertical displacements and strike different detectors.

At the same time, ions are accelerated parallel to the field axis by the electric field

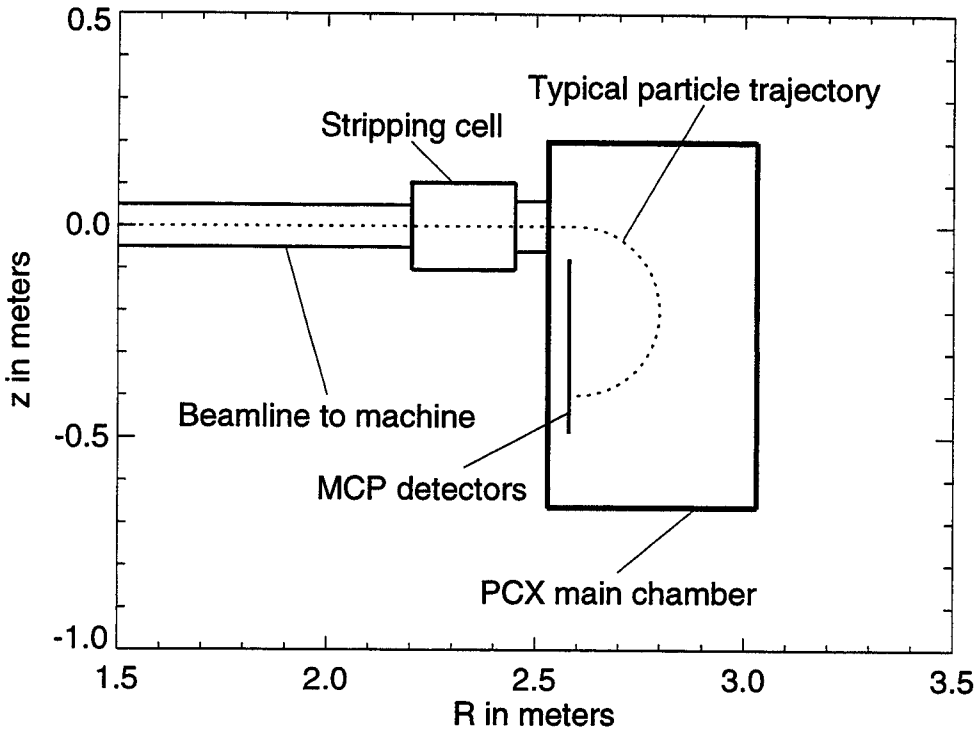

Figure 3.3: drawing of PCX main chamber

(E). At the end of the half orbit, they are displaced by $(qE/2m)t_f^2 = m\pi^2 E/qB^2$. Note that this is also independent of incident particle velocity. Therefore, hydrogen ions are displaced along the magnetic field axis by a certain distance, and deuterium ions are displaced by twice that amount, thus separating incoming particles by mass.

3.2.4 MCP's

Particle detection is by means of three arrays of microchannel plates (MCP's). Each array has 3×25 detectors. These are arranged to give 75 energy channels and three mass (or m/q) rows. The MCP's are biased so that there is a voltage difference of 2 kV between the two sides. An incident particle causes an avalanche of electrons in the tiny tubes that make up the MCP, resulting in a measurable puff of charge. Because of problems of crosstalk observed at Princeton, we are using only every other channel, giving 13 useful energy channels for each mass on a MCP, for 39 energy

channels for each mass. The dead space between the active channels causes about 60% of the particles in the energy range not to be counted. With three mass rows, the analyzer was designed to simultaneously measure hydrogen, deuterium, and tritium flux. As Alcator C-Mod has no tritium, that row is left unconnected, except for one channel used for noise detection.

The range in energies of the particles the PCX measures is controlled by the magnetic field. Due to the geometry of the analyzer, particles reaching the highest energy channel have 40 times the energy of particles reaching the lowest channel. For example, the PCX might be examining flux in the range of 1 keV to 40 keV. The lowest energy the PCX can reliably detect is around 500 eV; the stripping efficiency falls sharply below 1 keV[26], making it impossible to observe particles much below this energy. The upper energy limit is set by the maximum magnetic field the magnet can provide and the significant decrease in charge-exchange rate coefficient above 50 keV. We have successfully observed hydrogen ions with an energy of 150 keV with the PCX.

3.2.5 Electronics

There are transistor amplifiers close to the anodes of the MCP's. They are connected to the MCP pins with only 5 cm of wire, and are in vacuum. In practice, these buffer amplifiers are fragile, and some have failed. During a run, 10 or more of the 78 channels used might be inoperable due to failed buffers.

The signals from the buffer amplifiers travel through 2 m of triax cable to the pulse amplifier and discriminator modules (PAD's). These transform the pulses into clean triangular pulses of uniform height. The pulses are then passed to a bank of scalers. These count the number of pulses in a time bin, from 0.2 ms to 2 ms in these experiments, for 1024 time bins on each shot. The data are collected over a CAMAC system and stored on disk after every shot. The MDSplus system is used to access

the data[27].

3.2.6 Movement

The PCX has significant superstructure that allows the analyzer to scan in position while remaining pointed through the hole in the port. In the nominal position of the PCX, the sight line is horizontal and passes through the plasma at the midplane, perpendicular to the toroidal field. From this position, the analyzer can be scanned either "toroidally" or "poloidally". While scanning, the PCX pivots about a point $R = 2.02$ m at the midplane. There are bars attaching the main chamber of the analyzer to a gimbal on the port cover which keep the analyzer aligned during a scan.

In a toroidal scan, the PCX is moved on rails by a motor; the sight line remains horizontal through the midplane. This allows the PCX to measure escaping neutrals whose velocity vectors are at a finite angle with respect to the magnetic field. The PCX can be scanned toroidally to 11.7° from perpendicular. Note that the angle the sight line makes with respect to the toroidal field is not constant, but changes along the sight line. This extreme sight line is tangent at a radius 0.41 m ($R/R_0 \simeq 0.7$).

In a poloidal scan, a motor-operated scissors lift raises the PCX. The sight line remains perpendicular to the toroidal field, but now passes through the plasma below the midplane. At the furthest extent, the analyzer can "see" just above the X-point. While the sight line remains perpendicular to the toroidal field, it is not perpendicular to the *total* magnetic field. With the PCX raised to its maximum height, the sight line makes an angle of 11.9° with respect to horizontal. This sight line passes through R_0 of the plasma at 0.25 m below the midplane. While the PCX could be operated in a position where it has moved both toroidally and poloidally, this is not done in practice. The PCX only changes position between shots.

3.3 Absolute Calibration

The analyzer observes particles produced in a particular volume of the plasma, which is essentially a very narrow pyramid. At the center of the plasma, $R = .66$ m, the footprint of the sight line is 0.023 m vertically and 0.042 m toroidally. The area of the footprint varies approximately as the square of the distance to the stripping cell. The analyzer only observes particles whose velocity is such that they pass down the beam line. If $\hat{l}$ is a unit vector pointing along the sight line, then the analyzer selects particles with $\vec{v}_0 \parallel \hat{l}$. Practically, it admits particles within a range of velocities,

$$\frac{|\vec{v}_0 \times \hat{l}|}{v_0} < (0.0011 - 0.00052),$$

where the range is due to the aperture being rectangular, not circular. From this we find a solid angle of acceptance of $\Omega = 6 \times 10^{-7}$. The range is calculated at the center of the plasma, and is proportional to the inverse of the square of the distance to the aperture. This range of velocities is only valid at the center of the "pyramid" volume of the sight line. At the edge of the footprint, the range of velocities accepted goes to zero, so most of the contribution is from the center of the pyramid. To make the equations tractable, the reasonable assumption is made that variations in plasma parameters are negligible over the footprint of the sight line, and the ion distribution function is well represented by an average over the range in pitch angle. For example, the scale length for variation in the bulk ion temperature in the z direction is about 0.13 m, which is 10 times the vertical extent of the viewing area. Experimentally, variations in distribution function with pitch angle have scales of more than $5° \simeq .09$ radians, much larger than the resolution noted above, 0.0011 radians. The range in pitch angle of the particles accepted can therefore be ignored as well. Because the analyzer is sensitive to a greater range of pitch angles near the axis of the sight line volume, the effective footprint area A used is $\frac{1}{4}$ the total

area. Thus a volume and velocity-space integral of particles in the sight line can be simplified;

$$\int d^3x \int d^3v[\ldots] \simeq \int dl \int v^2 dv A\Omega[\ldots]. \tag{3.5}$$

If the distance from point $\vec{x}$ to the analyzer is L, then $A \propto L^2$ and $\Omega \propto 1/L^2$. The quantity $A\Omega$ is then independent of L (and v_0). This product is called the étendue. It can be calculated very simply. If the apertures in the stripping cell are Δx by Δy, and are separated by a distance D, then the étendue is $\Delta x^2 \Delta y^2 / D^2$. For the PCX, the étendue is 1.5×10^{-10} m^2.

Combining Eqs. 3.2 and 3.4 and integrating over the entire sight line through the plasma, the flux into the PCX, as a function of velocity, is

$$\Gamma(v_i) = \int dl A\Omega v_i^2 f_i(v_i, \hat{l}, \vec{x}) n_0(\vec{x}) \sigma_{cx}(v_i) v_i e^{\int_{\vec{x}}^{\vec{x}_{obs}} \alpha(x')dx'}. \tag{3.6}$$

It is a short step from Eq. 3.6 to an expression for the actual count rates of the PCX channels. As discussed above, the stripping cell has a finite efficiency, $\epsilon_{sc}(v)$. Also, the MCP's have a finite detection efficiency, $\epsilon_{MCP}(v)$, in the range 60-85%, though this is not known to high accuracy. If a channel counts incoming particles with velocities in a range v_1–v_2, the number of counts per unit time is

$$C = \int_{v_1}^{v_2} dv \epsilon_{sc}(v) \epsilon_{MCP}(v) \Gamma(v). \tag{3.7}$$

Because $\Gamma(v)$ varies slowly enough as a function of velocity, this can be written

$$C = \Delta v \epsilon_{sc}(v) \epsilon_{MCP}(v) \Gamma(v). \tag{3.8}$$

Letting k refer to the various channels, each responsive to a range Δv_k centered on

v_k, the count rates for the channels are

$$C_k = \Delta v_k \epsilon_{sc}(v_k)\epsilon_{MCP}(v_k) A\Omega\sigma_{cx}(v_k)v_k^3 \int dl f_i(v_k, \hat{l}, \vec{x}) n_0(\vec{x}) e^{\int_{\vec{x}}^{\vec{x}_{obs}} \alpha(x')dx'}. \tag{3.9}$$

On the Alcator C-Mod PCX, a typical count rate during ohmic plasmas is 3×10^4 counts per second at a few keV.

If the ions are assumed Maxwellian, and profiles for n_i, T_i, and n_0 are known or assumed, then the expected count rate can be easily calculated.

From Eq. 3.9, dividing out the known quantities outside the space integral, an experimentally measured count rate can be used to calculate

$$\hat{f}(v) = \int dl f_i(v, \hat{l}, \vec{x}) n_0(\vec{x}) e^{\int_{\vec{x}}^{\vec{x}_{obs}} \alpha(x')dx'}. \tag{3.10}$$

This function $\hat{f}(v)$ is a useful starting point for further analysis.

There are two special cases of interest. First, if the plasma is small or low density, then attenuation is negligible and the exponential term is approximately equal to unity. Tokamak plasmas are hottest in the center, and at energies sufficiently above T_i the spatial integral is dominated by the contribution from the highest temperature along the sight line. If f_i is a Maxwellian, then $\ln \hat{f} = -\mathcal{E}/T_{i,max} + c$, with $\mathcal{E} = \frac{mv^2}{2}$, or $T_{i,max} = -[d \ln \hat{f}/d\mathcal{E}]^{-1}$. Practically, we do this by fitting a line to an appropriate range of $\ln \hat{f}$ and using its slope. This formula, used to calculate bulk temperatures, is only an approximation, and more accurate ways of finding T_i from the CX flux are well known[7].

This derivative can be calculated for any $\hat{f}$, and gives us a quantity referred to as the "tail temperature". This temperature is not related to average particle energy, but to the relative number of particles at different energies.

The other special case of interest is a suprathermal population in the plasma edge.

If this population exists over some Δr at radius r, then

$$\hat{f}(v) = n_0(r) f_i(v, \hat{l}, r) \Delta r / (\hat{r} \cdot \hat{l}). \tag{3.11}$$

If $n_0(r)$ is known, then the PCX has measured the number of suprathermal particles (in a certain energy range with a certain pitch angle) per unit area of plasma surface. Similarly, quantities such as the energy in the tail per unit surface area can be computed.

3.4 Sources of Error

Three possible sources of error in the PCX measurements must be considered. First, any counting measurement has a statistical variation, a type of random error. Second, the level of pick up on the detectors must be monitored. Last, any systematic error must be accounted for.

3.4.1 Counting Statistics

The number of counts in a period of time follows a Poisson distribution. In analysis, the counts are generally summed over a sufficient time period to get a significant number. The error is used to weight fits for T_{tail}. The noise signal is also governed by counting statistics, and has an error. So if a channel gets m counts in a time period, and n of these are noise, the number of counts is adjusted to $m - n$, but the random error is $\sqrt{m}$, not $\sqrt{m - n}$. This is significant when $m - n$ and n are of similar size.

3.4.2 Pick-up

The PCX is susceptible to several sources of noise. The neutrons produced by nuclear reactions in the plasma are detected by the MCP's, and hard x-rays from run-away

electrons are also counted. Also, pick-up from the RF system is possible. One channel from the tritium row of the MCP's is hooked up, replacing the last D channel. As there is no tritium in the plasma, counts on this channel indicate the level of noise counts. This is subtracted from the other channels during data analysis. The signature of pick-up is that it is uniform across all the channels. In general, except in the highest energy channels of the minority species, the number of counts due to pick-up is negligible compared to the actual particle counts. Pick-up from the 80 MHz ICRF system has not been observed.

3.4.3 Systematic Error

One well known source of error in this type of analyzer is mass contamination between the D and H rows. As the ratio of hydrogen density to deuterium density has been measured to reach as low as 0.5%, a small amount of scattering of deuterium into the hydrogen row can overwhelm the hydrogen signal. Similarly, a high energy tail in hydrogen produces high count rates in the higher energy channels, causing counts to leak over and contaminate the D row. There is a specific signature of this effect; during significant leaking, plots of $\ln \hat{f}_D$ and $\ln \hat{f}_H$ versus channel number (rather than energy), have the same shape. Because the H row looks at energies twice what the D row measures, the shapes of these two flux curves are usually different. So if T_{tail} for hydrogen is almost exactly two times the T_{tail} calculated for deuterium, mass contamination is indicated. In practice, mass contamination is only observed at the lowest hydrogen concentrations, which seldom occur.

There is systematic variation between different channels, which can be seen at times when the count rate is very large, implying that the random error is small. This can be due to differences in the MCP channels or buffer boards. We assume that this systematic variation in a given channel is random across the channels, and the fits are still valid.

Note that there is no way to do an in situ calibration of the étendue or other efficiencies. We have roughly checked the alignment using a light source, and we believe the calculated étendue is approximately correct.

3.5 Sample Data

As an example of the data regularly taken by the PCX, Fig. 3.4 shows data from shot 960112030. It includes raw data from the deuterium row of the PCX, and the general plasma parameters from analysis of data from other diagnostics. Figure 3.5 shows the data from the hydrogen row. The channels on the D row collect neutrals with an energy from 0.8 keV to 14 keV, and the H row covers energies from 1.5 to 29 keV. The counts shown are acquired in 2 ms time bins. This shot is at relatively low density for C-Mod, with a central electron density of 1×10^{20} m^{-3}. This is a very high plasma density compared to other tokamaks, however. The trace "nl_04" is the line integrated electron density through a vertical chord through the plasma center. Note that, even at this density, the mean free path for an energetic neutral with 10 keV is 0.1 m, so the path from the center of the plasma to the edge is more than two mean free paths so attenuation is significant. The signal in the PCX D row labeled "noise monitor" is the noise monitor discussed above. Throughout the discharge, the rate of counts in this channel is less than 10 counts/s, while the channels counting particles are receiving at least 50 counts/s. On the H row, though, the channels above channel 34 are at the noise level throughout most of the shot. On this shot, the PCX sight line is horizontal through the midplane, and scanned toroidally to 10.4° from perpendicular.

The spike in the PCX signals at 200 ms is when the plasma becomes diverted. At 0.7 s, the RF heating is turned on for 70 ms. The plasma temperature increases, as does the total neutral flux. There is a sharp drop in the H_α light at 790 ms,

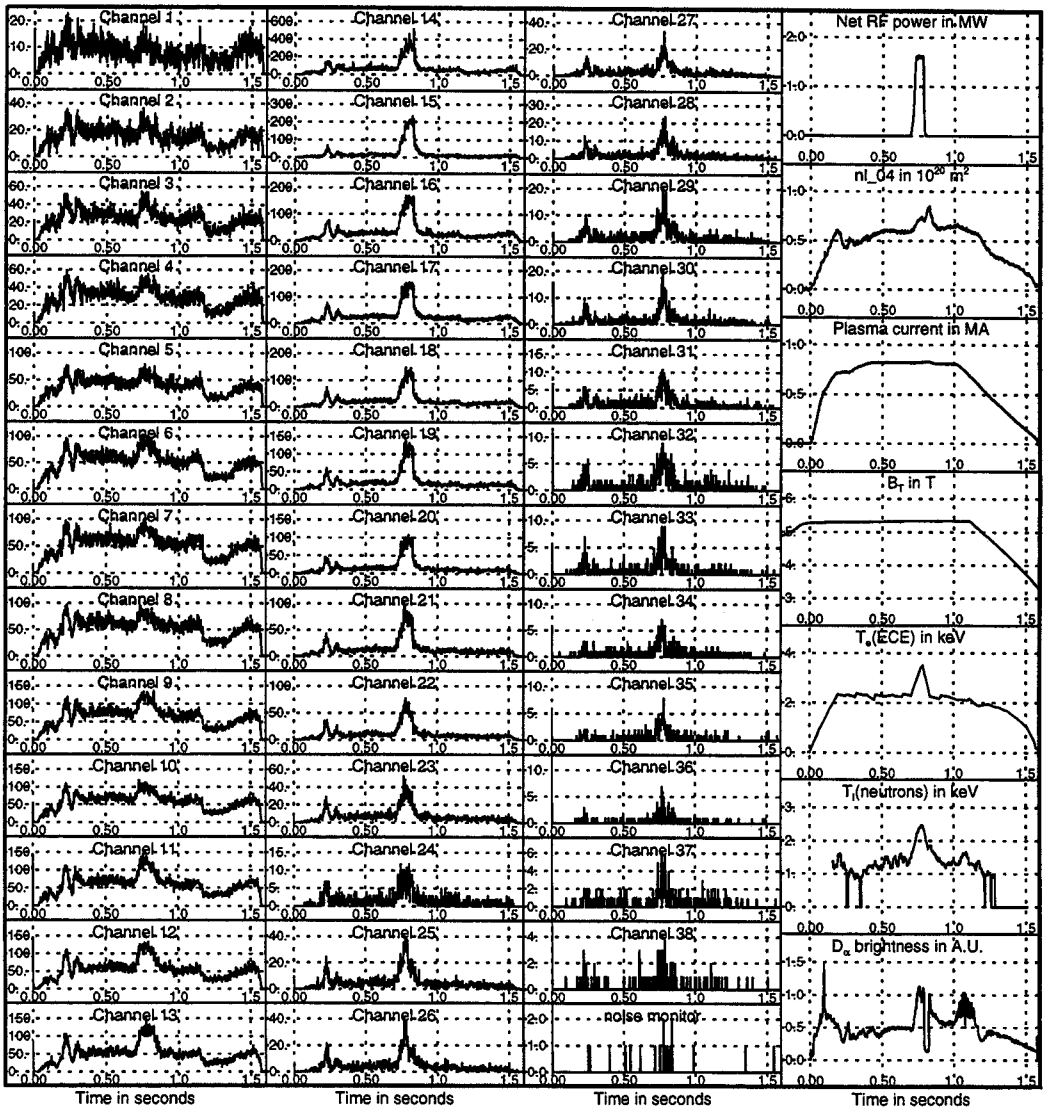

Figure 3.4: PCX D row and plasma parameters

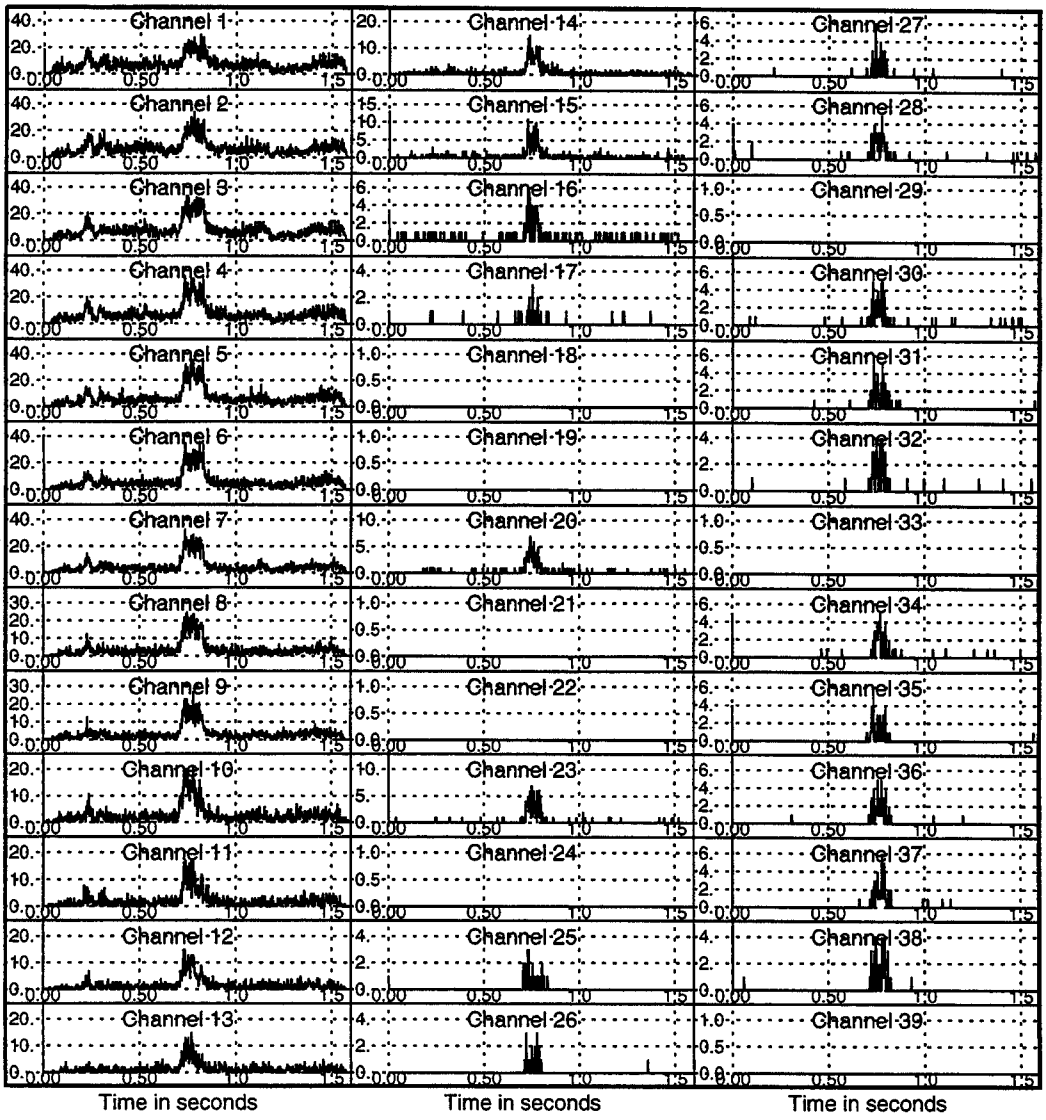

Figure 3.5: PCX H row

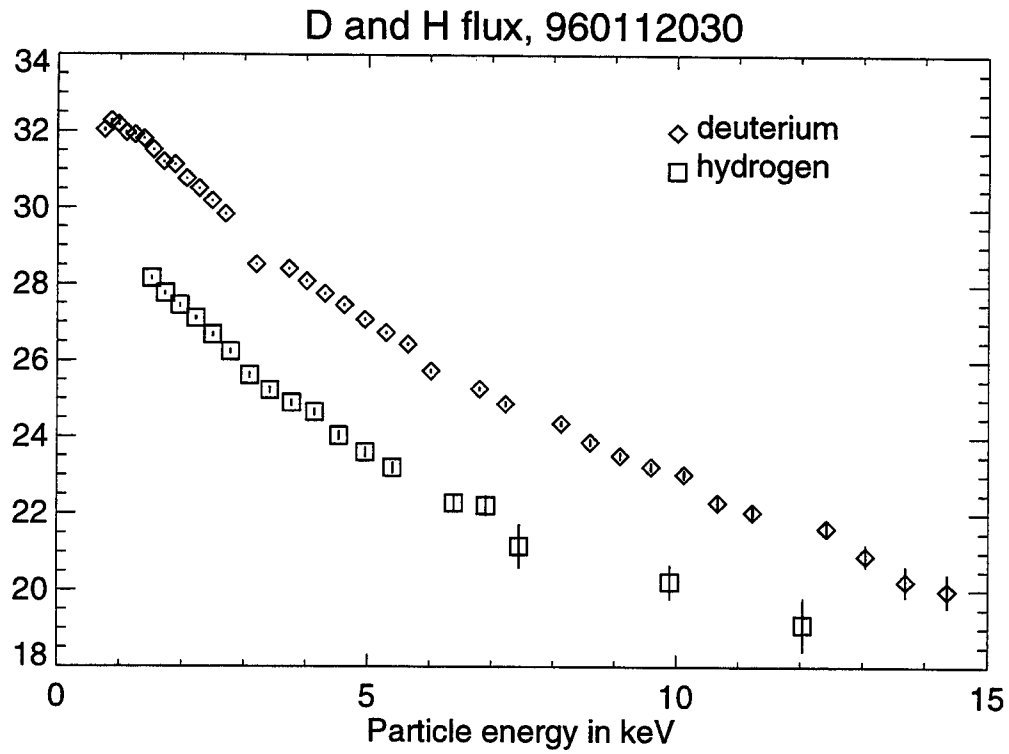

Figure 3.6: PCX D and H flux, $\ln \hat{f}$, as defined in Eq. 3.10

indicating the plasma has gone into H-mode. The improved confinement causes the plasma density to increase sharply.

In Fig. 3.6, the calculated values for $\ln \hat{f}_D$ and $\ln \hat{f}_H$ are plotted, with the error bars representing the random statistical error. The curve for hydrogen is the same shape as the deuterium curve, and lower than it by 3.4. This indicates that the ratio of hydrogen density to deuterium density is $e^{-3.4} = 0.03$. Because the count rates are relatively high, the statistical error is smaller than the systematic error for several of the channels.

The deuterium flux during the ohmic L-mode, RF heated L-mode, and H-mode phases is shown in Fig. 3.7. Fitting a straight line to the flux between 8 and 14 keV gives ion temperatures for these times as 1.4, 1.9, and 1.7 keV. The ion temperature measured by the neutron detectors is 1.4, 2.4, and 2.0 keV during these time periods. Note that the electron density and temperature are also different during the H-mode

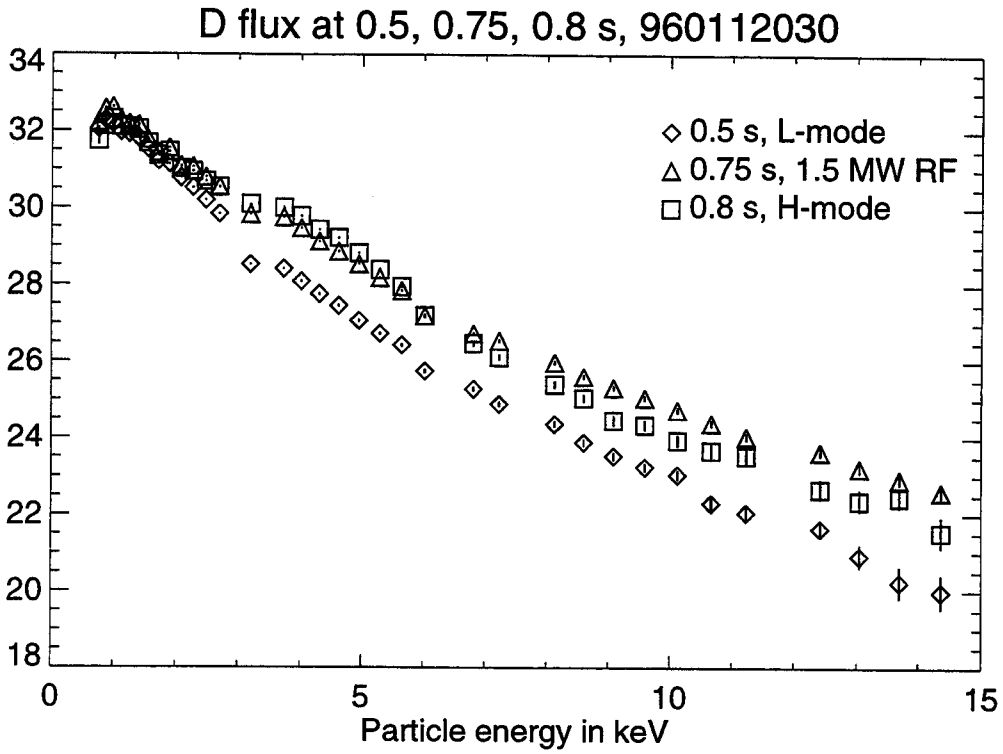

Figure 3.7: PCX D flux during L-mode, ICRF, H-mode

period of this shot, as shown in Fig. 3.4. A similar plot for hydrogen is shown in Fig. 3.8. During the RF heating, the fit to the hydrogen flux shows a temperature of 3.4 keV. During hydrogen minority heating with a low hydrogen concentration, it is expected that the hydrogen distribution function have a tail hotter than the bulk ion temperature[12].

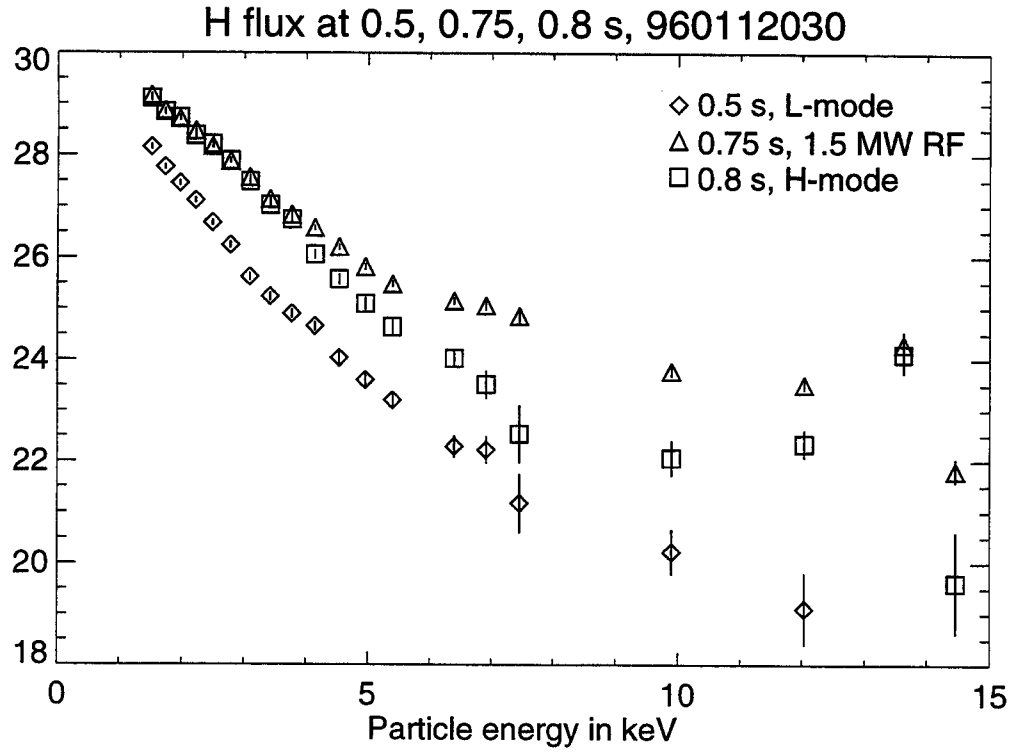

Figure 3.8: PCX H flux during L-mode, ICRF, H-mode

Chapter 4

Dynamics of Edge Ions

To interpret the measurements made by the charge exchange analyzers, it is necessary to understand the motion of energetic ions in the plasma edge.

In the complex geometry of the tokamak magnetic field, ions change their velocity both parallel and perpendicular to the magnetic field. Most but not all ions remain near a flux surface.

In general, interaction of ions with ICRF near a cyclotron harmonic generates ions with large perpendicular velocity[12]. Orbit dynamics are used to calculate at what location in its orbit an observed particle has a purely perpendicular velocity.

From orbits and collision mechanics, the confinement times of ions in the edge can be estimated. Estimated confinement times are used in Chapt. 6 to calculate the RF power absorbed directly by ions in the plasma edge.

4.1 Behavior of Fast Ions in Tokamaks

The magnetic field geometry controls the motion of ions in tokamaks. Edge ions of interest are in banana orbits, an effect of poloidal fields, and possibly ripple-trapped orbits, a result of toroidal field (TF) ripple.

To understand the motion of ions in a tokamak, we must first describe the relevant

parts of the magnetic field geometry, including the poloidal field and toroidal asymmetries in the toroidal field. Next, the orbits of banana-trapped and ripple-trapped ions are presented.

4.1.1 Tokamak Magnetic Fields

The magnetic fields in a tokamak are generated by external magnetic coils, currents flowing in the plasma, and eddy currents flowing through other structures.

The largest magnetic field in a tokamak is the toroidal field (TF), which is generated by a toroidal solenoid. In cylindrical coordinates (R,z,ϕ), the toroidal field ($\vec{B} \cdot \hat{\phi}$) is approximately $B_\phi = (B_0 R_0)/R$ in the plasma region, where B_0 and R_0 are constants. Because the field is generated by a finite number of coils, the resulting field has a weak ϕ dependence. The field generated by the TF coils is better represented by[28]

$$\vec{B}_T = \frac{B_0 R_0}{R}\left(1 + \delta(R,z)\cos(N\phi)\right)\hat{\phi}. \tag{4.1}$$

The number of coils is represented by N, and the quantity δ is referred to as the toroidal field ripple. In Alcator C-Mod, the ripple is less than 0.004 everywhere in the main plasma. In the area where $0.7 < R < 0.95$ meters and $|z| < 0.3$ meters, the ripple is approximately[29]

$$\delta(R,z) = 0.0038 e^{\frac{R-0.89}{0.044}}, \tag{4.2}$$

where R is in meters. Alcator C-Mod has 20 TF coils.

The toroidal field ripple has two effects important here. First, it makes the radius of cyclotron resonance surfaces a function of ϕ. For example, we will need to know

R_ℓ such that

$$\omega_{rf} = \ell\omega_{ci} = \frac{q}{m}B(R_\ell).$$

R_ℓ must be a function of ϕ because of the TF ripple. Second, as will be discussed more fully in the next section, the break in toroidal symmetry can lead to particles being trapped near the minima in the ripple and lost from the plasma.

The toroidal component of the total magnetic field, $\vec{B} \cdot \hat{\phi}$, also has a contribution from poloidal currents in the plasma. This is largest in the center and goes to zero at the plasma edge, and is independent of ϕ.

The poloidal components of the magnetic field come from plasma currents and external vertical field coils[9]. By definition, the poloidal field is always tangent to the flux surface. On Alcator C-Mod, the poloidal field is of the same order outside the plasma as inside and is around 1/5 the magnitude of the TF at the edge.

4.1.2 Ion Orbits

While the equations describing the motion of ions in tokamak magnetic fields are well known[30], a brief discussion is presented to facilitate their use in analysis of the data presented later. The PCX measures ions at different pitch angles and at different points in the plasma. Analysis of the ion orbits is necessary to understand where in physical and phase space these particles may have been accelerated. Also, the confinement of these ions near the plasma edge depends on where their orbits take them.

In the roughest approximation, an ion in a magnetic field will follow a helical path along a field line. In the measurements of edge ion tails, ions with energies up to 30 keV were observed in fields as low as 2 T. These ions have a Larmor radius, $\rho_L = v_\perp/\omega_{ci}$, of approximately 0.01 meters. This is the same order as density and temperature scale lengths in the plasma edge, but is small compared to scale lengths

of the magnetic fields.

The motion of ions in the curved magnetic fields of the tokamak is best described through the use of invariants of the ion motion. If the time and length scales for changes in the magnetic field are large compared to those of the orbits, there are quantities that remain nearly constant during particle motion. These are the particle energy,

$$\mathcal{E} = \frac{1}{2}mv^2, \tag{4.3}$$

the particle magnetic moment,

$$\mu = \frac{mv_\perp^2}{2B}, \tag{4.4}$$

and the angular momentum,

$$P_\phi = mRv_\phi + qR\vec{A}\cdot\hat{\phi}, \qquad \text{where } \vec{B} = \vec{\nabla}\times\vec{A}. \tag{4.5}$$

Solutions of these equations consist of passing orbits and two types of trapped orbits, banana orbits and ripple-trapped orbits. Equation 4.5 represents a constant of motion only when the magnetic field is toroidally symmetric; ripple-trapped orbits result from asymmetries in the toroidal field, and angular momentum is not conserved.

Banana orbits

Consider a particle on the midplane at some $R_1 > R_0$, with a velocity $\vec{v}_1$. In a magnetic field $\vec{B} = \frac{B_0 R_0}{R}\hat{\phi}$, if μ and $\mathcal{E}$ are constant over an orbit, then B and $v_\parallel$ must be related by

$$v_\parallel^2 = \frac{2}{m}(\mathcal{E} - B\mu). \tag{4.6}$$

Writing in terms of the initial perpendicular velocity, total velocity, and particle position (radius),

$$\frac{v_{\parallel}^2}{v^2} = 1 - \frac{v_{\perp 1}^2}{v^2}\frac{R_1}{R} = 1 - \frac{R_b}{R}. \tag{4.7}$$

If the field line the particle follows reaches R_b, defined by

$$R_b = R_1 \left(\frac{v_{\perp 1}}{v}\right)^2, \tag{4.8}$$

then at $R = R_b$ the particle's parallel velocity goes to zero, and the particle bounces back toward larger radius in a banana orbit. If the field line does not pass inside R_b, the particle passes around the torus, making a poloidal rotation every few toroidal rotations.

As a particle passes around an orbit, it deviates from a field line according to Eq. 4.5. The width of the banana orbit is approximately

$$\Delta R = 2\frac{mRv_{\parallel}}{qB_p}, \tag{4.9}$$

where B_p is the poloidal magnetic field. This equation is valid when ΔR is small compared to scale lengths for the poloidal field and radial electric fields can be neglected. For thermal ions in the plasma edge, $\Delta R \sim 2$ mm, depending on the plasma current; this is calculated for a typical current, $I_p = 800$ kA implying $B_p \simeq 0.6$ T. Ions heated in the edge plasma during ICRF injection have been observed with $\frac{v_{\parallel}}{v} = 0.5$ at the midplane. If such a particle has an energy of 10 keV, then the banana width of its orbit is 0.06 meters. This is large compared to relevant lengths in the plasma edge. The distance between the LCFS and the RF protection limiter at the outboard midplane is usually less than 20 mm. For these orbits, Eq. 4.9 is only a rough approximation.

The time for a particle to execute a banana orbit, τ_b, can be given approximately

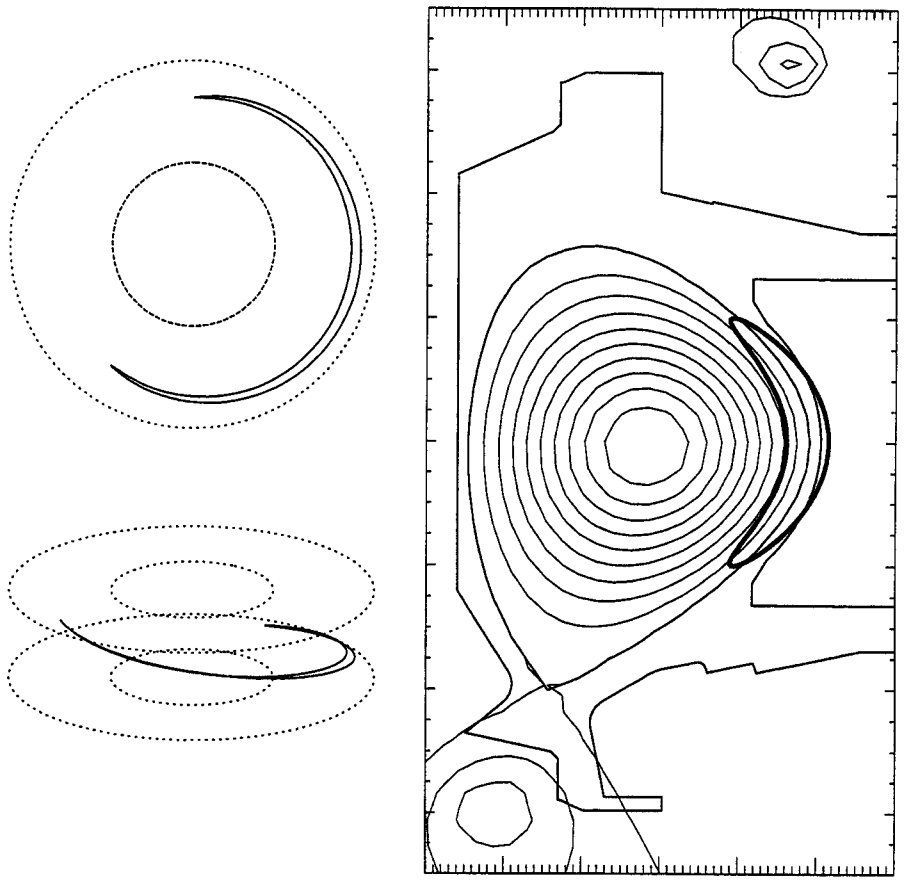

Figure 4.1: Banana orbit of an energetic particle

in terms of the basic parameters;

$$\tau_b = \frac{2\pi\sqrt{2rR_0}}{v_\perp}\frac{B_0}{B_p}. \tag{4.10}$$

A banana orbit for an energetic particle in the outer plasma is shown in Fig. 4.1. The figures on the left show two projections of the orbit in space. The figure on the right shows the same orbit with the toroidal angle dependence suppressed.

The banana orbits of edge ions observed by the PCX are shown in Fig. 4.2. The orbits are shown as viewed from the outboard midplane on a flat projection. This figure also shows graphically that the PCX observes ions at their banana tips during a poloidal scan, and at the center of their orbits during a toroidal scan.

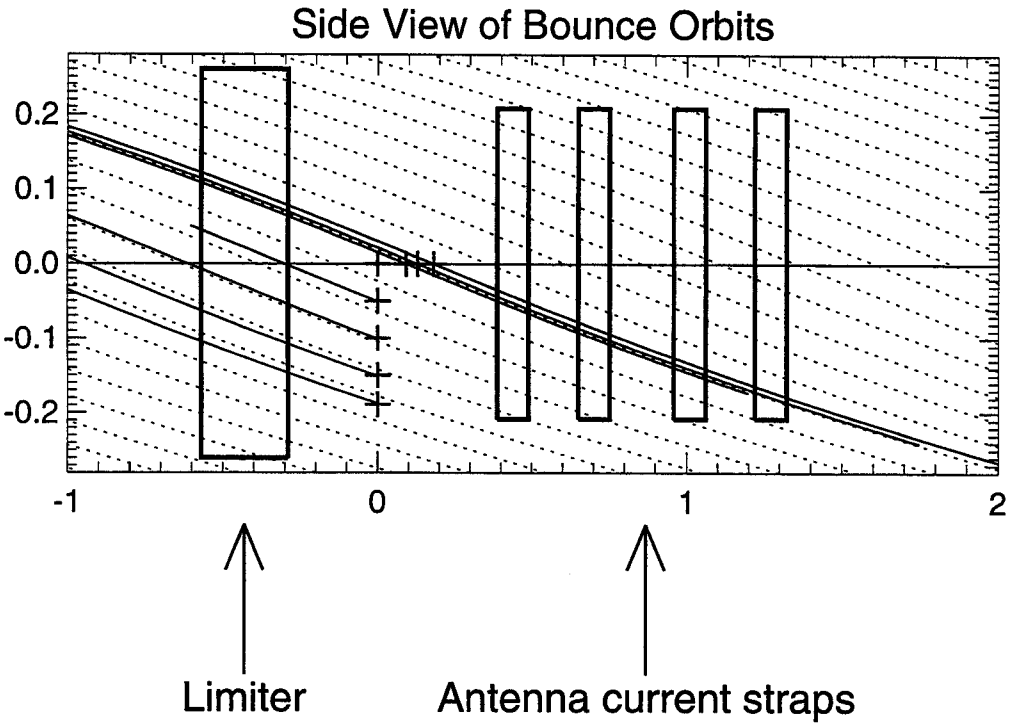

Figure 4.2: Orbits of ions in the edge

Ripple-trapped orbits

Banana orbits occur when $v_{\|} = 0$ along an ion trajectory, as described in Eq. 4.7, at which point the particle reverses direction. The asymmetry in the more accurate form for B_0, Eq. 4.1, adds more possible bounce points, which lead to ripple-trapped particles. Because the ripple in the toroidal field is small, ripple-trapped ions have $v_{\|} \ll v_{\perp}$.

A particle can be ripple trapped if there exist two local maxima in the magnetic field along the field line. Maxima occur when

$$\vec{\nabla} B \cdot \vec{B} = 0.$$

Using Eq. 4.1, and noting that the dominant terms in $\vec{\nabla} B$ come from the B_ϕ dependence on R and ϕ,

$$\vec{\nabla} B \simeq -\frac{B_0 R_0}{R^2}\hat{R} - \frac{B_0 R_0}{R^2}\delta N \sin(N\phi)\hat{\phi}, \tag{4.11}$$

$$\vec{\nabla} B \cdot \vec{B} \simeq -\frac{B_0 R_0}{R^2} B_R - \frac{B_0 R_0}{R^2}\delta N \sin(N\phi) B_\phi. \tag{4.12}$$

Setting the left-hand side equal to zero shows the condition under which ripple-trapping can occur,

$$B_R < \delta N B_\phi. \tag{4.13}$$

Defining θ as the angle between $\vec{B}_p$ and $\hat{z}$, $B_R = B_p \sin\theta$, the condition becomes

$$\sin\theta < \delta N \frac{B_\phi}{B_p}. \tag{4.14}$$

If the plasma has a circular cross section, then θ is the poloidal angle. In the shaped C-Mod plasmas, there is no simple interpretation to θ. In the volume where ripple-trapping is possible, only a small percentage of the particles are ripple-trapped. Outside this region, no particles are ripple-trapped.

To find the maximum parallel velocity of a ripple-trapped particle, we use Eq. 4.4, evaluated at the bounce points and the center of the ripple well,

$$\frac{mv_{\parallel max}^2}{2} = \mathcal{E} - \mu\bar{B}(1-\delta), \tag{4.15}$$

$$0 = \mathcal{E} - \mu\bar{B}(1+\delta). \tag{4.16}$$

Subtracting these and rearranging gives

$$\frac{v_{\parallel max}}{v} \simeq \sqrt{2\delta}. \tag{4.17}$$

If $\delta = 0.004$, then particles with $\frac{v_{\parallel max}}{v}$ less than 0.009 can be trapped, that is with velocity vectors within 5° of perpendicular to the magnetic field.

For ripple-trapped particles, the toroidal component of the vector potential, A_ϕ, is not even approximately independent of ϕ. Because of this, the ion angular momentum P_ϕ is not conserved, and the particle is not kept near a flux surface, as banana-trapped particles are. Ripple-trapped particles will instead exhibit ∇B-drift. In C-Mod, the ∇B-drift direction is usually downwards. The drift velocity is

$$\vec{v}_{\nabla B} = \frac{mv_\perp^2}{2}\frac{1}{qB}\frac{\vec{B}\times\vec{\nabla}B}{B^2} = \frac{mv_\perp^2}{2}\frac{1}{qRB}\hat{z}. \tag{4.18}$$

Curvature drift is negligible for ripple-trapped particles, as they have $v_\perp \gg v_\parallel$. For a 10 keV ripple-trapped particle, the drift velocity is 3×10^3 m/s.

Because the ripple-trapping region is small, particles can easily scatter out, with a characteristic time smaller than the large-angle collision time by a factor of δ. At the LCFS, thermal deuterons trapped in the ripple well will only drift a distance on the order of 10^{-8} meters before scattering out. As will be discussed in the next section, suprathermal ions have a much slower collision rate. Nevertheless, ripple-trapped 10 keV ions will only drift approximately 1 millimeter before scattering out of the ripple-trapping region of velocity space. This assumes that $n = 10^{20}$ m^{-3} at the LCFS.

4.2 Confinement of Edge Ions

The distribution function of energetic ions in the plasma edge is only partly a function of the interaction with the RF fields and the orbit dynamics. The evolution of the distribution function also depends on the rate at which these energetic ions either escape from the plasma or lose their suprathermal energy.

There are three primary mechanisms by which the ions of interest are lost. They may be unconfined, and not stay in the plasma for an entire orbit; they may charge exchange and become energetic neutrals; or they may lose their energy through collisions.

In the plasma edge, the confinement times for these processes change on short length scales. As we do not know exactly where in the edge the ion tails exist, we must consider how the loss mechanisms will vary across the plasma edge.

4.2.1 Unconfined Orbits

A particle is unconfined if its orbit intersects a material surface. For the particles viewed by the PCX the relevant material surfaces are either the outboard limiter or the protection limiters on the sides of the antennas. As noted above, the banana

width and Larmor radius for particles in these highly energetic tails can be larger than the width of the SOL, causing particles originating at even the LCFS to be scraped off by the limiters.

For purposes of estimation, we will consider the lifetime of a particle on an unconfined orbit to be approximately one quarter of the bounce period, or $\tau_b/4$. For a 10 keV deuteron, this lifetime will be 23 μs. Recall that $\tau_b \propto 1\sqrt{\mathcal{E}}$ (Eq. 4.10).

4.2.2 Collisions

There are three types of particle collisions to consider: collisions with ions, electrons, and neutrals. At ion energies above a few hundred eV ion-neutral collisions will be charge exchange reactions; these are covered in the next section.

The canonical form for collision frequencies is[31]

$$\frac{dv_\alpha}{dt} = -\nu_s^{\alpha/\beta} v_\alpha, \tag{4.19}$$

$$\nu_s^{\alpha/\beta} = \left(1 + \frac{m_\alpha}{m_\beta}\right)\psi(\chi^{\alpha/\beta})\nu_0^{\alpha/\beta}, \qquad \nu_0^{\alpha/\beta} = \frac{q_\alpha^2 q_\beta^2}{4\pi\epsilon_0^2}\lambda_{\alpha\beta}\frac{n_\beta}{m_\alpha^2 v_\alpha^3},$$

$$\chi^{\alpha/\beta} = m_\beta v_\alpha^2/2T_\beta, \quad \psi(\chi \gg 1) \simeq 1, \quad \psi(\chi \ll 1) \simeq \frac{4}{3\sqrt{\pi}}\chi^{3/2}.$$

The condition $\chi \ll 1$ holds for tail ions colliding on electrons, and $\chi \gg 1$ for tail ions on thermal ions. Whether tail-ion or tail-electron collisions dominate depends on the energy of the tail ion in question. Using k to refer to tail ions, and assuming hydrogenic ions, the collision rates are

$$\nu^{k/i} = \left(1 + \frac{m_k}{m_i}\right)\frac{e^4}{4\pi\epsilon_0^2}\lambda_{ki}\frac{n}{m_k^2 v_k^3}, \tag{4.20}$$

$$\nu^{k/e} = \frac{m_k}{m_e}\frac{e^4}{3\pi^{3/2}\epsilon_0^2}\lambda_{ke}\frac{n}{m_k^2}\left(\frac{m_e}{2T_e}\right)^{3/2}. \tag{4.21}$$

Comparative plots of the different collision times are in Sec. 4.2.4.

4.2.3 Charge Exchange

The charge exchange reaction is described in Chapt. 2. Because the density of neutral hydrogen decreases rapidly in the SOL, the charge exchange rate has a strong spatial dependence. Tail ions have large banana widths and large Larmor radii, and will pass through regions of much higher neutral density then that at their guiding center/bounce tip. The actual neutral density is neither toroidally nor up-down symmetric[22].

4.2.4 Discussion

We consider all the above processes to estimate the time that a suprathermal ion will remain in a perpendicular tail. Ion-ion collisions do not remove ions from the plasma, but they do scatter them out of the tail.

Figure 4.3 shows the collision frequencies for the various processes described above in the SOL of shot 960829023. The x-axis is distance from the LCFS in mm at the midplane. The temperature and density profiles are taken from data obtained by the fast scanning probe, and are shown in Fig. 2.3. The neutral density is estimated from measurements by the PCX during the ohmic heating phase of the discharge. Simulations using a Monte-Carlo code show the neutral density in the SOL is approximately ten times that at the LCFS[32]. For this shot, the gap between the LCFS and the outboard limiter is 12 mm.

The plots in Fig. 4.3 show that loss by hitting the limiter is the fastest loss mechanism for particles in orbits that intersect the outboard limiter. Depending on radius and energy, this loss time is 3–100 times faster than for charge exchange, implying that only 1–30% of the fast ions charge exchange before hitting a limiter, and only this small percentage can be measured by the CX analyzer.

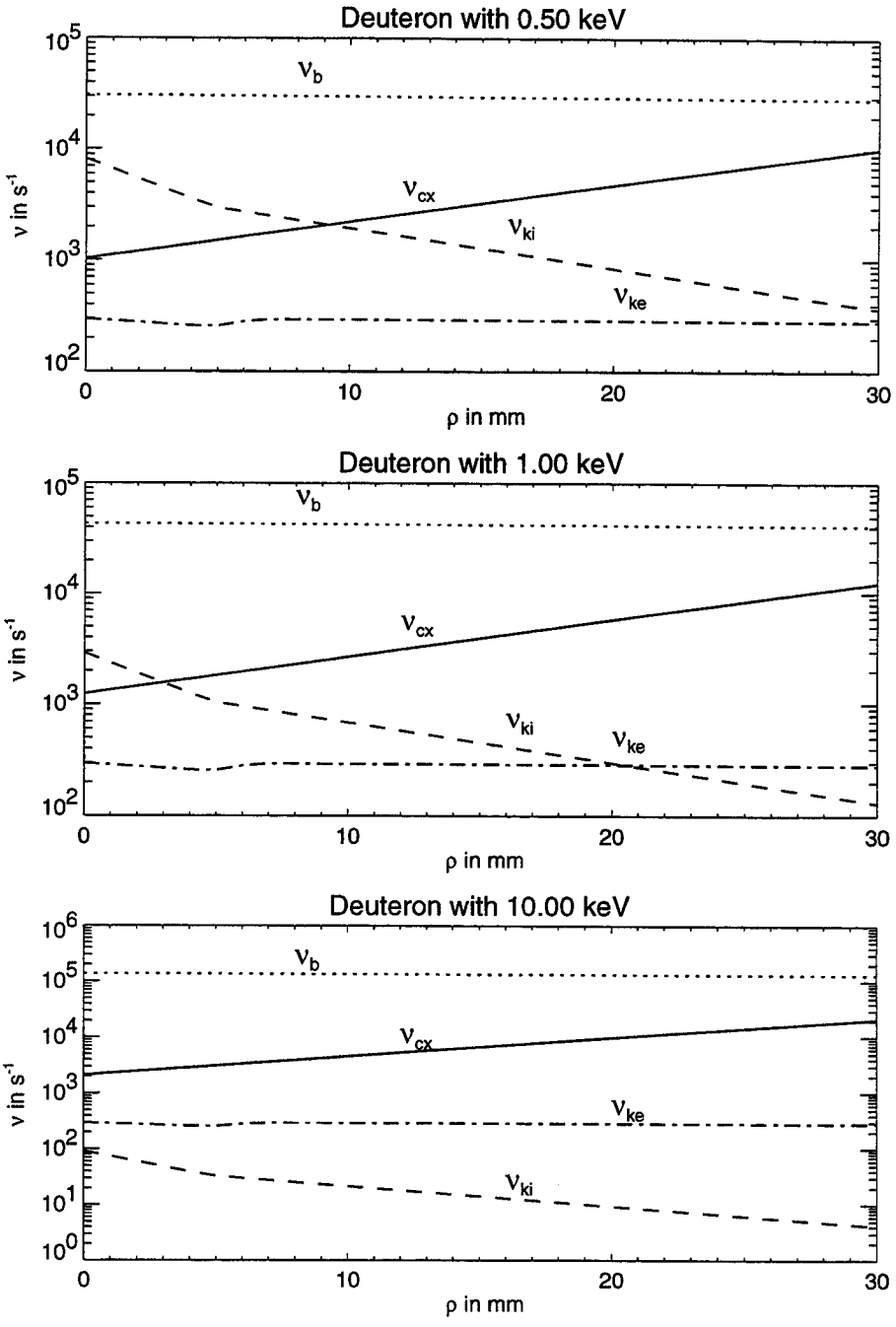

Figure 4.3: Collision frequencies for deuterons at 0.5, 1, 10 keV, showing bounce frequency (ν_b), charge exchange frequency (ν_{CX}), and frequencies for collisions with thermal ions (ν_{ki}) and electrons (ν_{ke}). X-axis shows distance from LCFS.

Because of the large Larmor radii and banana widths of the energetic edge ions under discussion, we will assume that their orbits intersect a limiter. In this case, the confinement time for energetic edge ions is on the order of tens of microseconds.

Chapter 5

Previous Observations of Edge Ion Heating

It has long been known that the interaction between particles and waves can lead to non-Maxwellian, non-isotropic velocity distribution functions[33]. The RF can add energy to a small part of the ion population, creating a "tail"[12]. An ion tail in the plasma center improves the damping of the fast wave, and, in a reactor, would increase the reaction rate.

Fast ion populations in the center of an ICRF heated tokamak were first observed on T-4[34]. A mass-resolving charge exchange diagnostic observed a large tail in the hydrogen population. The analyzer could only measure the perpendicular distribution function. Variations with pitch angle of the ion distribution function were first measured on PLT, using a scanning passive charge exchange analyzer[35]. Hydrogen tails in the main plasma during minority heating have been observed on many machines[30].

These results are important in understanding power absorption during minority ICRF heating in tokamaks. Indirect measurements of ion distribution functions near the plasma center are made, though extensive modeling may be necessary to under-

stand the results[36]. Certainly there are unresolved questions regarding the transport of the tail ions, including spatial diffusion of fast ions and response to transport events such as sawteeth.

In order to heat the plasma center, RF power must be coupled through the plasma edge. This coupling can be strongly affected by the edge conditions[6]. The strong RF fields can also interact with the edge plasma ions through various linear and non-linear mechanisms, and transfer energy to them. It is not surprising, then, that fast ions in the plasma edge have also been observed during ICRF heating on tokamaks. The mechanisms of edge ion heating and its possible effects will be discussed in Chapt. 7.

In particular, suprathermal ions have been reported on ASDEX, TEXTOR, JT-60, and Alcator C-Mod during fast wave heating, and on DIII-D during ion Bernstein wave heating.

During ASDEX experiments comparing optically-open and optically-closed Faraday screens, deuterons with large perpendicular velocities were observed when the antenna with the optically-open screen was used[37]. The tokamak was operated at 2.2 Tesla. The RF power consisted of up to 1.2 MW second harmonic hydrogen minority heating at 67 MHz. The plasmas were run in double-null configuration, with $R_0 = 1.67$ m, $a = 0.40$ m, $\bar{n}_e = (2-6) \times 10^{19}$ m^{-3}. The deuterium flux showed fast rise and decay times, 1–3 ms, and was very sensitive to toroidal field, leading them to conclude that the flux originated in the plasma edge. The tail began at energies of 4 keV. The flux showed large fluctuations uncorrelated with any macroscopic plasma parameter, including impurity production. The deuterium tail was measured using a charge-exchange analyzer midway between the two antennas, perpendicular to the magnetic field at the midplane.

Measurements were also made of fast particles using carbon implantation probes in the center of an RF antenna on ASDEX[38]. Each probe was exposed during one shot, and the depth distribution of particle implantation was measured using "elastic

recoil detection". Control probes, 1.5 m from the antennas, were also used. Particles with incident energy up to 15 keV were observed. The deposition of suprathermal ions was approximately twice as large for the probe in the antenna center compared to the control. However, the deposition on the control probe was ten times larger than the prediction based on measurements by the charge-exchange analyzer. From this they concluded that most of the particles striking the carbon probes were ions, not neutrals.

In the discussion of results from parametric decay instability investigations using RF probes on ASDEX, they suggested that PDI could be generating the fast ions. However, no evidence of correlation between edge heating observations and PDI as observed by RF probes was presented[39].

Investigations of edge effects during ICRF heating on TEXTOR showed the presence of fast ions in the SOL[40]. TEXTOR was operated at a toroidal field of 2.0–2.6 T, with $\bar{n}_e \leq 6 \times 10^{19}$ m^{-3}, $R_0 = 1.75$ m, $a = 0.45$ m, with limited, circular plasmas. Laser induced fluorescence was used to measure Fe atoms sputtered from a small, movable steel surface. From measurements at different plate positions they determined qualitatively that a population of fast ions existed in the SOL with 1.6 MW of ICRH at 29 MHz. The sputtering yield increased quickly, in less than 1 ms, compared to time scales for changes in the flux at the limiters or the bulk plasma parameters, around 100 ms. The increases in SOL temperature measured with probes were insufficient to account for the increased sputtering. RF sheaths were also ruled out. Further investigations indicated that the ion tails were in the perpendicular direction. Evaluation of measurements of heat flux to the limiters during ICRH showed changes in the heat flux too large to be accounted for by changes in n_e, T_e, and the parallel ion sound speed, indicating an increase in the perpendicular energy of ions in the SOL. No variations with plasma parameters or RF power were reported.

Fast ions were observed on the JT-60 tokamak with charge-exchange analyzers

during hydrogen minority heating[41]. JT-60 was operated with a divertor at the outboard midplane, with $B_T = 3.7 - 4.3$ T, $R_0 = 3$ m, $a = 0.93$ m. These measurements were made with 1.5 MW of RF power at an unspecified frequency in the range 110–130 MHz. The charge-exchange analyzer used was below the midplane on the outboard side with a sight line passing near the plasma center, and measured the flux of ions with energies of 3.9 keV and 5.6 keV. The CX flux "jumped" with the injection of ICRH, but only when the antennas were operated with (0,0) phasing. The jump in flux did not occur when the antennas were operated in $(0,\pi)$ phasing. Parametric decay into an ion cyclotron quasimode and an ion Bernstein wave was also observed with RF probes on these shots. The toroidal field was scanned at constant RF power, and the IBW amplitude and the jump in flux were found to be positively correlated, leading them to conclude that the parametric decay generated the energetic ions. Radiation losses from the plasma were also correlated with IBW amplitude, implying that the PDI led to increased impurities in the plasma.

On the DIII-D tokamak, experiments with direct-launch IBW heating of the plasma showed significant production of fast particles in the edge, as measured with a toroidally-scanning charge exchange analyzer at the midplane[42]. During these experiments $B_T = 1.0 - 2.1$ T and $\bar{n}_e = 0.7 - 5 \times 10^{19}$ m^{-3}. The IBW was launched at 36 or 38 MHz by a loop antenna with an opaque Faraday shield at powers up to 1 MW. While this experiment did not involve fast-wave heating, the antenna structure is similar to that of a fast-wave antenna, the ratio ω_{rf}/ω_{cD} is similar to that used in some of the Alcator C-Mod experiments, and their data is extensive. They found that edge ion heating only occurred in inner wall limited discharges with low densities ($\bar{n}_e \leq 3 \times 10^{19}$ m^{-3}), and not with higher densities, or in outer wall limited or diverted shots. Scanning the CX analyzer toroidally, they found no parallel ion heating. They observed perpendicular tails in both hydrogen and deuterium, with tail temperatures of 5.5 and 1.8 keV respectively, significantly higher than the 0.8 keV

bulk plasma ion temperature. The tails formed only at RF powers above 240 kW. The conclusion that these ions are generated in the edge was based on the fast rise and fall times, less than 1 ms, and that the appearance of the tail had no effect on the core ion temperature, plasma stored energy, or neutron production. During toroidal field ramps, the sizes of the ion tails were shown to peak strongly when the resonances $\omega_{rf} = 5\omega_{cD}$ and $\omega_{rf} = 4\omega_{cD}$ passed through the plasma edge.

These experiments measured parametric decay with an electrostatic RF probe located 50° toroidally from the RF antenna. The probe was located at the midplane at the same major radius as the RF antenna. The power thresholds for PDI and ion edge tail productions with $\omega_{rf} = 4\omega_{cD}$ near the edge were both found to be about 200 kW, and the tail amplitude was well correlated with the amplitude of the PDI decay waves. The PDI and tail production were sensitive to relative amounts of hydrogen and deuterium in the plasma.

While the focus of the present work is fast wave heating, it is worth noting that ion tails have been observed in conjunction with parametric decay on tokamaks using lower hybrid heating. On Alcator C[43], edge ion tails toroidally localized near the launcher were observed during LH heating using a CX analyzer. Ion tails in the bulk plasma caused by PDI were measured for the first time on the ATC tokamak[44].

The reported data regarding edge ion heating during ICRF heating on tokamaks leaves several issues unresolved. There is no record of these observations on several major experiments, including JET and TFTR. This may mean that no diagnostic was used which would be sensitive to energetic ions in the edge, or that they were not monitored. Also, the reported data are inconsistent regarding impurity production during edge ion heating. The control of impurities is crucial to tokamak reactor operation, and clarification of the role of edge ion tails is important.

The observations from different machines do have important similarities. Edge tail production appears sensitive to the antenna geometry, the edge conditions, and

the magnetic field. Of course, there are several mechanisms by which edge ion heating can occur (as described Chapt. 7), and the particular mechanism operating in any one of these experiments is not necessarily that which is occurring in the others, or in Alcator C-Mod.

Chapter 6

Observations of Edge Ion Heating on Alcator C-Mod

6.1 Introduction

This chapter describes our observations of edge ion heating in Alcator C-Mod and an analysis of its effects on the plasma. The rest of the present work will study possible causes of the edge ion heating on Alcator C-Mod.

This chapter serves three purposes. First, it defines and describes the phenomena of edge ion heating as observed on Alcator C-Mod. Second, it presents details which will be important in later chapters as comparisons to possible edge-heating mechanisms are analyzed. Third, it details the effect edge ion heating has on the rest of the plasma.

The perpendicular charge exchange analyzer was installed on Alcator primarily to measure the central ion temperature, and more generally the distribution functions of hydrogen and deuterium in the plasma interior. The latter are particularly important in analyzing ICRF heating results[36]. The PCX takes data on essentially every plasma shot. In certain cases, the PCX has measured ion temperatures in ohmically

heated plasmas, but in general the plasma is too dense, leading to high attenuation (see Sec. 3.1.2), which reduces the energetic particle flux from the plasma center to below-measurable levels.

During RF heating on Alcator C-Mod, the PCX often records a sudden large increase in signal coincident with the RF pulse. The signal represents a large flux of neutrals in the energy range the PCX, usually on the order of 1 to 20 keV. Because the flux includes neutrals with energies well above the plasma temperature, we refer to them as energetic neutrals. The energetic neutrals arise via charge exchange from ions in the plasma. These ions are referred to as suprathermal, and make up an ion tail, that is, a high energy component to an otherwise Maxwellian distribution function.

There is a specific set of characteristics that define the jump in neutral flux: the fast rise and decay times; the lack of correlation with macroscopic plasma parameters; and the sensitivity to edge plasma conditions (Sec. 6.2). Analysis of these characteristics leads to the conclusion that the energetic ions are located in the plasma edge. Specifically, some effect related to the RF heating generates highly energetic ions in the plasma edge, and these ions charge-exchange and escape the plasma as energetic neutrals. In the present work, "edge heating" refers to the generation of suprathermal ions in the plasma edge during RF power injection.

The properties of edge ion heating depend on the RF heating regime. During hydrogen minority heating, there is a threshold electric field for edge heating (Sec. 6.3). If the magnetic field is at a value such that the RF frequency is an exact cyclotron harmonic in the plasma edge, large edge heating at low RF power is observed (Sec. 6.4). At the transition from L-mode to H-mode, the plasma edge changes, and this is reflected in the energetic neutral flux (Sec. 6.8).

Theoretically, edge ion heating may affect the efficiency of RF heating. The edge heating seen on C-Mod, however, has no effect on the coupling of RF power to the

plasma (Sec. 6.7) and it is not a significant channel of parasitic power loss (Sec. 6.9). It also does not lead to an increase in the level of impurities in the plasma (Sec. 6.6).

6.2 Identification as Edge Heating

As discussed in Chapt. 3, the PCX is sensitive to neutrals generated at any position along its sight line, and the flux measured can be written as a line integral, as in Eq. 3.6. The radial location of the source of any particular particles must be inferred. There are three characteristics of the particle flux that indicate that the energetic ions are being generated in the plasma edge: (i) the fast time scale, (ii) the slope of the flux, and (iii) the dependence on edge conditions.

6.2.1 Time Scale

On some discharges, the PCX records an increase in the flux of suprathermal neutrals of up to a factor of 10^3 when the RF power turns on. The increase occurs on time scales shorter than 0.2 ms (the PCX time resolution), much faster than changes in the core ion and electron temperatures, which typically change on a time scale of 10 ms. The decay time after the RF power turns off is similarly short. Again, in the center, the temperatures decay over tens of milliseconds.

As described in Chapt. 4, and shown in Fig. 4.3, particles in the SOL with energy in the keV range can have particle confinement times less than 0.1 ms. The short decay time of the increased flux is typical of times in the plasma edge, rather than the plasma center.

6.2.2 Tail Temperature

The agreement between spectroscopic and neutron-rate measurements of the plasma central ion temperature shows that the distribution function of the majority ion

species in the plasma remains nearly an isotropic Maxwellian during ICRF heating on Alcator C-Mod. Line widths in the atomic spectra of impurities in the plasma center measure the spread in energy of the distribution function. The impurity ions are strongly coupled to the bulk ions via collisions, and have the same temperature. The neutron production rate (for D-D reactions) increases with energy, so total neutron production is in effect a measure of a higher order moment of the distribution function, and is therefore particularly sensitive to suprathermal tails. Ion temperature is calculated from the neutron production using the assumption that the deuterium distribution function is a Maxwellian. The two measurements of central ion temperature generally agree, implying the deuterium distribution function is a Maxwellian.

During the jump in flux, the value of T_{tail} inferred from the neutral flux (as defined in Sec. 3.3) shows no relation to the bulk ion temperature as measured by other diagnostics. In shot 960227042, shown in Fig. 6.1, the deuterium flux shows a large jump at the beginning of RF injection, before the ion temperature begins to rise. The tail temperature is 4.5 keV (see Fig. 6.2) at 0.8 s, when the ion temperature is 3 keV. On this shot, the sight line of the PCX passes 0.21 meters below the center of the plasma ($r/a > 0.5$ mapped to the midplane), where the ion temperature is more than a factor of two lower than at the center.

The difference between the PCX T_{tail} values for the bulk species and the central ion temperature indicates that the tails observed by the PCX are not occurring in the interior of the plasma.

6.2.3 Dependence on Edge Conditions

The ion tails' strong dependence on the edge conditions is revealed in two situations, H-modes and toroidal field ramps.

One of the results of the plasma transitioning into H-mode is an immediate change in the temperature and density profiles of the plasma in the scrape off layer[45][46][47].

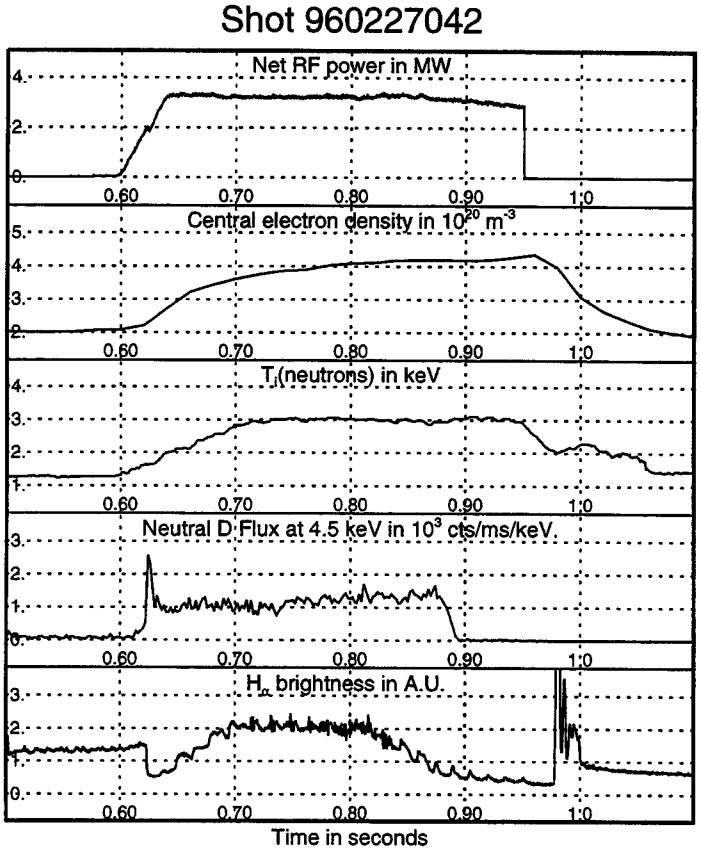

Figure 6.1: Edge heating during ICRF heating. Note PCX signal rises in 4 ms and remains constant, while the central ion temperature rises over 100 ms. Cutoff in PCX signal at 0.88 seconds is due to the PCX gate valve closing early.

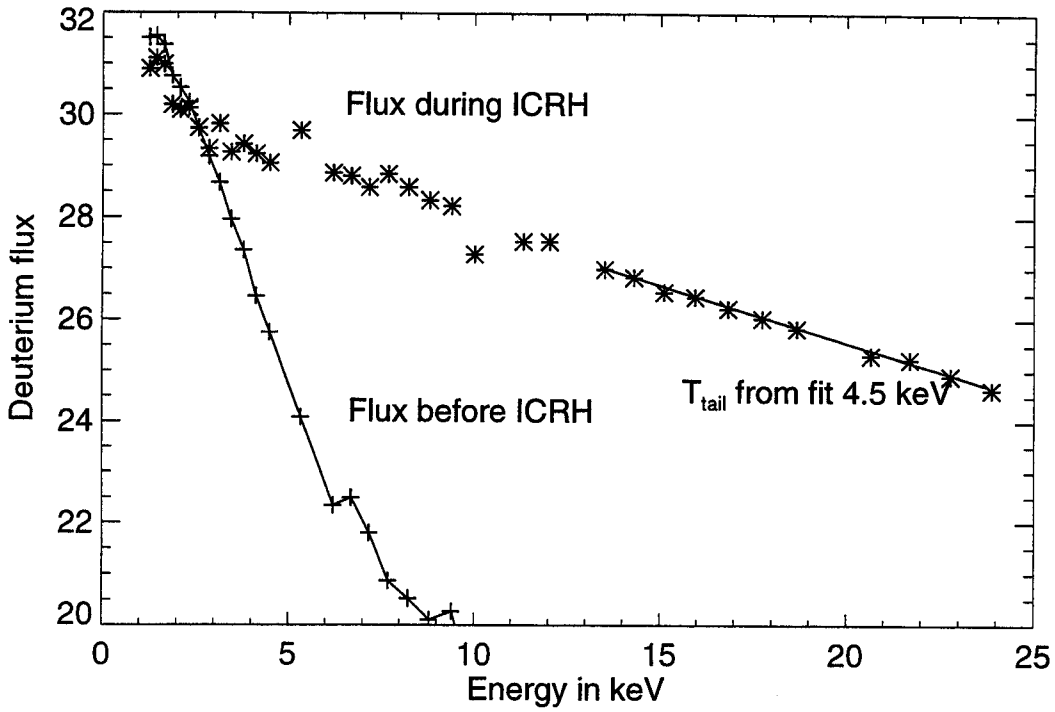

Figure 6.2: Deuterium flux, $\ln \hat{f}(\mathcal{E})$, before and during edge heating by ICRF heating.

The gradients steepen, so that the temperature and density outside the LCFS drop. The H-mode may be accompanied by fluctuations known as edge localized modes (ELMs), which further modify the edge profiles.

Figure 6.3 shows an example of changes in the ion tails correlated with changes in the plasma edge. The RF power turns on at 0.7 s, with only a small increase in the flux of 5 keV neutrals. However, at 0.74 s the plasma transitions into H-mode, as shown by the abrupt drop of the H_α signal, and the neutral flux at 5 keV increases by an order of magnitude. The neutral flux drops back down in less than 2 ms at 0.76 s when the RF pulse turns off. It appears that the change in the edge parameters at the H-mode transition change the susceptibility to ion tail generation. The ion tail is still only observed while the RF power is on, however. The effect of an H-mode on edge ion heating is further discussed in Sec. 6.8 of this chapter.

At low RF power, edge ion heating is sensitive to small changes in the toroidal

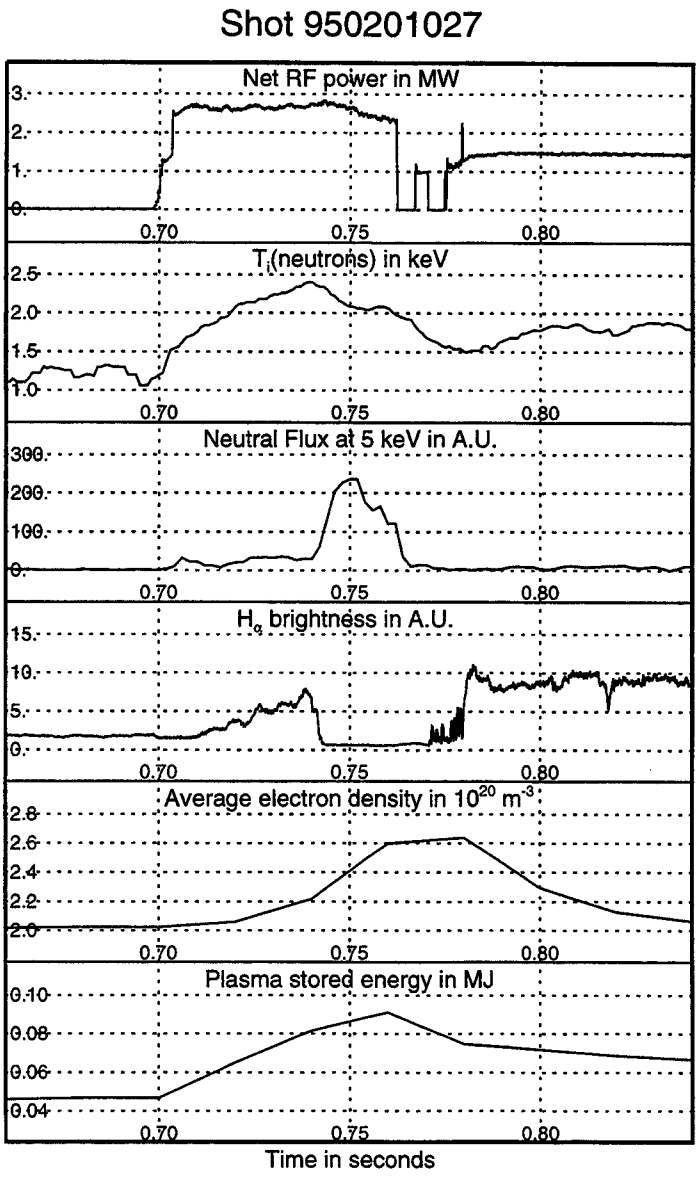

Figure 6.3: Change in neutral flux with H-mode

magnetic field. Figure 6.6 shows large changes in the energetic neutral flux with small changes in the toroidal magnetic field. The peaks, which are reproducible, can have FWHM as narrow as 1% in B_0 or less. As discussed more fully in Sec. 6.4, these peaks in the energetic neutral flux occur when the RF frequency is at a cyclotron harmonic in the edge. That is, when the magnetic field changes, the cyclotron frequency ω_{ci} also changes, and when $\omega_{rf} = \ell\omega_{ci}$ in the SOL, large ion tails are observed by the PCX.

This strong dependence on edge conditions suggests that the ion tails are located in the plasma edge.

6.3 Edge Heating during H Minority Heating

Hydrogen minority heating at 5.3 T is the heating scheme most often used on Alcator C-Mod. The high efficiency and the high powers available make it very attractive for use on future machines and reactors[2]. Consequently, it is particularly important to determine the prevalence and effects of edge ion heating in this regime.

Edge heating, as described above, is observed on some shots at this value of toroidal field. We examined the data from 298 shots at 5.3 T with ICRF heating for evidence of edge ion heating. These shots occurred between 12 January 1995 and 9 June 1995.

6.3.1 Scatter Plots

Scatter plots were used to search for thresholds and their possible parametric dependences. On the plots, each symbol represents a single shot, and indicates whether edge heating was observed on that shot, as characterized by the fast jump in the energetic neutral flux.

Several examples of scatter plots generated from the data are shown in Fig. 6.4.

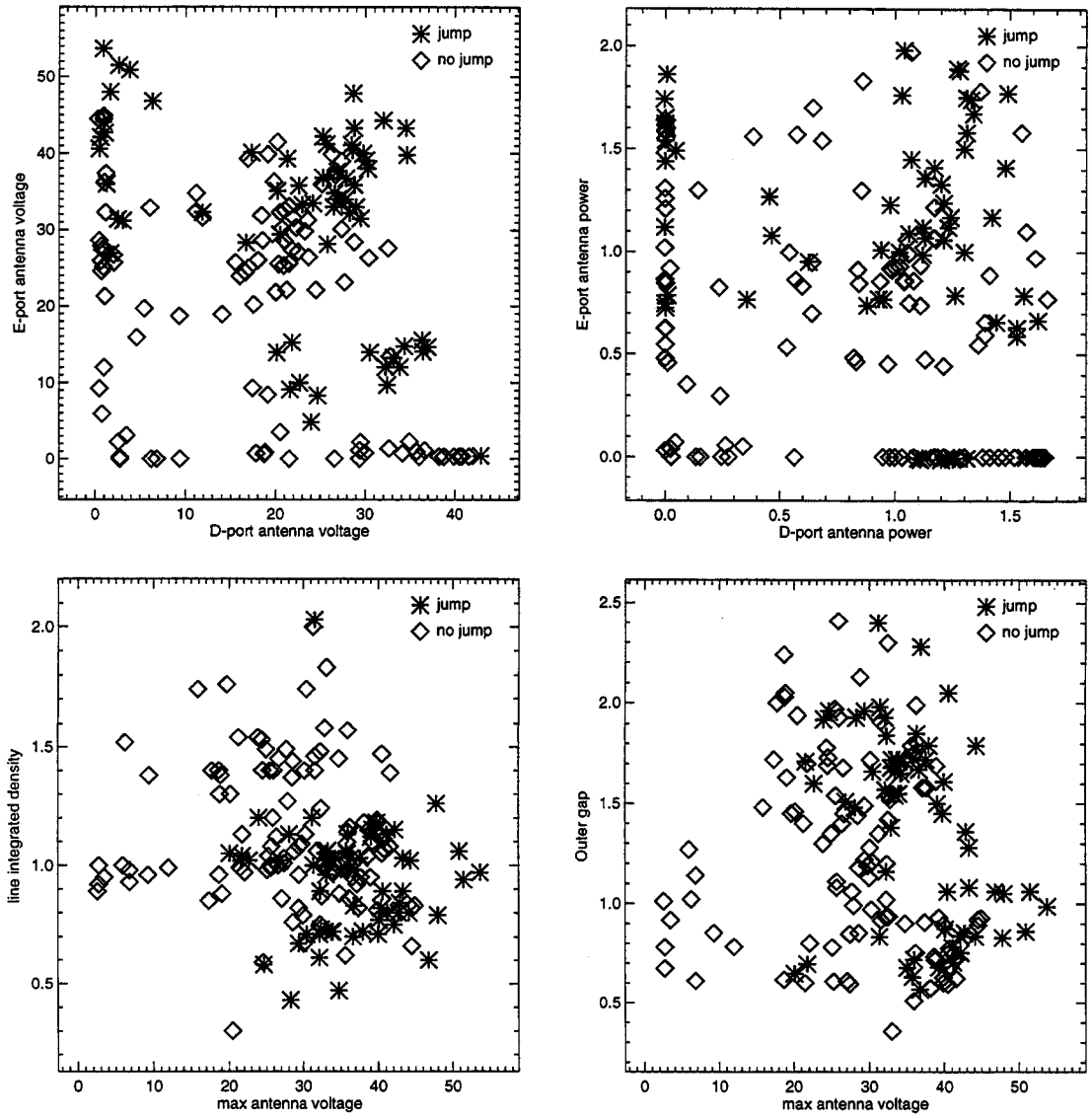

Figure 6.4: Scatter plots of flux jumps at 5.3 T

The top two plots give information about the minimum threshold for edge heating. On the top right plot, the axes show the RF power from each antenna during RF heating. This plot shows that edge heating is only observed if RF power launched by the E-port antenna is greater than 0.7 MW or D-port power is greater than 1.1 MW. On the top left plot, the axes are the antenna voltage in kV. This shows a threshold of 25 kV on the E-port antenna, or 20 kV on D-port. These plots show that edge ion heating is not an effect of the *total* RF power injected into the plasma.

The relation between voltage and power is not the same for the two antennas because of variations in their construction. It is interesting that the apparent power threshold for edge heating is at very different power levels for the two antennas, but at almost the same voltage. This strongly suggests that the edge heating is caused by the electric field local to an antenna. The relationship between antenna voltage and electric fields around the antenna is described in Sec. 2.2.3.

The term "threshold" may be misleading, because there is apparently not a firm limit above which edge heating is always observed. It is reasonable to investigate other plasma parameters that may have an effect on edge heating.

To be consistent with the conclusion that it's the maximum voltage that matters, the other two scatter plots use the higher antenna voltage as an axis.

If the edge heating is purely a result of conditions at the plasma edge, then the parameters to investigate are such things as edge temperature, density, impurities, and so on. However, measurements of these quantities in the SOL are not available for most shots. If we suspect that the edge heating is related to the core plasma, say via poor central RF absorption, or that the relevant edge parameters are strongly linked to core parameters, then searching for a parametric dependence of the RF voltage threshold should prove fruitful.

The plasma parameters examined include plasma current, line-integrated density, central electron temperature, gap between the LCFS and limiter, Z_{eff}, and Ratiomatic

neutral density.

The two lower scatter plots show examples. None of the parameters examined showed a clear effect on the voltage threshold. Density, shown on the lower left graph, shows a tendency for edge heating not to occur at values above 1.2×10^{20} m^{-2}, but there are many shots below this density that do not show a jump in the flux. Similarly, on the plot of maximum voltage versus outer gap, on the lower right, edge heating appears to be more frequent at larger gaps. Neither of these conclusions is very strong. Any effect of other parameters is even weaker than in the two cases shown here.

The conclusion must be that edge heating depends on the antenna voltage and on one or more other parameters poorly represented by the available measurements. We believe that quantities such as density and temperature, even at the LCFS, should be strongly related to the core values, but this is not true of density and temperature in the outer SOL, near or outside the limiter radius. The poor correlation of edge heating with core temperature and density may reflect its sensitivity to the plasma parameters in the outer SOL.

6.4 Resonance at Plasma Edge

At certain values of the magnetic field the threshold for edge heating is much lower, less than 10 kW. The low threshold is seen where there is an ion cyclotron harmonic in the plasma edge, that is when $\omega_{rf} = \ell eB/m_i = \ell\omega_{ci}$ (integer ℓ) with B evaluated at the plasma edge. If the PCX sight line is horizontal through the midplane, then the "edge" is near 0.91 m, outside the last closed flux surface.

Even though none of the standard C-Mod heating schemes places an ion cyclotron resonance in the plasma edge, this regime is interesting for several reasons. Because significant edge ion tails are generated at low RF power, this regime is ideal for

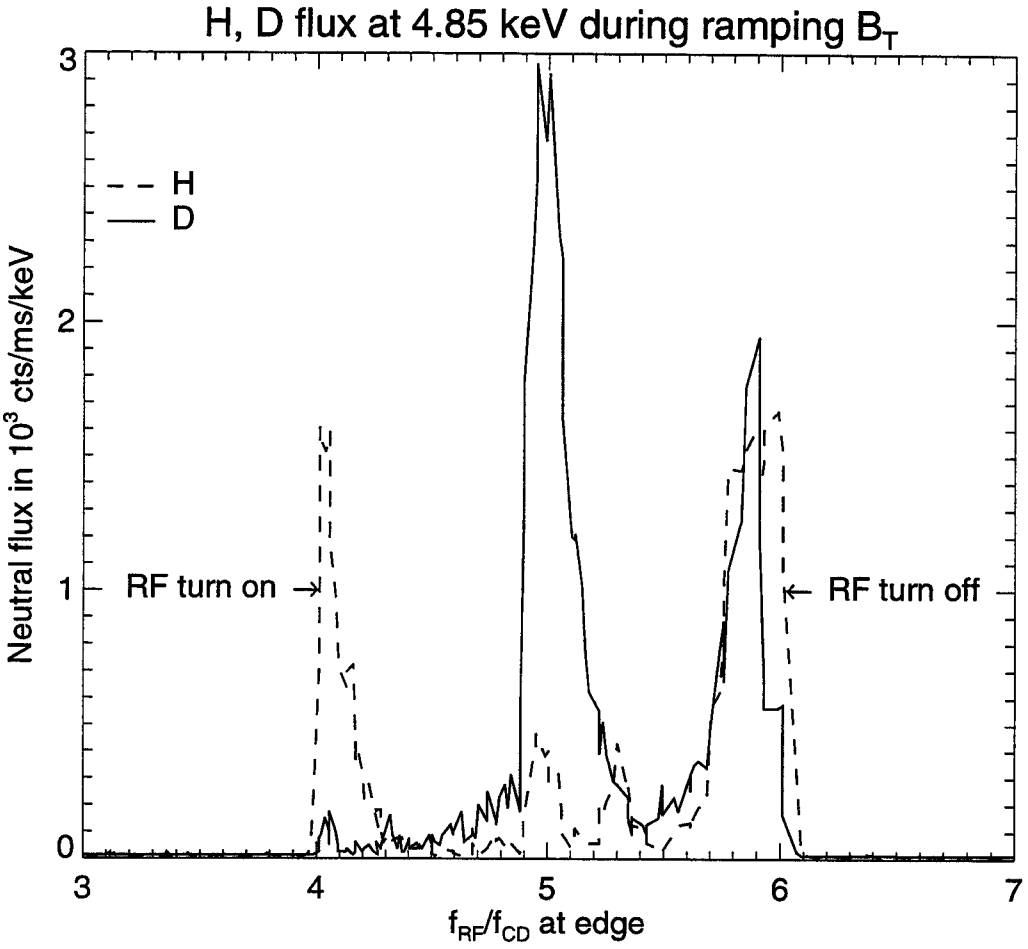

Figure 6.5: Hydrogen and deuterium flux during a TF ramp. Drop in D signal at 0.59 is due to a 50% drop in RF power.

studying the effects of the edge heating on RF coupling (see Sec. 6.7) and impurity generation (see Sec. 6.6). Low-power RF shots are also more reproducible, making this regime useful for making scans in PCX sight line and RF power. A higher percentage of RF power is deposited in the edge as well.

6.4.1 Toroidal Field Ramps

Figure 6.5 shows hydrogen and deuterium flux during a toroidal field ramp at constant RF power. The relative magnitudes of the flux signals are correct. During ICRF injection, B_0 ramps from 3.46 to 2.30 T, moving three deuterium cyclotron resonances

through the outboard edge of the plasma. In this sense, a cyclotron resonance occurs at radius R if

$$\ell \frac{eB(R)}{m_D} = \ell\omega_{ci} = \omega_{rf} \tag{6.1}$$

for integer ℓ. The resonances therefore are defined with respect to the frequency of the RF heating wave. For example, because the RF frequency on Alcator is 80 MHz, the third cyclotron harmonic occurs where $B(R) = 3.5$ T. Because $B(R) \simeq B_0 R_0/R$, the radial location of the third deuterium cyclotron harmonic is

$$R \simeq \frac{B_0 R_0}{3.5\mathrm{T}}.$$

Thus ramping the toroidal field strength has the effect of moving the radial locations of the cyclotron resonances. At odd harmonics, that is when Eq. 6.1 is satisfied with an odd integer l, the deuterium signal is larger than the hydrogen signal, while the hydrogen signal is larger at even harmonics. These peaks and the relative heights of the hydrogen and deuterium flux are reproducible.

This shot also shows a small peak where $\omega_{rf} = \frac{8}{3}\omega_{cH}$. The cyclotron frequency for a species depends on the charge-to-mass ratio, q/m, so this peak may correspond to a cyclotron resonance of an impurity species, such as O^{6+}. This peak and others at fractional harmonic numbers are observed only occasionally.

The data in Fig. 6.5 was taken with the PCX analyzer horizontal through the midplane. Figure 6.6 shows data taken during TF ramps with the PCX scanned to various poloidal locations. The sight line for each shot is shown to the left, overlaying the plasma and vacuum vessel surface. The structure of the signals, namely the multiple peaks, was observed regularly.

In this form, the figure only indicates that away from the midplane, edge heating occurs at lower B_0. To put this in a more useful form, we calculate for each sight

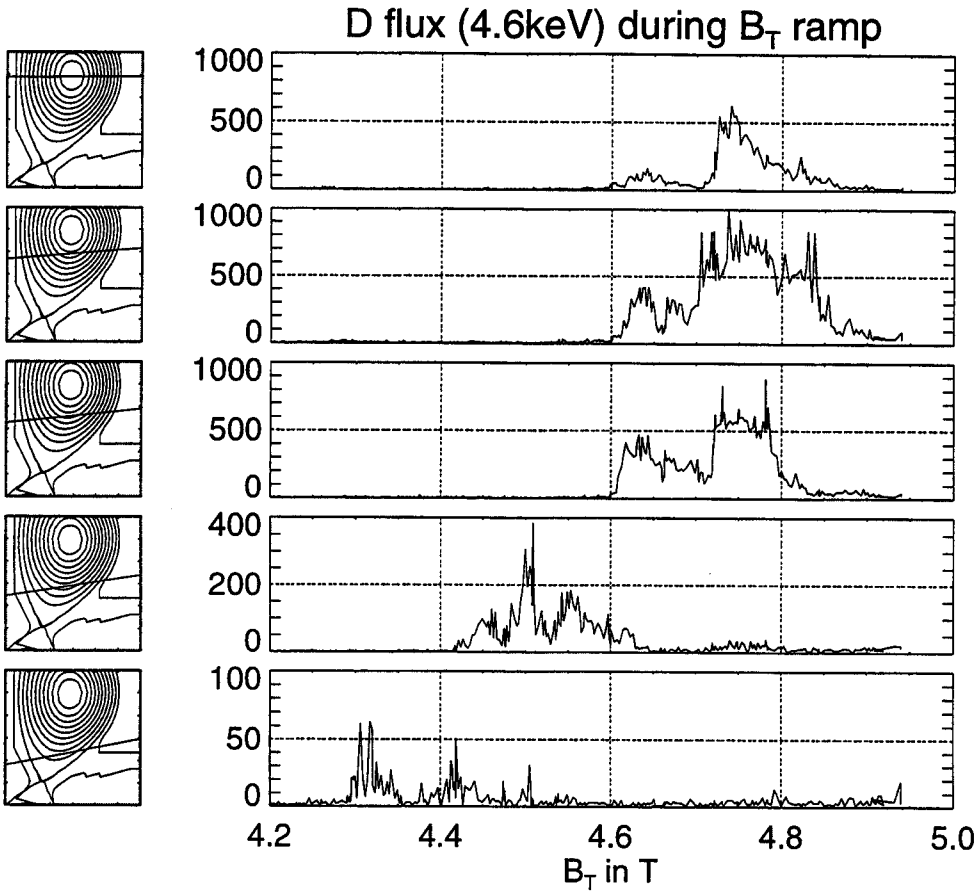

Figure 6.6: Poloidal scan of PCX flux during TF ramp

line the radius of the resonance layer as a function of time. Because we want to know this to accuracy of better than 1%, we need to include several terms in addition to the basic $1/R$ dependency of the toroidal field. We correct for the TF ripple (as described in Sec. 4.1.1) and the contribution of the poloidal field. Particles observed at different sight lines in the poloidal scan do not have velocities purely perpendicular to the magnetic field. As particles accelerated by RF waves at a cyclotron resonance gain mainly perpendicular velocity, for each sight line we calculate the radius at which the particles observed have purely perpendicular velocity, that is, R_b as described in Sec. 4.1.2.

The result of this transformation is shown in Fig. 6.7. The bottom plot of the stack of six panels shows flux surfaces, PCX sight lines, and the limiter. The dashed lines are the flux surfaces out to the LCFS, and the dotted lines are flux surfaces outside the LCFS. The heavy line represents the RF protection limiter, and the thinner nearly-horizontal solid lines show the four sight lines used in this scan. The x-axis is now radius of the resonance layer in meters. Note that in the bottom plot the vertical axis has been compressed. These plots show clearly that the largest CX flux for all the sight lines occurs when the resonance is just outside the limiter. This is particularly clear in the case of the lowest sight line, where the limiter does not follow a flux surface closely.

There are more hidden assumptions involved in making this plot. We have not yet justified why the $\omega_{rf} = \ell\omega_{cD}$ surface is of any interest. Perhaps we should be concerned with the radius where $\omega_{rf} = (\ell + 0.1)\omega_{cD}$, or something else. Without having presented any theoretical cause for the edge heating, the only justification is our intuition that interactions between particles and RF waves will occur at cyclotron resonances. These theoretical considerations will be presented later in Chapt. 8. As partial justification, recall that the plots show that the flux jumps occur when the resonance crosses the limiter radius to better than 0.5% in major radius. This con-

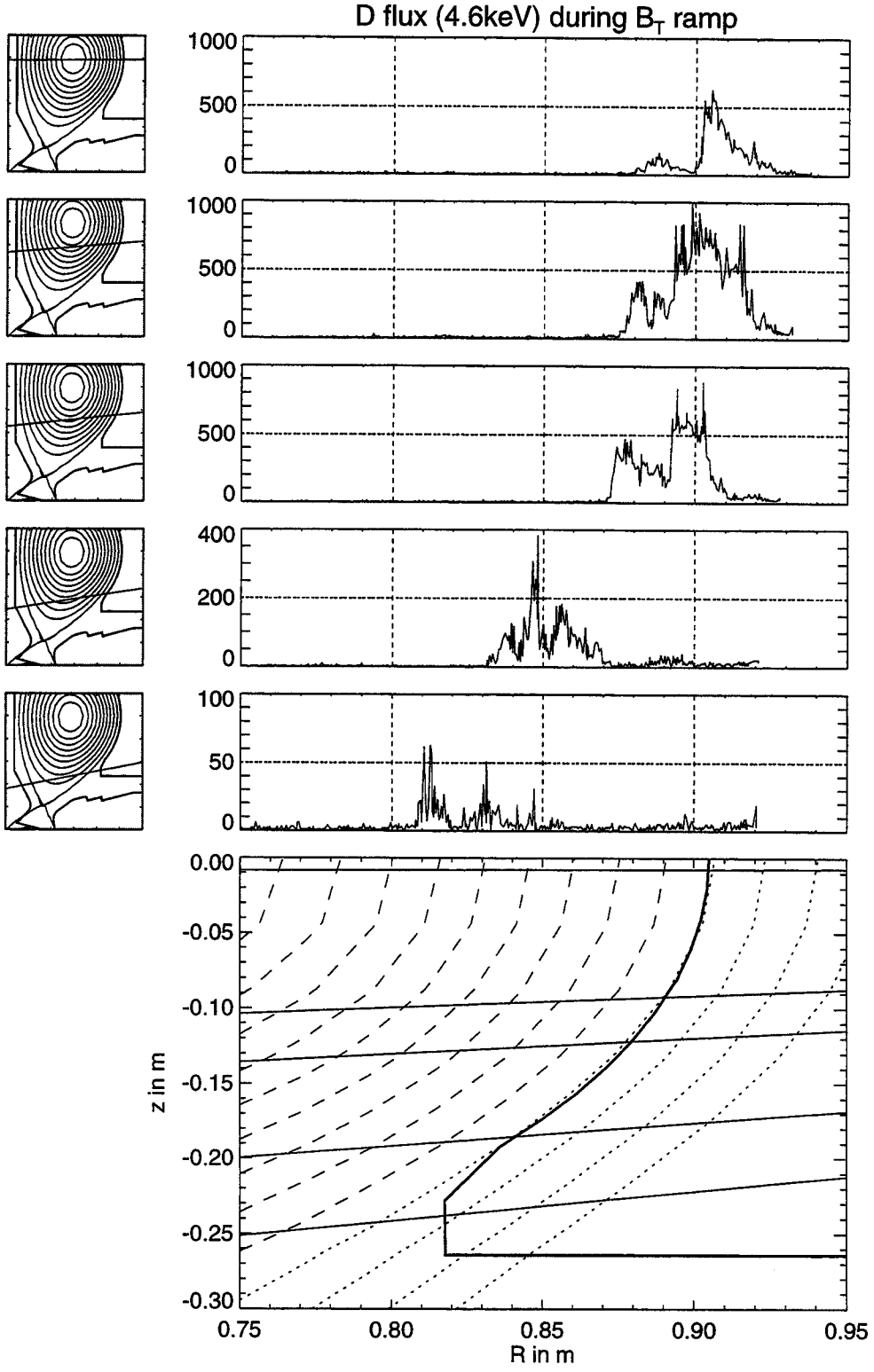

Figure 6.7: Poloidal scan of PCX flux vs. resonance radius. Bottom panel shows flux surfaces (dots and dashes), limiter (thick), and PCX sight lines (thin)

tinues to be true even at the lowest sight line where the spacing between the flux surfaces (along the sight line) is significantly different and the limiter does not follow a flux surface. This makes the connection extremely likely, though not proven.

6.4.2 Scans in RF Power

As mentioned above, shots with a resonance in the edge show large edge heating at low RF power and are reproducible. With the toroidal field in the plasma center set to 4.71 T, we performed scans in RF power during poloidal and toroidal scans of the PCX sight line.

From the neutral flux as a function of energy thus obtained we calculate quantities that have a more intuitive interpretation. The tail temperature is found as described previously by fitting a line to $\ln \hat{f}$ between the energies of 1.5 and 3.5 keV. Estimates of the power deposition during these scans are described in section 6.9.

The plots in Fig. 6.8 show the tail temperature at a given sight line as a function of RF power, and T_{tail} as a function of sight line at a given power.

It is important to point out that the particles viewed on the various sight lines have significantly different orbits. When the PCX scans toroidally, the actual point of the plasma viewed changes only by a few cm, but the tips of the bounce orbits change from being near the outboard midplane in front of the PCX analyzer to directly in front of the RF antennas. Particles that have their bounce tips, for example, directly in front of the antenna will cross the midplane at different toroidal locations with different pitch angles. So when we observe a change with toroidal angle, it may represent a toroidal asymmetry more than a characteristic pitch angle dependency.

During toroidal scans, we observed significant ion tails only at pitch angles corresponding to banana orbits, not passing orbits.

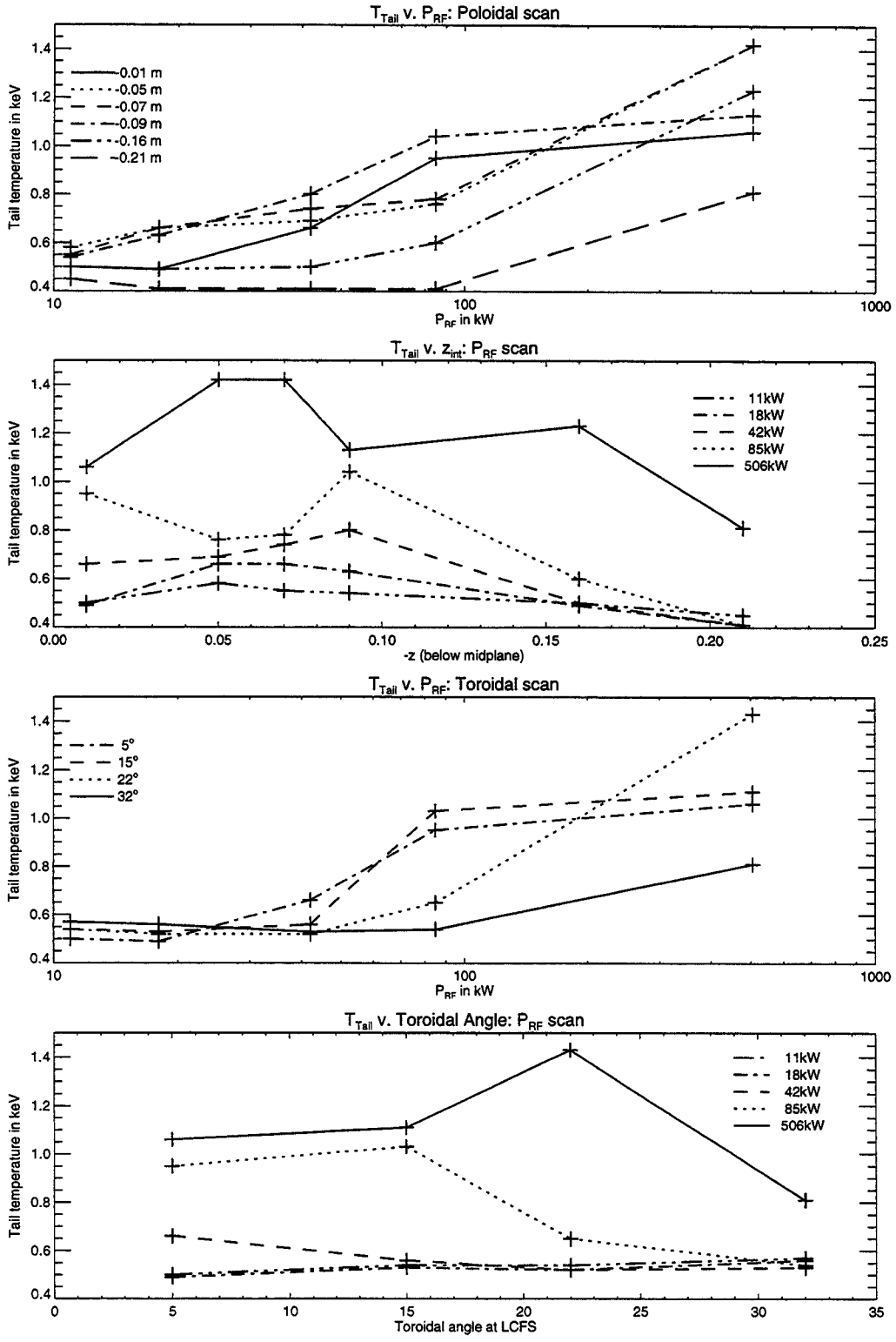

Figure 6.8: T_{tail} vs. RF power and sight line

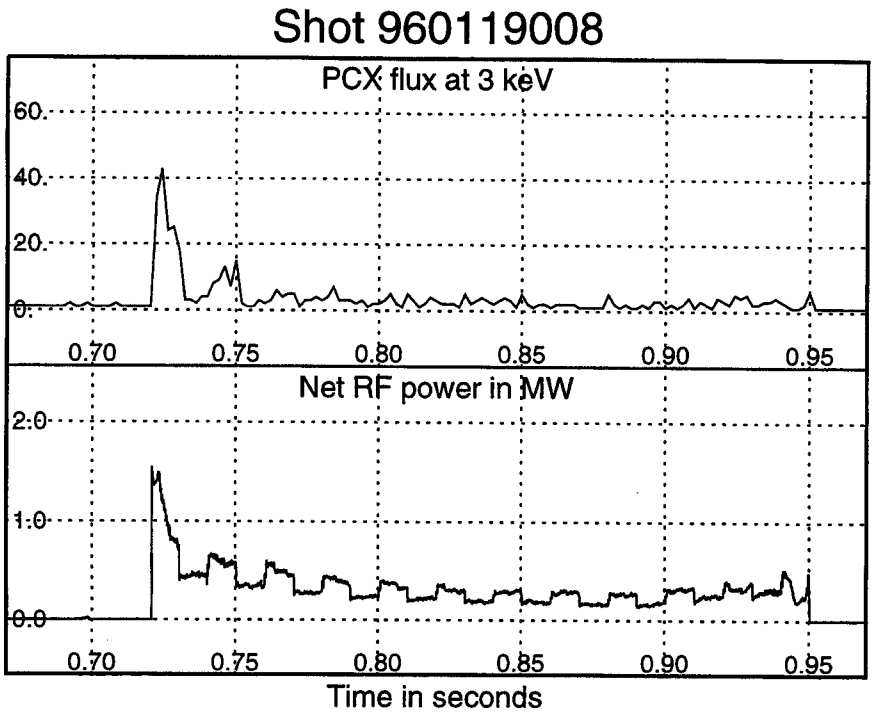

Figure 6.9: PCX neutral flux and RF power with $B_0 = 6.5$ T

6.5 ICRF Heating at 6.5 T

Alcator C-Mod is operated with a toroidal field of 6.5 T when using mode-conversion heating. While there is much less data in this regime, edge heating is observed with a threshold approximately the same as that observed at 5.3 T. In the shot shown in Fig. 6.9, the RF power was turned on and off quickly, but at varying power levels. Edge heating occurs only when the power reaches above 500 kW.

6.6 Impurities

Impurities, referring to any non-hydrogenic species in the plasma, reduce central plasma temperatures by line radiation and bremsstrahlung, can destabilize magnetic equilibria, and dilute the density of hydrogen species[48]. Experiments on JT-60[41] showed a strong correlation between edge heating and increases in impurity levels in

the plasma. The importance of impurities in tokamak operations and a possible link between edge heating and impurity generation compel study of a similar possible link on C-Mod.

6.6.1 Toroidal Field Ramps

In order to determine whether edge ion tails contribute to impurity generation during RF heating, we examined shots which have high levels of edge heating at relatively low RF power. This occurs when the RF frequency is an ion cyclotron harmonic in the plasma edge.

When a resonance layer is moved through the plasma edge by ramping the toroidal field, the flux of energetic neutrals increases by orders of magnitude. If either the energetic ions in the plasma edge or the escaping neutrals caused impurities to be sputtered or desorbed from the vessel walls, we would see an increase in impurities at the same time.

Figure 6.10 compares two shots with similar levels of edge heating, but greatly different RF power. The diagnostics used are described in Sec. 2.3.3.

The shot on the left has up to 2.7 MW of RF power injected into the plasma. During RF heating, the percentage of radiated power increases, as do the levels of molybdenum, showing that impurities are being generated. Note that on this shot the plasma does *not* transition into H-mode, because the toroidal field is reversed.

During the shot shown on the right, the toroidal field is ramping, moving a cyclotron harmonic through the plasma edge around 0.65 seconds. The edge heating is similar in magnitude (the PCX settings are identical) even though only 90 kW of RF power is injected. There is clearly no change in radiated power or molybdenum signals that would indicate that impurities are being generated.

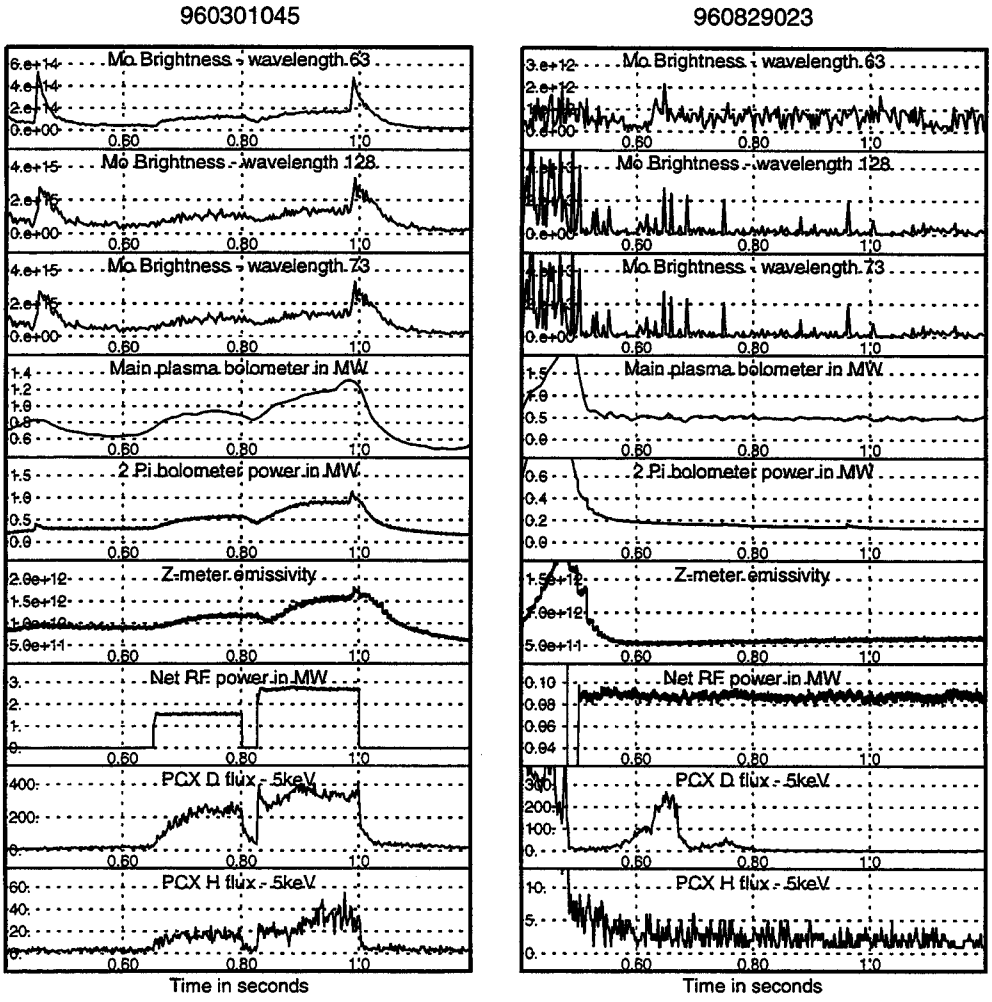

Figure 6.10: Spectroscopic measurements during edge heating, at high and low RF power, showing impurities uncorrelated with edge heating.

6.6.2 Results

These shots are characteristic of many examined, demonstrating that there is no correlation between edge heating and impurity generation. That edge heating does not contribute to impurities in Alcator C-Mod is in distinct contrast to measurements made on JT-60[41], which showed that edge ion heating caused measurably raised impurity levels.

6.7 RF Loading and Heating Efficiency

The shots described above are also ideal for looking at the effect of edge ion tails on coupling the RF power to the plasma. The coupling of RF power from the antenna to the plasma is believed to depend significantly on the characteristics of the edge plasma[6], and so may deteriorate with edge ion heating.

The primary measure of the coupling is the loading resistance seen at the antenna. Figure 6.11 shows traces for the E port antenna taken during a toroidal field ramp at constant RF power. This shot is characteristic of many shots with toroidal field ramps.

As the plot shows, the edge heating has no effect on the loading. This is an important negative result; the edge ion tails do not detrimentally affect the RF coupling.

6.8 H-modes

The H-mode is a regime of high confinement in which energy transport at the plasma edge is reduced[45], and has been observed on many machines. A fusion reactor may have to operate in a higher confinement regime such as H-mode to reach ignition. The major indications that the plasma has entered H-mode are a sudden drop in D_α emission and changes in the slopes of the time traces of the plasma central density

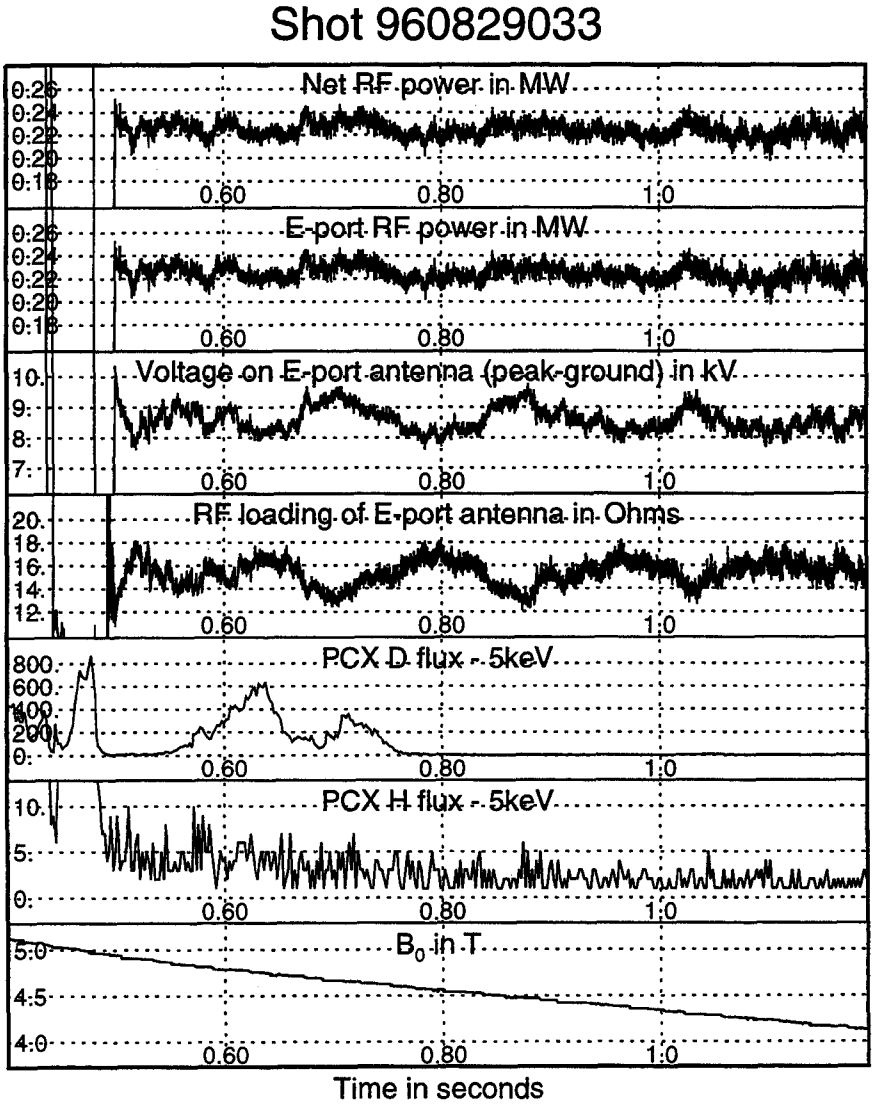

Figure 6.11: RF loading during edge heating.

and temperature.

MHD events called edge localized modes (ELMs) are sometimes observed during all or part of an H-mode. ELMs increase the average transport across the LCFS, but not up to L-mode levels[47][45].

6.8.1 Changes in Edge due to H-mode

Significant changes in the density and temperature profiles at the plasma edge as the plasma enters H-mode are observed on many machines, including Alcator C-Mod[46]. Profiles outside the LCFS are measured with an array of fast-scanning Langmuir probes[47]. When the plasma transitions to H-mode, density and temperature increase inside the LCFS, while they decrease in the SOL. The changes in the density and temperature profiles also affect the penetration of neutrals into the plasma.

The changes in edge heating with H-mode indicate that the edge heating is indeed occurring in the SOL. Two different kinds of changes in edge heating are observed with H-mode. On some shots, the flux increases sharply when the plasma enters an ELM-free H-mode. On some other shots, the flux starts to increase slowly, with a time scale of tens of milliseconds, peaking when the plasma enters H-mode.

6.8.2 Fast Jump at Transition

Figure 6.12 shows data from shot 960220007. The trace of D_α light indicates that the plasma enters an ELMy H-mode at 0.82 s and changes between ELMy and ELM-free several times. The ELMy periods are seen on the D_α signal as small increases in emission with observable fluctuations. Looking at the deuterium flux at 1.8 keV, the flux doubles when the RF turns on, but there is little effect on the flux at higher energies. When the plasma enters an ELM-free H-mode, the flux at 3.4 keV and 6.5 keV increases significantly. The fluxes drop rapidly when the H-mode becomes ELMy.

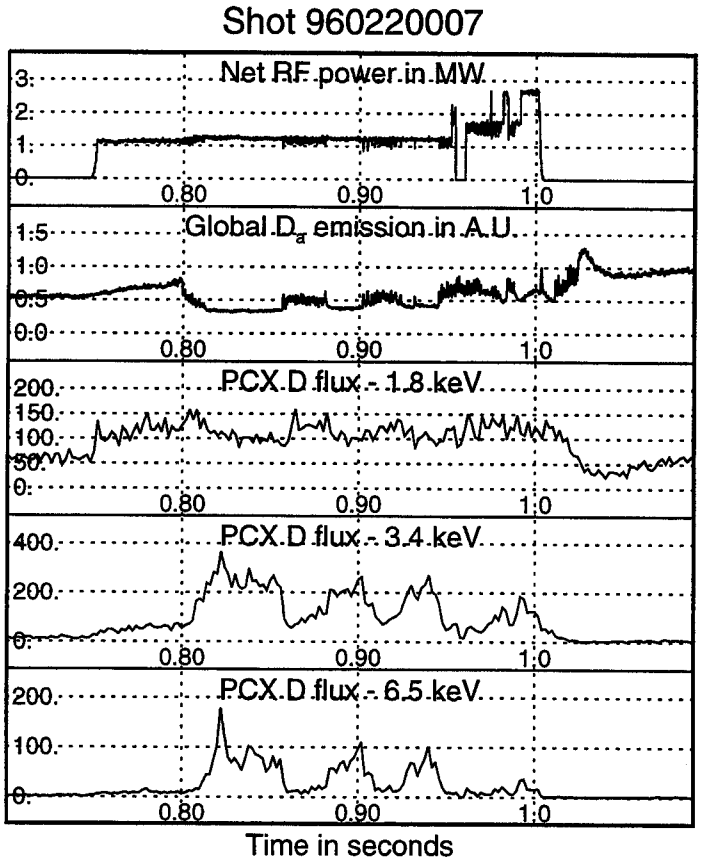

Figure 6.12: Edge heating during ELM-free H-modes

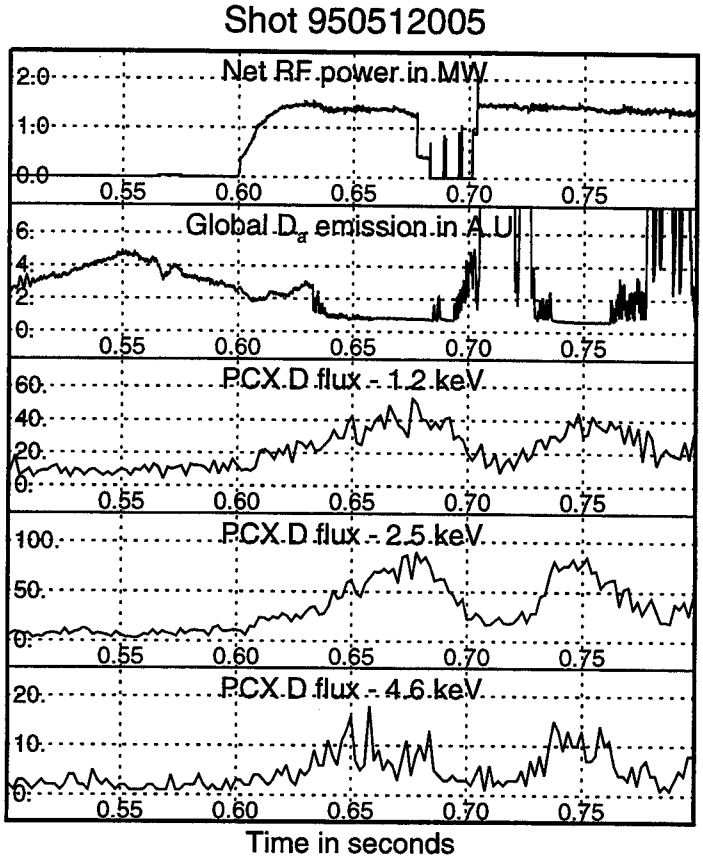

Figure 6.13: Precursor in PCX flux before H-mode

6.8.3 Slow Precursor

Figure 6.13 shows another type of behavior observed during H-modes. In this case, the flux starts to rise after the RF power turns on, and increases on a time scale of 10 ms. It is important to note that the PCX flux does not drop quickly, that is, faster than 1 ms, during the notch in the RF at 0.67 s. This increase in flux is as large as that observed with edge heating, but it changes with a significantly longer time scale. Because the basic plasma parameters are changing on similar time scales, we conclude that is a separate phenomenon from the edge heating discussed in the earlier sections of this chapter.

6.8.4 Conclusions

Forming concrete conclusions is difficult because almost all strong C-Mod H-modes are made using RF power. Differentiating between phenomena that result from H-modes during RF heating and those that involve edge heating affected by the H-mode is not possible on the basis of the data available. However, later we will show that the changes in edge heating with H-mode are consistent with changes in the threshold for parametric decay, which we will argue is the cause of the edge ion heating.

6.9 Power Deposition

Understanding the amount of the RF power that is deposited in the edge is obviously important, for it tells us how much power is not available to heat the plasma center and how much power is immediately reradiated as neutrals from the edge onto the vessel surface.

6.9.1 Methods

It is straightforward to write down an equation for the amount of power in energetic neutrals entering the PCX. If ϵ_i is the counting efficiency for channel i, c_i is the count rate, and $\mathcal{E}_i$ is the energy of particles measured in the channel, then the power in neutrals entering the PCX (in its energy range) is

$$P_{pcx} = \sum c_i \mathcal{E}_i / \epsilon_i. \tag{6.2}$$

We subtract the count rate during an ohmic portion of the plasma to find the counts due to the ion tail in the edge. Since there is no attenuation expected, the power per unit area per unit solid angle leaving the tail in energetic neutrals at a particular

angle is

$$\frac{\partial P_{tail,cx}}{\partial \Omega \partial A} = \frac{1}{A\Omega} \sum c_i \mathcal{E}_i / \epsilon_i. \tag{6.3}$$

The proportion of particles lost from the tail by CX is simply the ratio of the CX time to the total confinement time (τ_{tot}, the characteristic time for loss by all mechanisms). With this, we can estimate the total power loss from the power loss via CX. Thus we find the total power going into the tails is

$$\frac{\partial P_{tail,total}}{\partial \Omega \partial A} = \frac{1}{A\Omega} \sum \frac{c_i \mathcal{E}_i}{\epsilon_i} \frac{\tau_{tot,i}}{\tau_{cx,i}}. \tag{6.4}$$

Of course the confinement times are calculated as a function of energy (see Sec. 4.2).

The problem with this method is its dependence on several factors which cannot be measured directly. In particular the power calculated above is proportional to the term $1/(A\Omega n_0 \epsilon)$, where ϵ is an overall counting efficiency, as long as CX is *not* the dominant loss term.

As described in Chapt. 3, it is straightforward to calculate the flux spectrum from an ohmically-heated plasma given the parameters of a particular discharge. Comparing data from the ohmic phase of a given discharge to this calculation, we generate a scale factor, Θ, which we apply to the data taken during RF heating. Because the neutral density, n_0, in the SOL varies from shot to shot, this scale factor is not a constant. Thus our final equation for the power lost to the edge ions is

$$\frac{\partial P_{loss}}{\partial \Omega \partial A} = \Theta \frac{1}{A\Omega} \sum \frac{c_i \mathcal{E}_i}{\epsilon_i} \frac{\tau_{tot,i}}{\tau_{cx,i}}. \tag{6.5}$$

To reiterate, this gives a calculated value for the power lost to the plasma edge during edge heating which is independent of any errors in the absolute calibration of the PCX or in the estimation of the neutral density in the SOL.

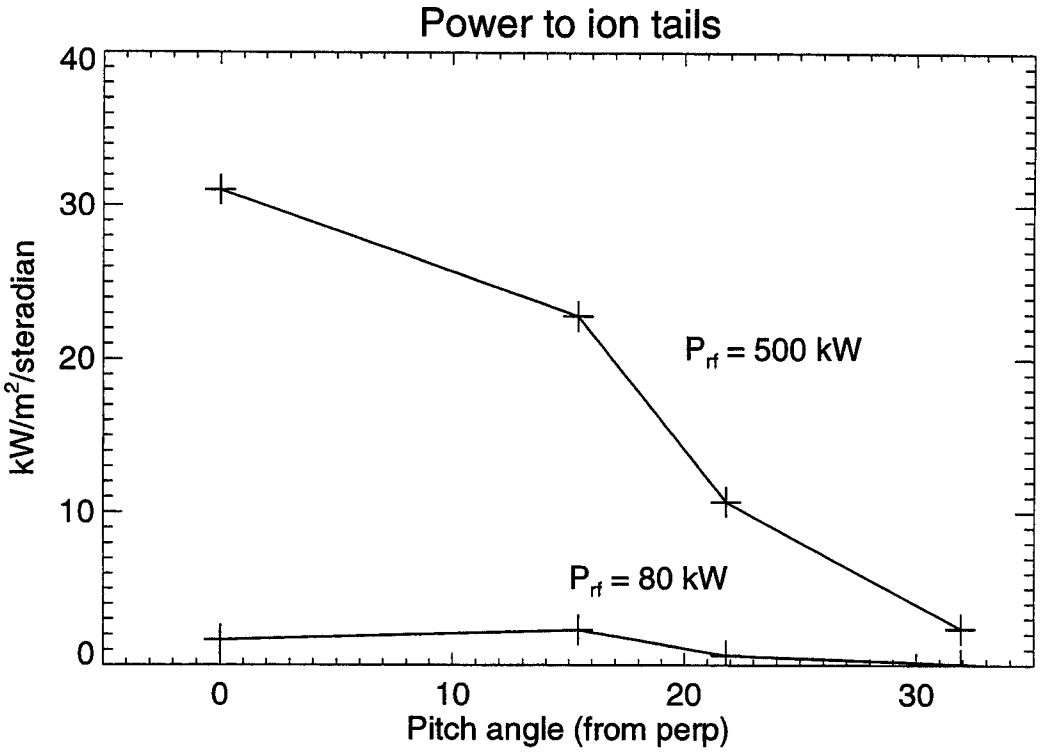

Figure 6.14: Power into edge ion tail as a function of pitch angle

6.9.2 Resonance in Plasma Edge

We have observed that the size of the edge ion tails at low RF power is greatest when the RF is at a cyclotron resonance in the plasma edge. Because of this, we chose this regime to measure the power going into the plasma edge. All other cases, in particular hydrogen minority heating at 5.3 T, show a much lower percentage of RF power being lost to the plasma edge.

In a series of plasmas with $B_0 = 4.7$ T, the PCX was used to measure the power lost from the tails as a function of pitch angle, as shown in Fig. 6.14. A central magnetic field of 4.7 T puts the RF at the third deuterium cyclotron harmonic in the midplane SOL. This figure shows the results at RF power levels of 500 and 80 kW. Assuming the power is negligible at greater pitch angles, which is reasonable considering how fast it falls off, we can integrate over pitch angle to get a total power emitted per square meter. In this example, the power emitted is 10 kW/m^2.

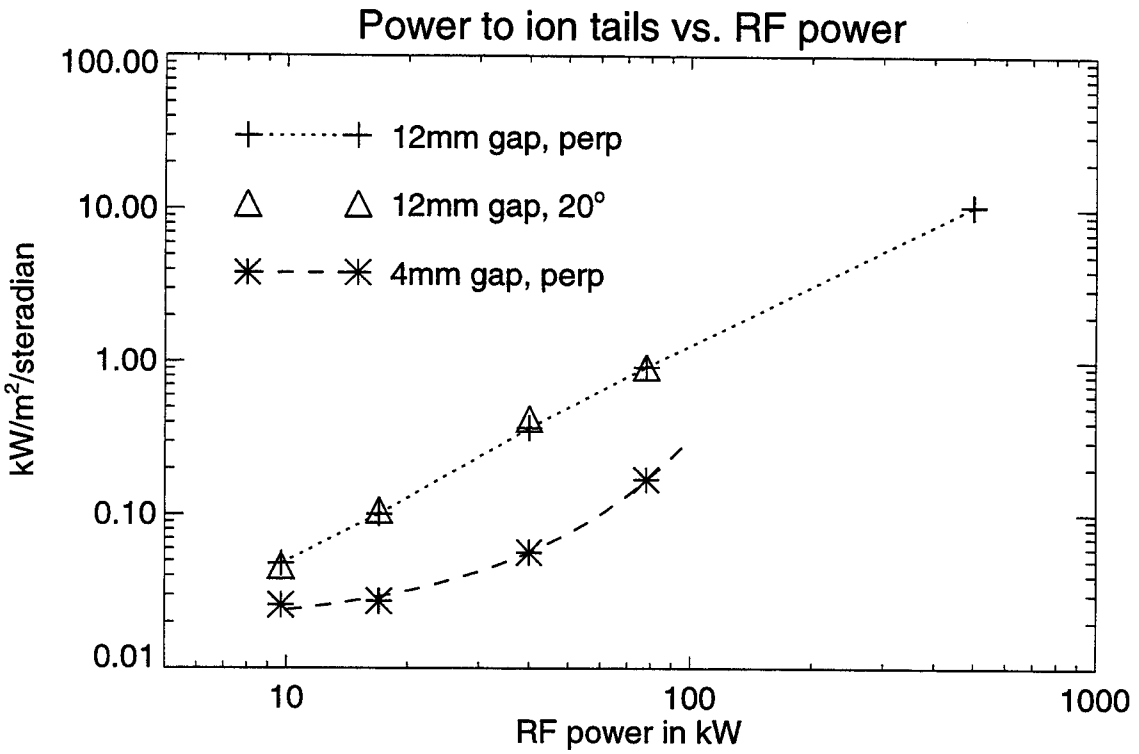

Figure 6.15: Power into edge ion tail as a function of RF power

The total RF power going into edge ions depends on the extent of the edge heating. The narrow range in pitch angle of the emissivity in Fig. 6.14 indicates that the suprathermal ions have bounce tips within 0.2 meters of the midplane. If the accelerated ions only exist near the antenna, say the distance from the PCX to the antenna, then they occupy a toroidal extent of 1.4 meters, versus a total of 5.7 meters if the edge heating is toroidally symmetric. Estimates of the plasma surface area with edge heating are then 0.6 m^2 or 2.3 m^2, respectively. This leads to a total power lost to the edge of 6 kW or 23 kW, that is, 1.2 or 4.6% of the total RF power. Because this shot was chosen as one with large edge heating at low RF power, 4.6% power going to the edge is the worst case. During high power ICRF minority heating on C-Mod, the power lost to the edge via edge ion heating is always less than 1%.

Experiments at $B_0 = 3.5$ T show how power to the edge depends on the RF power. Data from three shots is shown. Two are identical, but with the PCX at

different sight lines. The power going to the edge ions at the given pitch angle varies as $(P_{rf})^{1.4}$. A shot with similar parameters, but with the gap between LCFS and the limiter reduced, shows smaller edge heating, with the power to edge ions varying as $e^{P_{rf}}$. A convective instability with growth rate proportional to RF power would have an amplitude near threshold that varies as $e^{P_{rf}}$.

6.10 Summary

With the neutral particle analyzer, we observe large increases in energetic neutral particle flux during ICRF heating. Because of the fast rise and decay times, the energy dependence of the flux, and the dependence on edge parameters, we identify this flux as being due to energetic ion tails in the plasma scrape-off layer.

Edge ion heating has no detrimental effects on the plasma. Spectroscopic measurements show no increase in radiation correlated with edge heating. The diagnostics of the RF system show that the RF loading does not change due to edge heating. Measuring the particle flux as a function of pitch angle, we calculate that the RF power lost to the edge is always less than a few percent of the total power.

We have identified the dependence of the edge heating on various plasma parameters. During hydrogen minority heating, there is a threshold in RF electric field of about 100 kV/m for edge heating, which changes during H-modes. When the ICRF frequency is at an exact ion cyclotron harmonic in the plasma edge, the edge heating is relatively large at low P_{rf} ($\leq$ 10 kW). These characteristics will be used in our search for the mechanism of the edge heating.

Chapter 7

Mechanisms for Generating Energetic Ions in the Plasma Edge

There exist a large number of processes by which the RF antenna can transmit power to particles in the plasma edge[6][49]. This makes the topic simultaneously difficult and interesting.

This work focuses on ions in the SOL with energies greater than a few keV. A brief survey of the various edge-heating mechanisms will show that our observations are consistent with heating by electrostatic modes.

Several well-known mechanisms of edge heating affect only the electrons. For example, the motion of the electrons in the RF electric field can be randomized by collisions with ions[49]. Also, the RF antenna can couple to global surface modes with large electric fields that damp on electrons[15]. As they only effect electrons, these mechanisms are not relevant to this work.

The paths by which power can be channeled into edge ions can be roughly divided into three categories: direct damping of the electromagnetic wave, kinetic effects, and generation of electrostatic modes.

7.1 Damping of the EM Wave

It is reasonable to ask if the ion tails observed when a harmonic is in the plasma edge result from the fast wave damping on the directly on the ions.

In fact, this damping does not occur at any significant level. By looking at the scaling of fast wave damping with temperature and harmonic number, it will be clear that an accuracy of few orders of magnitude is sufficient.

The damping of the fast wave as a function of harmonic number n is proportional to $(k_\perp \rho)^{2n}/2^n n!$. It is also proportional to the radial width over which damping occurs. Damping occurs when $(\omega - n\omega_{ci})/k_\parallel v_{ti} < 1$, which translates to a radial width of $\delta R = R k_\parallel v_{ti}/n\omega_{ci}$. These scalings lead to a strong temperature dependence for high-harmonic damping.

Including the effect of harmonic number on wave polarization, the damping is[50]

$$\int \mathrm{Im}(k)dx = 2\eta = \frac{2}{\pi}\frac{\omega_{pi}}{c} R \left(\frac{n^2\beta_i}{4}\right)^{n-1} \frac{n-1}{(n-2)!} \tag{7.1}$$

Assuming typical edge parameters, $n_i = 10^{19}\ \mathrm{m}^{-3}$, $T_i = 10$ keV, and harmonic number of 6, the single pass absorption is 2×10^{-24}. The edge ion tails seen at $\omega_{rf} = 6\omega_{cD}$ (as shown in Fig. 6.5) cannot be the result of direct damping of the fast wave launched by the RF antenna.

7.2 Kinetic Effects

Calculations of the ion orbits in the RF fields near the antenna have shown that these can result in increased ion energies in the SOL.

7.2.1 Quiver Motion

Because the quiver velocity of the ions in the RF field is similar to the thermal velocities in the edge, the average energy of the particles is increased[13]:

$$\mathcal{E} = \mathcal{E}_0 + \frac{q^2 E_y^2(\omega_{ci}^2 + \omega^2)}{2m(\omega_{ci}^2 - \omega^2)^2}. \tag{7.2}$$

The electric fields near and between the blades of the Faraday screen on C-Mod are around 400 kV/m at RF power levels where significant edge heating is observed. In this case, the addition to the average ion energy is 6 eV. Quiver motion therefore cannot be the source of the energetic ions observed.

7.2.2 Ponderomotive Force

The antenna RF electric field perpendicular to the magnetic field, particularly the large field between the blades of the Faraday screen, exerts a ponderomotive force on the plasma (see Appendix B),

$$\vec{F}_P = -\frac{q^2}{4m(\omega^2 - \omega_c^2)}\vec{\nabla}|E_\perp|^2. \tag{7.3}$$

This leads to a drift velocity

$$\vec{v} = \frac{\vec{F}_P \times \vec{B}_0}{qB_0^2}. \tag{7.4}$$

The drift moves ions outward in radius, and can cause them to hit the Faraday screen. Assuming an electric field of 450 kV/m (between the blades) changing with a length of 3.4 mm, the ion drift velocity due to the ponderomotive force is approximately 700 m/s. The additional particle energy due to the drift is much less than 1 eV.

Both quiver motion and ponderomotive drift result in higher ion energies in the SOL when the RF is active. The energy difference, though, is only a few eV, and

hence much too small to be the source of the ions observed.

7.3 RF Sheaths

RF sheaths can result in ions with energies in the keV range hitting the vacuum vessel walls and antenna components[51].

RF sheaths are caused by components in the RF electric field parallel to the magnetic field lines on field lines that intersect a material surface. Electrons, much lighter than ions, are accelerated into the surface, causing the DC plasma voltage to increase. The resulting electric field is shielded by the plasma, leaving a sheath of a few Debye lengths at the material. The DC voltage drop across the sheath is similar in magnitude to the RF voltage on the antenna.

This effect could be the source of energetic ions that have been recorded with probes. But as sheaths can only accelerate particles directly into a material surface, they cannot be responsible for the ion tails observed on Alcator C-Mod.

7.4 Electrostatic Modes

The conclusion that electromagnetic waves from the antenna cannot cause the edge ion heating observed in Alcator C-Mod may appear to also apply to electrostatic waves. There are two crucial differences, however. First, nonlinear processes can generate electrostatic modes at lower frequencies, including ω_{ci}, where damping is strong. Second, electrostatic waves can be excited with very large wave numbers compared to the fast wave, which are also more strongly damped.

7.4.1 Parametric Decay Instabilities

The term "parametric decay" refers to a broad class of instabilities brought about by coupling of several modes in a system.

Of interest here is the parametric decay instability by which the RF heating wave decays into an ion Bernstein wave and an ion cyclotron quasimode[8]. The daughter waves are electrostatic in nature, can have large wave number, and one or both has a frequency which is an ion cyclotron harmonic. Parametric decay instabilities are therefore a major candidate for edge ion heating, and will be explored in depth in Chapter 8.

7.4.2 IBW Launching

There are several methods by which a fast wave antenna can excite ion Bernstein waves(IBW)[15].

Measurements taken during IBW launching with a Faraday-shielded toroidal loop antenna on Alcator C[52] and measurements of parasitic IBW excitation by a fast-wave antenna on the ACT-I toroidal device[53] showed significant coupling to low $k_\perp$ waves only. Theoretical predictions[54] also show that only low $k_\perp$ waves are launched by an antenna. The condition of small $k_\perp$ corresponds to a situation where the RF frequency is just below a cyclotron harmonic at the antenna (as shown in Fig. 8.1).

These waves would not damp on an edge plasma, particularly at higher harmonics, because $k_\perp \rho_i \ll 1$. Therefore, they cannot be a direct source of edge ion heating.

7.5 Conclusions

The ICRF can effect all the species in the plasma edge through a variety of mechanisms. They are all potentially important in antenna and tokamak design.

Our observations are consistent with one mechanism of edge ion heating, para-

metric decay instabilities (PDI). In the next chapter, theoretical calculations from PDI theory are made and compared with experimental results.

Chapter 8

Parametric Decay Instabilities

The category of parametric decay instabilities (PDI) can include any system in which a source of free energy and coupling between modes of different frequencies produce oscillations at multiple frequencies that grow with time.

In plasmas heated by an electromagnetic wave, the heating wave can decay into two or more modes at other frequencies. A wide variety of parametric decays are possible, and many have been observed on tokamaks and other machines. Of interest here are plasmas heated with a heating wave near the ion cyclotron frequency.

Parametric decays in the ion cyclotron range were first observed on the linear machine L-4 in 1977[55]. PDI was seen on the ACT-1 torus with fast wave heating[56]. Tokamaks recording observations of PDI during fast wave heating include ASDEX[39], TEXTOR[40], and JT-60[41]. Experiments on DIII-D launching an IBW at a few times the cyclotron frequency also showed PDI[42]. In these experiments, the identification of parametric decay was based on the frequency spectra observed with RF probes.

In our data analysis, particularly in section 6.3.1, we searched for the onset of the edge heating, a more tractable problem than understanding the magnitude of the edge heating. Similarly, finding the point in parameter space where PDI becomes unstable

is more practical than attempting to calculate, for example, nonlinear saturation levels. The threshold for PDI will turn out to be approximately the same as the thresholds observed for edge heating.

8.1 PDI Theory

In order to cause ion tails to appear in the edge, the parametric decay must put power into a mode that can damp on the ions. This limits the kinds of PDI to examine. Once an appropriate PDI type is identified, we must calculate the growth rate to determine if decay of that type is unstable.

8.1.1 Waves

Of interest to us is the parametric decay in which the RF heating field, or "pump wave", decays into an ion Bernstein wave and an ion cyclotron quasimode[8].

This PDI is an example of three-wave coupling, and there are two conservation laws that must hold for the waves involved,

$$\omega_1 + \omega_2 = \omega_0 \quad \text{and} \quad \vec{k}_1 + \vec{k}_2 = \vec{k}_0. \tag{8.1}$$

As we shall show, the wavelength of the decay waves is much shorter than that of the pump wave, basically allowing us to set $\vec{k}_0 = 0$. This is the dipole approximation, and is in fact necessary for the theoretical treatment used. The frequency equation implies that the frequency of the IBW will differ from the RF frequency by a multiple of the cyclotron frequency. At 5.3 T, then $\omega_{IBW} = \omega_{RF} - \omega_{cD} = 1.7\omega_{cD}$. If the RF is at a cyclotron harmonic in the edge, then both the quasimode and the IBW will be near a cyclotron harmonic.

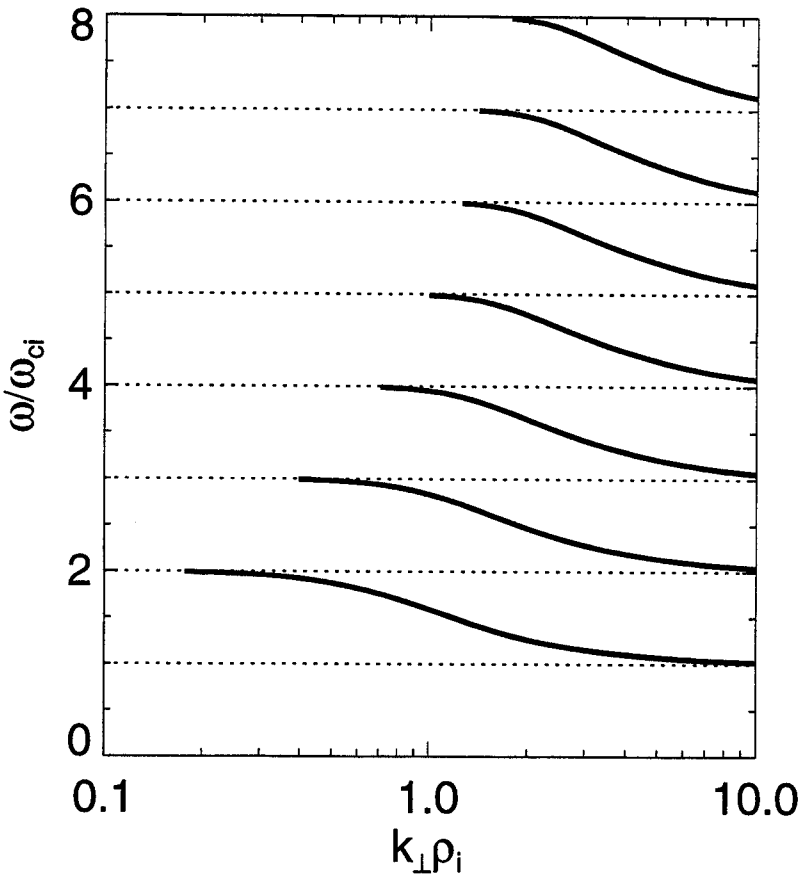

Figure 8.1: Typical dispersion relation for ion Bernstein wave, assuming $n = 1 \times 10^{19}$ m^{-3}, $T = 10$ eV, $k_{||} = 40$ m^{-1}, $B = 4$ T.

In principle, ion Bernstein waves propagate with $k_{||} = 0$ or any $k_{||}$ satisfying[57]

$$\frac{\omega}{k_{||} v_{te}} \gtrsim 3.$$

The ion Bernstein waves involved in the parametric decay process, however, have $k_{||} \neq 0$. Figure 8.1 illustrates a typical dispersion relation for ion Bernstein waves.

The ion cyclotron quasimode is not a propagating wave. It occurs near multiples of ω_{ci} at any $\vec{k}$. Unlike propagating waves, the ion fluid current is in phase with the electric field, so the power deposited, $P = \langle \vec{E} \cdot \vec{j} \rangle$, is large.

8.1.2 Dispersion Relation

The derivation followed assumes that the plasma is infinite and uniform, and the pump wave is treated in the dipole approximation. Collisions are neglected, as is the magnetic component to the RF field.

An external electric field, $\vec{E} = (E_{0\perp}\hat{x} + E_{0\|}\hat{z})\cos\omega_0 t$, imposed upon a plasma in a uniform static magnetic field $B\hat{z}$, will induce fluid motion

$$\vec{v} = \frac{q}{m}\left[\frac{E_{0\perp}\omega_0}{\omega_0^2 - \omega_c^2}(\cos\omega_0 t\hat{x} + \frac{\omega_c}{\omega_0}\sin\omega_0 t\hat{y}) + \frac{E_{0\|}}{\omega_0}\cos\omega_0 t\hat{z}\right] \tag{8.2}$$

where $\omega_c = qB/m$ for the species under question.

Using this to define an oscillating frame of reference, a modified linearized Vlasov equation can be written for each species σ[58]:

$$\frac{\partial F_\sigma}{\partial t} + \vec{v}\cdot\vec{\nabla}_x F_\sigma + (\vec{v}\times\vec{\omega}_{c\sigma})\cdot\vec{\nabla}_v F_\sigma = -\frac{q_\sigma}{m_\sigma}\vec{E}_k^{(1)}\cdot(\vec{\nabla}_v f_{0\sigma})e^{i\mu_\sigma\sin\omega_0 t}. \tag{8.3}$$

In this equation, F and $E_k^{(1)}$ refer to perturbed quantities, while f_0 refers to the unperturbed distribution function. Thus, this equation describes the propagation of a wave through a plasma *already* disturbed by an external wave at ω_0. The time-varying term on the right hand side, $\mu\sin\omega_0 t$, couples waves with frequencies separated by ω_0. This is the coupling between the ion quasimode and the IBW. The coupling term μ_σ is defined as

$$\mu_\sigma = \frac{q_\sigma}{m_\sigma}\left[\left(\frac{\vec{E}_\perp\cdot\vec{k}_\perp}{\omega_0^2 - \omega_{c\sigma}^2} + \frac{E_{\|}k_{\|}}{\omega_0^2}\right)^2 + \frac{|\vec{E}_\perp\times\vec{k}_\perp|^2\omega_{c\sigma}^2}{(\omega_0^2-\omega_{c\sigma}^2)^2\omega_0^2}\right]^{1/2} \tag{8.4}$$

where σ is simply an index representing electrons or one of the ion species present.

To proceed, it is assumed that $\mu \ll 1$. Physically, this means that the displacement of a particle during an RF cycle is shorter than the wavelength of the decay wave.

This approximation is not necessary, but greatly simplifies the presentation of the equations.

Solving the modified Vlasov equation (Eq. 8.3) with Maxwell's equations gives[8]

$$\epsilon(\omega_1)\epsilon(\omega_2) = -\frac{1}{8}\sum_{\sigma,\nu} |\mu_\sigma - \mu_\nu|^2[\chi_\sigma(\omega_1) - \chi_\sigma(\omega_2)][(\chi_\nu(\omega_1) - \chi_\nu(\omega_2))]. \tag{8.5}$$

The sums over ν and σ are over species in the plasma. The χ's are defined as the standard plasma susceptibilities, and other variables are defined in the customary way; namely

$$\chi_\sigma = \frac{1}{k^2\lambda_{D\sigma}^2}\sum_{n=-\infty}^{\infty} \Gamma_n(b_\sigma)(1 + \zeta_{\sigma 0} Z(\zeta_{\sigma n})). \tag{8.6}$$

$$b_\sigma = \frac{k_\perp^2 v_{t\sigma}}{2\omega_{c\sigma}} \qquad \zeta_{\sigma n} = \frac{\omega - n\omega_{c\sigma}}{k_\parallel v_{t\sigma}} \qquad v_{t\sigma}^2 = 2T_\sigma/m_\sigma$$

$$\epsilon(\omega) = 1 + \sum_\sigma \chi_\sigma(\omega)$$

As described in Eq. 8.1, $\vec{k}_1 = -\vec{k}_2$, so references to $\vec{k}$ in the above equations are suppressed. The function Z is the Fried-Conte plasma dispersion function, and $\Gamma_n(b) = I_n(b)e^{-b}$ with I_n being the modified Bessel function. The Debye length of species σ is $\lambda_{D\sigma}$.

The relative velocity between different species, which appears in the term $|\mu_\sigma - \mu_\nu|$, is the source of free energy that drives the instabilities.

Equation 8.5 has real and imaginary parts, and its complex solutions ω_1, ω_2 give the growth rates of the instabilities.

8.1.3 Growth rate

In Eq. 8.5, we have on the left hand side the product of two susceptibilities, and on the right, a term which we are formally considering as "small". So we look for a solution in which $\epsilon(\vec{k}, \omega_2) \simeq 0$ in order that the equation be satisfied.

Assuming the growth rate is much smaller than the frequency, we can make the approximation

$$\epsilon(\omega_2) = \epsilon(\omega_R + i\gamma) \simeq \epsilon(\omega_R) + i\gamma \frac{\partial \epsilon}{\partial \omega} \simeq \epsilon_R(\omega_R) + \epsilon_I(\omega_R) + i\gamma \frac{\partial \epsilon_R}{\partial \omega} \tag{8.7}$$

The subscripts R, I refer to the real and imaginary parts.

For simplicity of notation, we now assume that only electrons and one ion species are considered. The real and imaginary parts of Eq. 8.5 are then

$$\epsilon_R(\omega_R) \simeq \frac{1}{4}|\mu_i - \mu_e|^2 \,\mathrm{Re}\left[\frac{1}{\epsilon(\omega_1)}(\chi_i(\omega_1) - \chi_i(\omega_R))(\chi_e(\omega_1) - \chi_e(\omega_R))\right] \tag{8.8}$$

$$\epsilon_I + \gamma \frac{\partial \epsilon_R(\omega_R)}{\partial \omega} \simeq \frac{1}{4}|\mu_i - \mu_e|^2 \,\mathrm{Im}\left[\frac{1}{\epsilon(\omega_1)}(\chi_i(\omega_1) - \chi_i(\omega_R))(\chi_e(\omega_1) - \chi_e(\omega_R))\right]. \tag{8.9}$$

We solve for the growth rate

$$\gamma \simeq \frac{-\epsilon_I}{\frac{\partial \epsilon_R}{\partial \omega}} + \frac{|\mu_i - \mu_e|^2}{4\frac{\partial \epsilon_R}{\partial \omega}} \,\mathrm{Im}\left[\frac{1}{\epsilon(\omega_1)}(\chi_i(\omega_1) - \chi_i(\omega_R))(\chi_e(\omega_1) - \chi_e(\omega_R))\right]. \tag{8.10}$$

The solution to $\epsilon_R(\omega_R) \simeq 0$ describes the ion Bernstein wave. So in Eq. 8.10, $-\epsilon_I / \frac{\partial \epsilon_R}{\partial \omega}$ describes the normal damping of the IBW. The term proportional to μ^2 is the PDI driving term. It must be larger than the IBW damping term for the decay modes to grow.

If $(\vec{k},\omega_1)$ do not describe a propagating wave then the imaginary part of the term in the brackets will generally be "small", because $\epsilon(\omega_1)$ is real and "large" over most of its range. If $\omega_1 = \ell\omega_{ci}$, however, $\chi_i(\omega_1)$ is large and imaginary. This corresponds to the ion cyclotron quasimode described above. At this frequency, then, we have

$$\frac{(\chi_i(\omega_1) - \chi_i(\omega_R))}{\epsilon(\omega_1)} \simeq \frac{\chi_i(\omega_1)}{\chi_i(\omega_1)} = 1. \tag{8.11}$$

This leaves us with an expression for the growth rate of

$$\gamma \simeq \frac{-\epsilon_I}{\frac{\partial\epsilon_R}{\partial\omega}} + \frac{|\mu_i - \mu_e|^2}{4\frac{\partial\epsilon_R}{\partial\omega}} \mathrm{Im}(\chi_e(\omega_1) - \chi_e(\omega_R)). \tag{8.12}$$

The condition on χ_i leading to Eq. 8.11 is not always met, and we will keep the more general expression when necessary in calculations.

8.1.4 Convection

If the IBW frequency is higher than the ion quasimode frequency, then there is always a value for $k_{||}$ such that the growth rate given in Eq. 8.12 is positive. However, the growth rate may be so small that the instability will not grow significantly on relevant time scales.

A spectral component of the random noise spectrum of, say, density, characterized by $\vec{k}$ in an RF field will grow in time as described in Eq. 8.10. At the same time, it will move in space with the direction and speed of the ion Bernstein wave group velocity. Because the RF field has a finite extent, the perturbation may propagate out of the volume of interaction before it grows significantly.

If the spatial extent of the RF field along the group velocity, $\vec{v}_g$, is L, then the time in the interaction volume is $\tau = L/v_g$. If $\tau\gamma \ll 1$, then the wave is not unstable in a convective sense. Traditionally, the threshold is taken to be at $\tau\gamma = \pi$. If the interaction region has dimensions (L_x,L_y,L_z), then the time a perturbation remains

in the interaction region is

$$\tau \simeq \min\left(\frac{L_x}{\vec{v}_g \cdot \hat{x}}, \frac{L_y}{\vec{v}_g \cdot \hat{y}}, \frac{L_z}{\vec{v}_g \cdot \hat{z}}\right).$$

In all calculations, these three terms were examined to find the proper interaction time. For simplicity of notation, we will refer to the right-hand side above as L/v_g.

The term $\gamma L/v_g$ will be referred to here as the "PDI growth". The amplitude of the decay wave, recall, is proportional to $e^{\gamma L/v_g}$.

The appropriate interaction volume to use must be entirely in the antenna near field and have only small variation in parameters, including magnetic field. Because of toroidal symmetry, the length in that direction is constrained only to be with in the antenna near field, giving a length of about 0.5 m.

Radially, the dimension used is 10 mm. The LCFS of the plasma is 20-25 mm from the front of the Faraday screen. Density is approximately constant outside 6 mm from the LCFS, but electron temperature changes with a length scale of about 10 mm[10], so 10 mm is used as the radial width. The R dependence of B_0 also constrains the radial width. Looking ahead and using values for $k_{||}$ and T_i at which there is instability, and using a width in frequency for a resonance of

$$\delta\omega = k_{||} v_{ti},$$

we find a radial width of 10-20 mm.

In the poloidal direction, the constraint is due to the curvature of the flux surfaces and the limiters. A distance of 0.04 m above or below the midplane moves a flux surface into a different magnetic field, as defined above.

Away from the midplane, the height of the interaction region would be $\frac{B_Z}{B_R}0.01$ m.

With an equation for the convective growth rate, it is possible to calculate the threshold for instability as a function of various parameters in the range of interest

for C-Mod.

8.2 Numerical Calculations

In Chapt. 6, it was noted that having the RF at a cyclotron harmonic in the plasma edge changes the edge heating dramatically. Parametric decay occurring during hydrogen minority heating would have an IBW frequency of $1.7\omega_{ci}$, while PDI with a resonance in the edge would generate an IBW at a frequency near $\ell\omega_{ci}$. Because the propagation of the IBW is very different in these two regimes, we treat them separately.

All numerical calculations were done after separating the real and imaginary parts of the equations as described above. All dispersion relations were solved for arbitrary $\vec{k}$. Terms of the order ω/ω_{ce} were neglected.

8.2.1 PDI during Hydrogen Minority Heating

Parameters and equations

During hydrogen minority heating, the RF frequency is at $2.7\omega_{ci}$ in the plasma edge at the outboard midplane. Because the IBW frequency is not near a cyclotron harmonic, the equation for the growth rate is simplified using

$$\mathrm{Im}\,\epsilon(\omega_R) \simeq \mathrm{Im}\,\chi_e(\omega_R) = \frac{\sqrt{\pi}}{k^2\lambda_{De}^2}\zeta e^{-\zeta^2} \tag{8.13}$$

$$\text{where} \qquad \zeta = \frac{\omega_R}{k_\parallel v_{te}}.$$

We will soon consider the more general case, but if we assume that the quasimode is exactly at ω_{ci}, then

$$\frac{1}{1.7}\zeta_{IBW} = \zeta_{QM} \equiv \zeta.$$

Recall that $\vec{k}$ is the same for both modes. With this, we obtain a simple representation for the growth rate,

$$\gamma = \frac{1}{\frac{\partial \epsilon_r}{\partial \omega}} \frac{\sqrt{\pi}\zeta}{k^2 \lambda_{De}^2} \left(\frac{\mu^2}{4} e^{-\zeta^2} - \left(1.7 + \frac{\mu^2}{4} \right) e^{-(1.7\zeta)^2} \right). \tag{8.14}$$

At large ζ, $e^{-\zeta^2} \gg e^{-(1.7\zeta)^2}$, meaning we can always choose a large enough ζ to make the growth rate positive. At very large ζ, however, the growth rate will be positive but very small, and the IBW will not be unstable in a convective sense. In practice, convective instability is only found when $1 < \zeta < 3$.

As described in section 2.2.3, the largest component in the antenna electric field is parallel to the current strap, E_θ. For the decay modes,

$$\vec{k}_\perp \parallel \hat{\theta} \quad \text{implies} \quad |\mu_i - \mu_e| \simeq \frac{e}{m_i} \frac{E_\theta k_\perp}{\omega_{ci}^2 - \omega_0^2}$$

while

$$\vec{k}_\perp \parallel \hat{r} \quad \text{implies} \quad |\mu_i - \mu_e| \simeq \frac{e}{m_i} \frac{E_\theta k_\perp}{\omega_0 \omega_{ci}}.$$

Thus μ is larger if $\vec{k}_\perp \parallel \hat{r}$. Because the interaction region has different extent in the r and θ directions, we must always check both directions when searching for a convectively unstable mode.

The Recipe

The method for applying these equations is comparatively straightforward. Plasma parameters for the region of interest are chosen. For each $k_\parallel$, the IBW dispersion relation is solved to find $k_\perp$, and this is used to find $\vec{v}_g$ for the wave and μ. The convective growth rate is then calculated for a range of $k_\parallel$ to find the maximum. We need only find a single $k_\parallel$ that has $\gamma\tau > \pi$ to show that parametric decay is unstable.

We vary the antenna electric field E_θ, recalculating the maximum growth rate, to

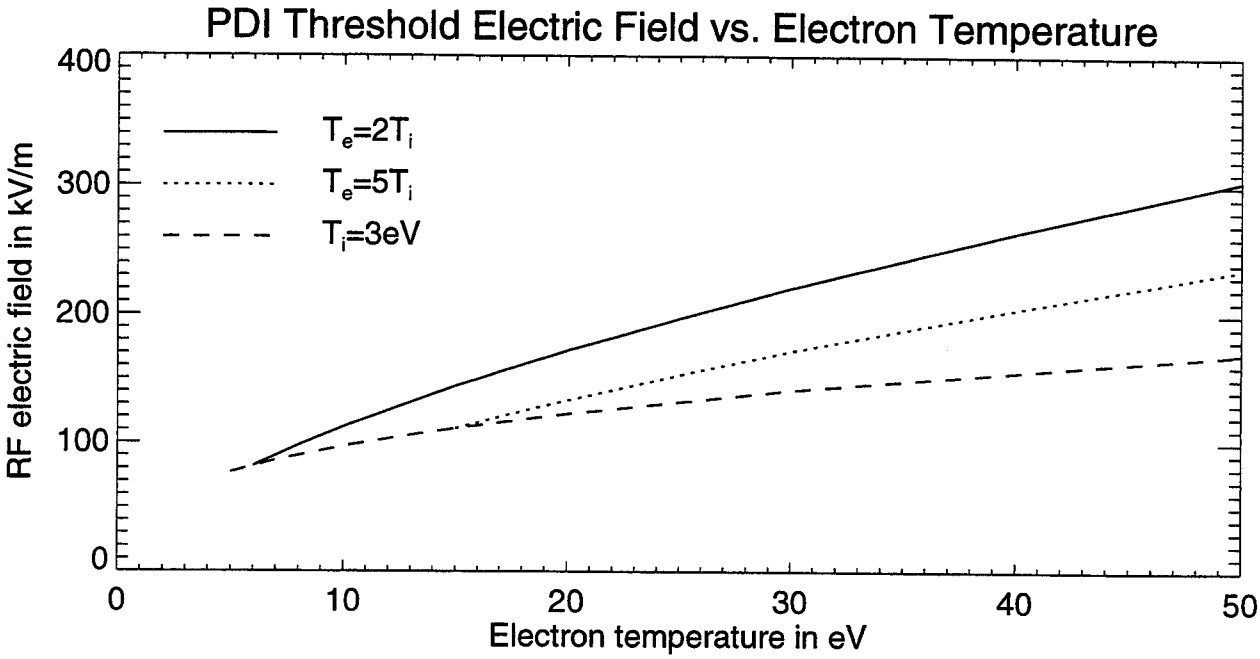

Figure 8.2: RF electric field PDI threshold as a function of plasma temperature

find a threshold for PDI.

When the restriction that the quasimode occurs exactly at ω_{ci} is relaxed, the procedure is the same as above, except there is an extra free parameter.

Results

Through the calculations, we found a threshold electric field as a function of density, and ion and electron temperature.

Figure 8.2 shows the threshold in RF electric field as a function of plasma temperature. The density used is 1×10^{19} m^{-3}. Most of this temperature dependence is in the IBW group velocity, and not in the growth rate γ.

The most striking result is that the threshold for PDI in SOL type parameters is very close to the experimentally observed threshold for edge ion heating. In the outer SOL, where a temperature of a few eV is expected, the threshold is on the order of 100 kV/m (we will refine these parameters below), the same as the electric field in the antenna near field at power levels around 0.5 MW.

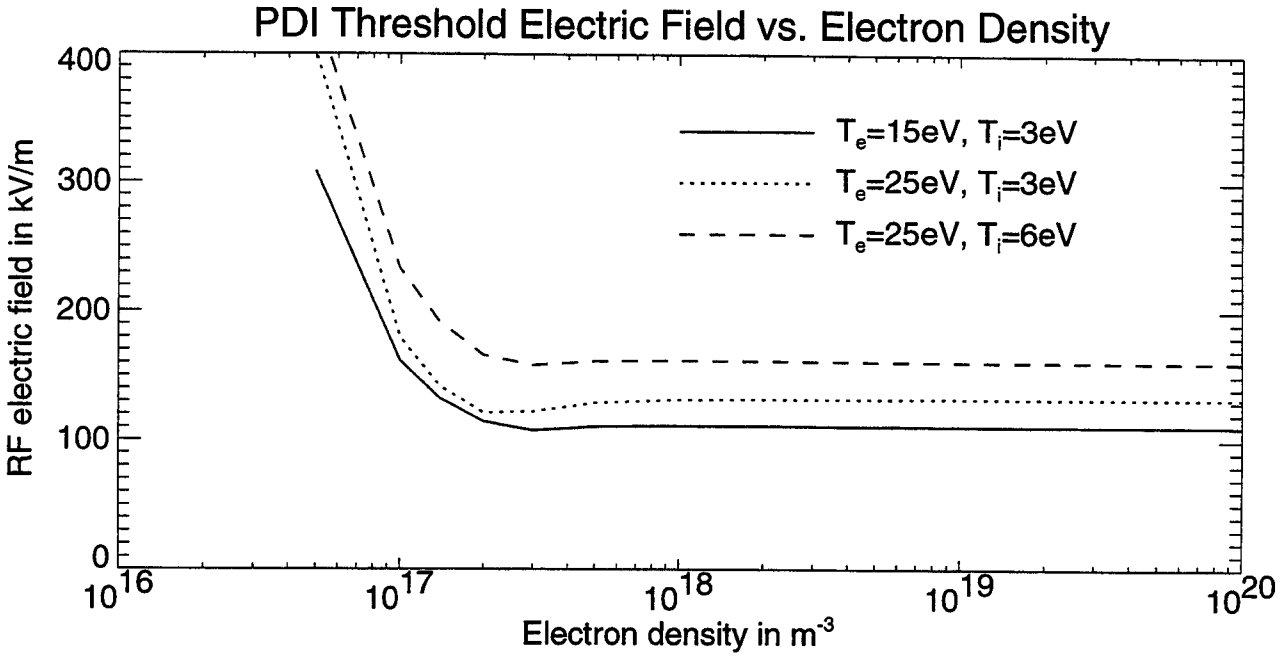

Figure 8.3: RF electric field at PDI threshold vs. plasma density.

On the other hand, at temperatures near or inside the LCFS, 50 eV or so, the threshold is much higher than any expected RF electric field.

Figure 8.3 demonstrates the effect of plasma density on the threshold. The temperature is fixed for both ions and electrons as shown. The threshold is independent of density for densities above 3×10^{17} m^{-3}. In L-mode discharges on Alcator, the outer part of the scrape-off layer maintains a density greater than 1×10^{18} m^{-3}[47].

So far in this section, it was assumed that the quasimode is at the ion cyclotron frequency, because this is what will generate the fast ion tails. We must actually consider the quasimode frequency as a free parameter.

Figure 8.4 shows several plots of convective growth as a function of quasimode frequency for several values of T_e. These calculations assume $E_0 = 120$ kV/m, $T_i = 3$ eV, $n_e = 10^{19}$ m^{-3}. At very low T_e, the convective growth is large, but is peaked at $\omega_{QM} = 0.92\omega_{ci}$. In this case, the quasimode would grow at this frequency, and there would not be any ion heating. At higher T_e, the growth is lower, though still high enough for the mode to be unstable, and the peak is at $\omega_{QM} = \omega_{ci}$. As T_e

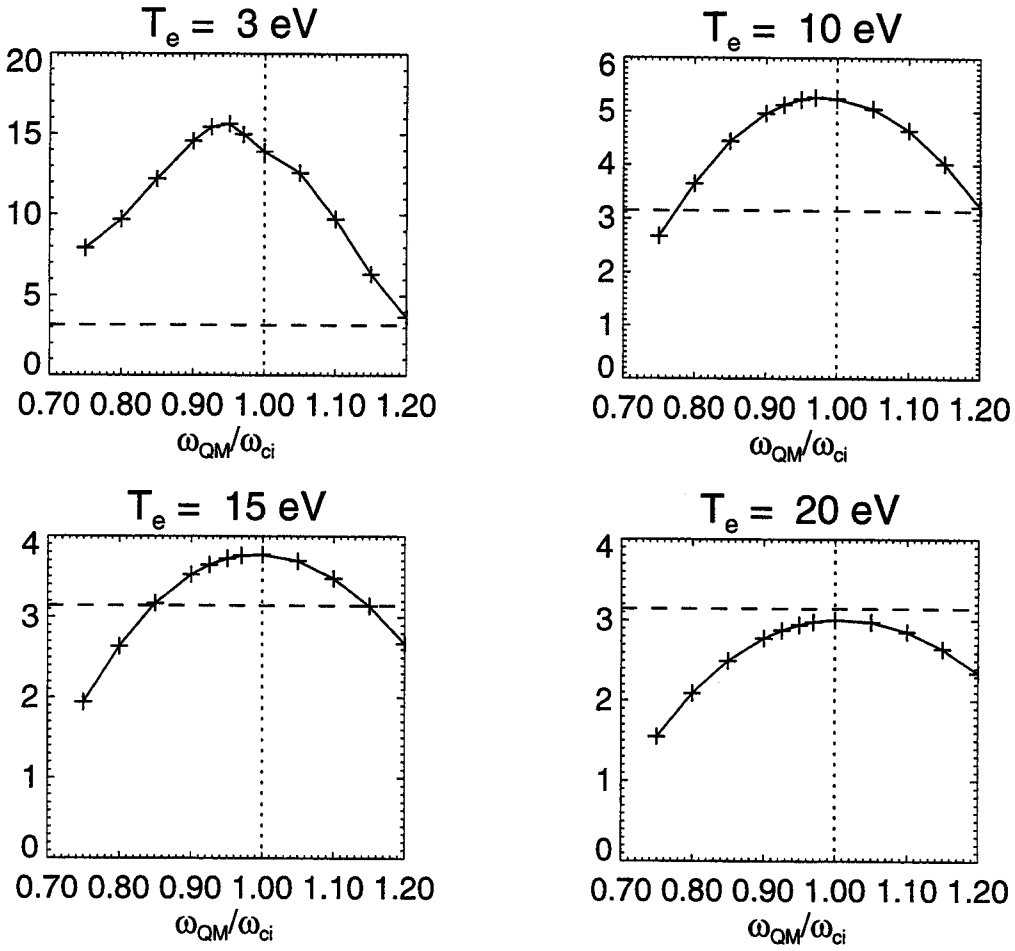

Figure 8.4: PDI growth, $\gamma L/v_g$, as a function of quasimode frequency for $T_e = 5$, 10, 15, 20 eV. Threshold value, $\gamma L/v_g = \pi$ is shown as a dashed line.

increases, the growth decreases, and the peak stays at the cyclotron frequency. So at $n = 1 \times 10^{19}$ m^{-3}, $T_i = 3$ eV, $E_0 = 120$ keV, PDI *with* edge ion heating only occurs for a range of T_e, approximately between 12 and 18 eV.

In section 8.1.3 it was argued qualitatively that the highest growth rate should occur when the quasimode is near the cyclotron frequency. In the calculation above, we found that the highest growth rate can occur with the quasimode significantly below the cyclotron frequency at certain electron temperatures. The reason for this shift is the strong dependence of the growth rate on the difference between the quasimode and IBW frequencies.

H-modes

As described in section 6.2.3, the edge ion tails change sharply at H-mode transitions. In the example shown in Fig. 6.3, we do not observe edge heating when the RF turns on, but edge heating starts when the plasma transitions into an ELM-free H-mode. The edge heating is large when the plasma is in ELM-free H-mode, and small in ELMy H-mode or L-mode.

This effect can be explained by the PDI calculations above. During ELM-free H-mode, energy transport through the LCFS is lower and the electron temperature in the outer SOL is lower[47][45]. The low temperature reduces the PDI threshold. With the onset of ELMs, energy transport to the SOL is increased and the electron temperature rises quickly. This increase raises the electric field threshold, causing the PDI and edge heating to stop.

8.2.2 Resonance in Plasma Edge

Parameters

If we examine a plasma in which the toroidal field value puts the RF at a cyclotron harmonic in the plasma edge, the situation becomes more complicated. In the previ-

ous section, we found that the results of the calculations did not depend strongly on magnetic field. In an IBW with $\omega_{IBW} \sim \ell\omega_{ci}$, $\vec{k}_\perp$ is a strong function of ω_{IBW}, and the wave has $k_\perp\rho_i \ll 1$ just below a harmonic and $k_\perp\rho_i \gg 1$ just above a harmonic[57]. Also, if one of the modes involved in the decay is near an even harmonic of the deuterium cyclotron frequency, then it is also near a hydrogen cyclotron frequency, making it necessary to include the effect that the 0.5-15% of hydrogen in the edge will have on the IBW propagation and damping. The equation for the growth rate, Eq. 8.10, must then be expanded to include three species in the plasma. Terms proportional to any of $|\mu_D - \mu_e|$, $|\mu_H - \mu_e|$, $|\mu_D - \mu_H|$ may be the primary driving terms for the instability.

Growth Rate

We find that the calculated threshold for parametric decay is very low in this situation, and the dominant coupling term is $|\mu_D - \mu_H|$.

It is possible to see this qualitatively. We choose, as an example, a toroidal field such that $\omega_{RF} \gtrsim 4\omega_{cD}$ in the edge. The dominant decay is into a quasimode at $2\omega_{cD}$ and an IBW with $\omega_{IBW} \gtrsim 2\omega_{cD}$. Because the IBW is near the cyclotron harmonic, $k_\perp$ is very large. Hence, μ is of order one, even when the mismatch in the hydrogen and deuterium quiver velocities is small. Furthermore, when $k_\parallel$ is small, the IBW is essentially undamped. Also, the group velocity of the IBW is much lower near a harmonic. So the coupling is large, the wave is undamped, and the time for perturbations to transit the pump region is comparatively long. All these factors contribute to the growth rate.

Results

Figure 8.5 shows the results of a calculation of the PDI growth, $\gamma L/v_g$, versus magnetic field, simulating a B_0 ramp. Convective growth is shown for two decays:

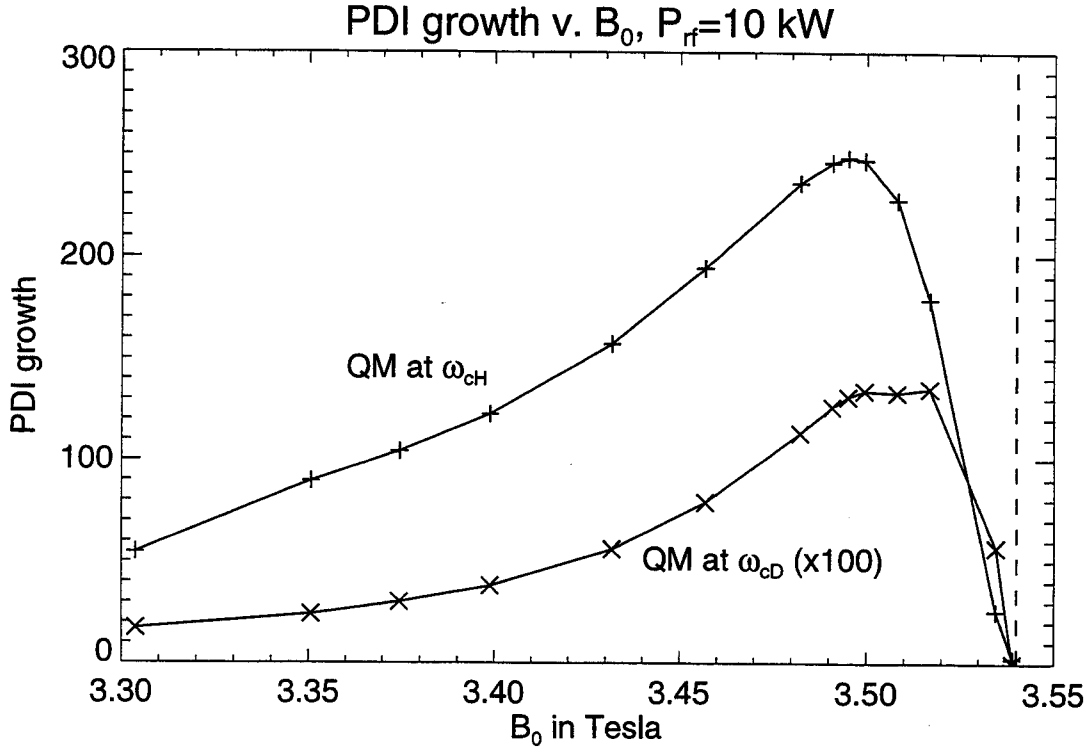

Figure 8.5: PDI Growth, $\gamma L/v_g$, vs. magnetic field. $4\omega_{cD}$ in plasma edge when $B_0 = 3.54$ T.

$\omega_{QM} = \omega_{cD}$, $\omega_{IBW} \simeq 3\omega_{cD}$; and $\omega_{QM} = 2\omega_{cD}$, $\omega_{IBW} \simeq 2\omega_{cD}$. The peak of the higher curve, at approximately 250, is much larger than the threshold value of π. The RF electric field used, 10 kV/m, corresponds to an RF power level approximately 10 kW. At the parameters used, the lower curve is actually not convectively unstable, but would be at 20 kW of RF power.

A few caveats must be applied. First, the growth rate is unbounded as $k_{\|} \to 0$, so the calculated growth is sensitive to the lower cutoff on $k_{\|}$. We assumed that the $k_{\|}$ of both decay modes must be greater than the $k_{\|}$ of the launched fast wave. Second, inclusion of a collision term would result in some damping of the IBW, reducing the growth. Finally, because the IBW group velocity is relatively slow near a harmonic, the transit time for a perturbation through the pump region is, in this example, 0.4 ms, which is slower than times for changes in the edge (in comparison, the transit time calculated for $B_0 = 5.3$ T in the previous section is 1.5 μs). A more complete calculation including all these factors must delve deeply into the physics of the plasma edge, and is beyond the scope of the present work.

Nevertheless, given that the growth is a factor of 100 over the threshold at an RF power of 10 kW, we expect that the parametric decay as described will occur.

Odd versus Even Harmonics

As shown in the traces in Fig. 6.5, hydrogen flux is high when the RF is at an even cyclotron harmonic, and deuterium is large at odd harmonics.

This supports the conclusion that parametric decay is occurring due to the coupling term proportional to $|\mu_D - \mu_H|$. For example, at $\omega_{RF} \gtrsim 4\omega_{cD}$ as above, PDI can occur through electron-deuterium coupling into a deuterium cyclotron quasimode and an IBW near $3\omega_{cD}$, and would heat deuterium only. This turns out to be barely unstable according to the calculation when $P_{rf} \sim 10$ kW. But as we have just shown, PDI with the quasimode at a hydrogen cyclotron frequency and an IBW near $2\omega_{cD}$,

which will also damp on hydrogen, has a growth two orders of magnitude higher.

These large growth rates occur when the quasimode is at $\ell\omega_{cH}$. At even deuterium harmonics, then, both of the decay modes will be at hydrogen harmonics, and absorption on hydrogen dominates. At odd harmonics, the IBW will be at an odd deuterium harmonic, and deuterium damping will be large. This is consistent with the observations made with different harmonics in the plasma edge.

This argument that the behavior at different harmonics can be described by changes in the growth rate must remain qualitative for two reasons: the saturation level of the instability is not known, and the relative damping on hydrogen versus deuterium has not been calculated. So far, we have assumed that the instability will grow at least to the point where it has a measurable effect on the ions in the plasma edge before its growth is stopped by some non-linear effect (Eq. 8.10 is valid only in the limit that the amplitudes of the unstable waves is small). This saturation level has not been calculated.

In general, it is well-known how to calculate the damping of a wave on different ion species[30]. For electrostatic modes, such as the ion cyclotron quasimode and the ion Bernstein wave, the ratio of damping on hydrogen to damping on deuterium is the ratio of the imaginary parts of the linear susceptibilities (defined in Eq. 8.6), χ_H, and χ_D. However, in calculating the damping in a parametric decay instability, currents and electric fields must be calculated from Eq. 8.3, which includes the coupling of the external RF wave to the decay waves.

8.3 RF Probes

The waves involved in parametric decay instabilities can be observed directly using RF probes. Although other experiments have reported correlations between PDI spectra and fast particles in the edge[42][41][43][44], there is no reason to expect a

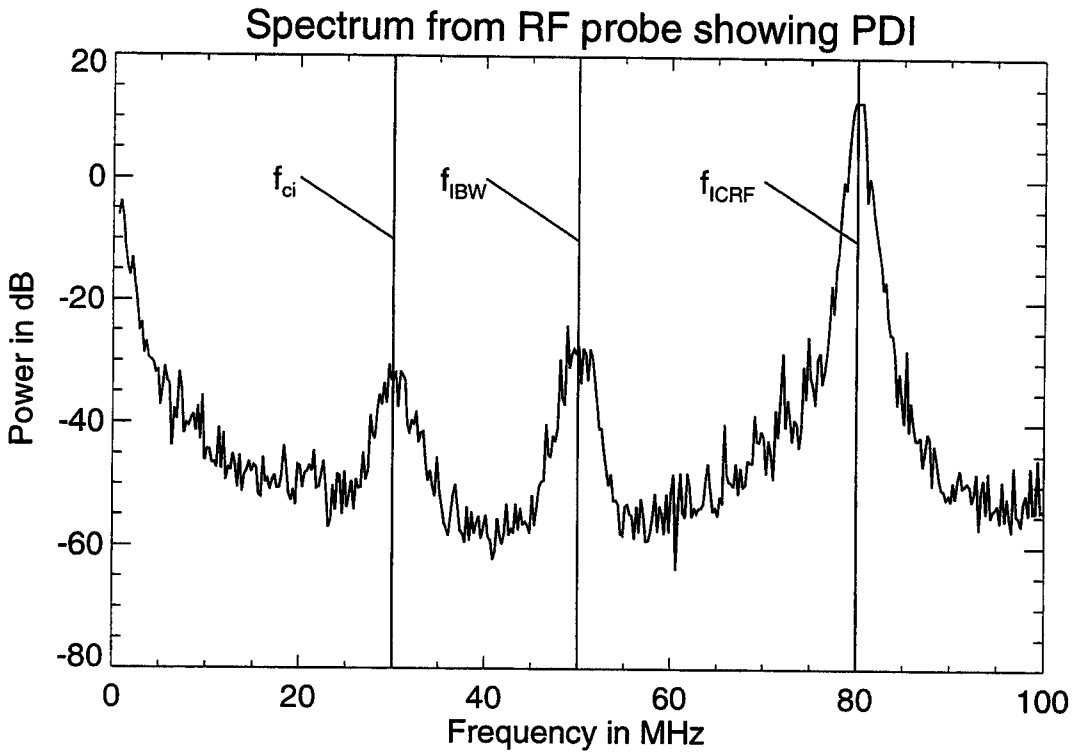

Figure 8.6: RF spectrum from RF probe, showing a spectrum typical of PDI. B_0 is 5.3 T, and the deuterium cyclotron frequency is 30 MHz at the probe position.

strong correspondence between PDI-generated fast ions and PDI spectra detected by the RF probes on Alcator C-Mod.

In some circumstances, RF probes on C-Mod have recorded spectra typical of PDI, particularly at values of B_0 that place a cyclotron resonance at the probe tip.

Figure 8.6 shows a spectrum taken at a central B_0 of 5.3 T. The large peak at 80 MHz is due to the fast wave launched by the RF antennas. Interpreting the other peaks as the results of PDI, we identify the peak near 30 MHz as an ion cyclotron quasimode at the deuterium cyclotron frequency, and the peak at 50 MHz as an IBW.

8.3.1 Correspondence with PCX Measurements

Measurements from the RF probes, PCX edge heating measurements, and the theory of PDI indicate that PDI measurements by the RF probes should be independent of

edge ion heating observed by the PCX.

The RF probes are positioned at different radii, and some can be scanned in radius. A critical observation is that the quasimode peaks are at the frequency of the cyclotron frequency *at the probe tip*, rather than the cyclotron frequency at, say, the midplane LCFS[59]. It therefore appears that the oscillations measured with the RF probes occur at the probes themselves. They are not waves generated elsewhere that have propagated to the probes.

During hydrogen minority heating, the parametric decay has a threshold in electric field at a value we expect only in the near field of the antennas, that is, within a few centimeters. Therefore, the quasimode, which only exists in the pump region, would only be measurable by a probe which is actually in the antenna near field and at the correct radial location. The RF probes that provided the spectra shown above are more than a meter away from the antenna.

The ion Bernstein wave should propagate out of the pump region. During hydrogen minority heating, though, we found that the IBW damping rate and the PDI growth rate are of the same order. This implies that the IBW will damp away not far from the antenna. A wave at 50 MHz has a vacuum wavelength of 6 m, too large to propagate in vacuum regions inside the vessel.

8.3.2 RF Probe Measurements of PDI

As shown above in Fig. 8.6, RF spectra typical of PDI have been observed on C-Mod. The data shown were taken during hydrogen minority heating, where the calculated threshold for PDI is only exceeded near the antenna. The peak power in the decay wave signal as picked up by the probe is 40 dB lower than the pump wave. This does not account for variation in probe response due to frequency, wave number, or electrostatic vs. electromagnetic waves.

However, there is a regime where the RF probe data are interesting, though we

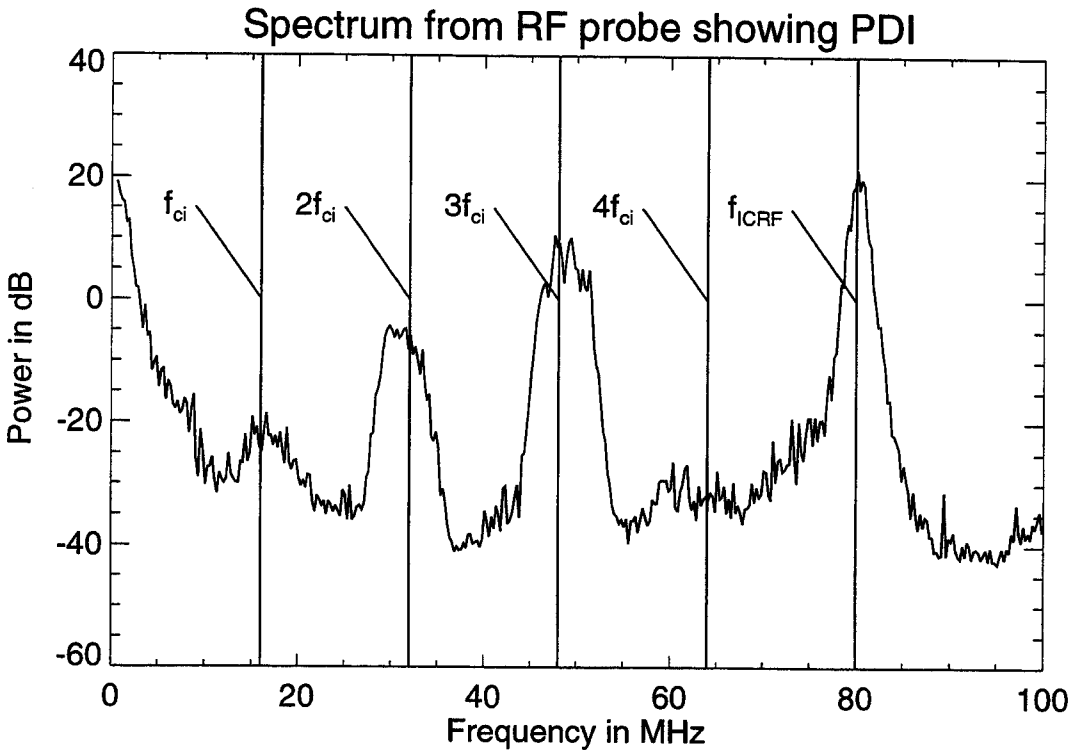

Figure 8.7: RF spectrum from RF probe, showing spectrum typical of PDI. B_0 is 2.7 T, and deuterium cyclotron frequency is 16 MHz at probe position

do not expect a strong correlation with PCX data. As we have shown above, the threshold in RF field for PDI is very low when $\omega_{rf} = \ell\omega_{ci}$, $\ell = 2, 3 \ldots$, in which cases the central RF absorption is also low. When central absorption is low, the RF fields in the plasma edge are higher, high enough so that they are above the PDI threshold all around the torus.

As described in Sec. 8.2.2, we calculate large growth rates for decay into a quasimode at ω_{cH} and an IBW near a multiple of ω_{cD}. The growth rate is large even at low electric fields. For example, if $\omega_{rf} = 5\omega_{cD}$ in the plasma edge, then the largest growth is for decay into a quasimode at $\omega_{cH} = 2\omega_{cD}$ and an IBW at $3\omega_{cD}$. A spectrum taken with RF probes at such a field (Fig. 8.7) shows these peaks.

Considering the conclusions made above from the calculations above, there is no reason to expect that parametric decay causing the observed edge ion tails would be observable by the current set of RF probes. However, the spectra taken with a

cyclotron resonance at the probe support the conclusions from the calculations above.

8.4 Conclusions

In trying to explain the source of the edge ion heating, we must look for waves that will damp strongly on the ions and drive tails in the direction perpendicular to the magnetic field. Parametric decay into a large $\vec{k}$ mode at an ion cyclotron frequency and another wave generates such a heavily damped mode.

Using parameters appropriate for the plasma in the outer SOL at the outboard midplane during hydrogen minority heating, we found that PDI will be convectively unstable at RF electric fields of approximately 100 kV/m. Experimentally, we observe edge ion tails during hydrogen minority heating only if the voltage on at least one of the RF antenna is above 20 kV, which corresponds to a near-field RF electric field of about 100 kV/m.

The PDI threshold depends strongly on plasma temperature, and the experiments showed large changes in edge heating with H-mode transitions, which cause rapid changes in the temperature in the SOL. The fast change (< 1 ms) in the ion tails at the time of the transition into ELM-free H-mode implies that the edge plasma itself changes on the same time scale.

When the toroidal field is changed so that the RF frequency is at a deuterium cyclotron harmonic in the plasma edge, the threshold for PDI drops to very low values, well below 10 kV/m, which corresponds to an RF power of 10 kW. Similarly, the experimental data show the largest energetic neutral flux when the RF is near a harmonic in the edge. The PDI growth rates also predict that deuterium should be heated if the third harmonic is in the edge, and predominantly hydrogen heated if the fourth harmonic is in the edge. This is also reproduced by the PDI growth calculations. Therefore, we conclude that the observed edge ion heating is explained

by parametric decay in the RF antenna near field.

Chapter 9

Summary and Conclusions

The Alcator C-Mod tokamak has proved to be a powerful and versatile machine upon which to study edge ion heating due to ion cyclotron resonance frequency heating. In particular, the good energy resolution of the neutral particle analyzer and its ability to scan poloidally and toroidally allowed measurements that had not previously been available in the study of this effect.

There were two goals of our study of edge ion heating on C-Mod. The first was to determine what other, possibly detrimental, consequences the edge ion heating might have on the plasma. The second was to to explain the source of the energetic edge ions in terms of plasma physics.

9.1 Effects of Edge Heating

Experiments were performed to determine whether edge ion heating increased the impurity level in the plasma, reduced the ability of the RF antenna to couple power to the plasma, or served as a loss channel reducing the RF power reaching the center of the plasma.

We chose a regime where the edge heating was large but the RF power level was low, thus minimizing any effects of the RF not directly connected with edge ion

heating.

Indications of impurity rise were searched for in measurements of molybdenum levels and radiated power. No changes in these were observed to correlate with edge ion heating.

On the same shots, measurements of the RF system were examined for changes in the RF coupling due to the edge heating. RF coupling, measured as loading resistance of the plasma, was unaffected by edge heating.

To estimate the power being lost into the edge ions, we performed scans in pitch angle to find the distribution of the fast ions. Combined with knowledge of the orbits and confinement of these ions, we determined that the maximum RF power lost to the edge is less than a few percent of the total injected RF power, and much less than this in standard RF heating schemes.

We conclude that there are no detrimental effects to Alcator plasmas caused by edge ion heating.

9.2 Parametric Decay Instability as Cause of Edge Heating

Our broad data set includes measurements taken during dedicated experiments as well as observations across the wide span in parameters at which Alcator is operated. This gives us a broad base of observations to compare to known or expected causes of edge heating.

Parametric decay instabilities, in particular decay of the RF heating wave into an ion Bernstein wave and an ion cyclotron quasimode, can produce perpendicular ion tails, resulting in parasitic power loss to the plasma edge.

We calculated the parametric decay growth rates at parameters corresponding to the plasma edge during hydrogen minority heating to find the threshold for the decay.

The RF electric field threshold calculated for parametric decay is approximately the same as the electric field near the antenna at the experimentally observed threshold for edge ion heating. The decrease in the calculated threshold as electron temperature decreases explains the increased edge heating observed during ELM-free H-modes. This work is the first report of the effect of H-modes on edge ion heating by PDI.

Theoretically, parametric decay with large growth at very low RF power was found when the RF frequency is near a cyclotron harmonic in the plasma edge. This agrees with experimental results, where we found large edge heating at these magnetic fields at low RF power. At odd harmonic numbers, the decay modes are expected theoretically to damp strongly on deuterium, and damp strongly on hydrogen at even harmonics, matching experimental observations.

Because of these correspondences, we are convinced that the edge ion heating observed is due to parametric decay instabilities.

9.3 Comparison with Results of other Machines

9.3.1 Impurities

Experiments on JT-60 showed a correlation between parametric decay instability with edge ion heating and increased impurity levels[41]. Specifically, the magnitude of the IBW decay mode was correlated with the impurity radiation as parameters were varied. The PDI was only observed with the antennas at (0,0) phasing.

On Alcator C-Mod, we have found that there is no increase in radiated power and no other indication of increased levels of impurities associated with edge heating. The simplest explanation of this apparent discrepancy may be the cliche "Correlation does not imply causality." The plasma edge effects with (0,0) phasing are significantly different for similar RF power levels at (0,π) phasing[40]. Certain conditions in the edge, such as large poloidal electric fields, may be independently responsible for both

the impurity production and the PDI. The JT-60 results do not include an estimate of the RF power going into edge heating. It is possible that, in their machine, a much larger percentage of RF heating power went into edge heating. Greater power going into the edge could result in greater impurity production.

9.3.2 Parametric Decay Instabilities

Results from ASDEX[39] included RF probe spectra and calculations of the PDI threshold. PDI was observed with RF probes only at certain values of B_0, specifically at fields such that

$$\omega_{rf} = \ell\omega_{cD} \quad \ell = 4, 5, 5.5, 6$$

in the edge. Their calculated growth rates were marginal for instability, $\gamma L/v_g \sim 1{-}3$. In Sec. 8.2.2 we found very large PDI in similar conditions by considering the modes driven unstable by the ion-ion coupling ($\mu_D - \mu_H$). This was neglected in their analysis, and would provide high growth rates for the cases where a harmonic is in the edge.

Conclusions from our experiments are supported by results of the parametric decay experiments on DIII-D[42]. Parametric decay was observed only during limited discharges, and not in diverted discharges. On DIII-D, diverted plasmas have a much less dense edge ($n_e = 5 \times 10^{15}$ m^{-3}) than limited plasmas ($n_e = 1 \times 10^{18}$ m^{-3}). While the ICRF heating in these experiments is 36 MHz, vs. 80 MHz on C-Mod, the trend in Fig. 8.3, a large increase in threshold at lower densities, can explain why PDI disappeared in diverted plasmas on DIII-D. This points out the importance of the plasma density in estimating the effect of PDI on future machines.

9.3.3 Parasitic Power Loss

In plasma discharges on TEXTOR with and without PDI, the total RF power deposited directly into the edge is estimated to be at most 5% during ICRF heating[40]. Because the percentage is not affected by the presence of PDI, they concluded that the power lost via PDI is significantly less than this.

The ion Bernstein wave heating experiments on DIII-D, however, showed approximately 50% of the RF power being deposited in ions in the plasma edge[42]. This value was calculated from measurements made with a neutral particle analyzer similar to the one on Alcator.

The C-Mod results are similar to those on TEXTOR, showing negligible amounts of parasitic power loss.

9.4 Open Questions

Measurements of the fields of the pump and decay waves in front of the antenna would make it tractable to study the relationship between the magnitudes of the edge ion heating and the RF fields, and possibly connect the results to a theory predicting saturation levels of the instability. Understanding the mechanisms setting the saturation level of PDI is necessary to predict theoretically the effect of edge ion heating.

The details of the damping of the quasimode on the ions, and the resulting changes in the distribution function, should be calculated. The results could be compared to our data, and would be useful in predicting the effects of edge heating in new regimes.

In the parametric decay growth calculations, effects of collisions, scattering, and the three-dimensional geometry on propagation and damping of the ion Bernstein wave should be included.

Appendix A

Magnitude of RF Electric Field in Propagating Fast Wave

The magnitude of the RF electric field in the propagating wave can be estimated using the the RF power flux, the wave number, and the polarization. We will use the equations describing the fast wave to express the Poynting flux in terms of known parameters and the electric field in the plasma.

The first step is to determine the perpendicular wave number of the fast wave. Assuming $\vec{k} = k_x\hat{x} + k_z\hat{z}$, $\vec{B}_0 \parallel \hat{z}$, the dispersion relation for the fast wave can be written[1][12]

$$M_\perp^2 = A - M_\parallel^2 + \frac{A(1-A)}{A - M_\parallel^2} \tag{A.1}$$

with the definitions

$$M_\parallel^2 \equiv \frac{V_A^2}{(\omega_{rf}/k_\parallel)^2} = \left[\frac{k_\parallel}{\omega_{rf}}\frac{B^2}{\mu_0 mn}\right]^2, \tag{A.2}$$

[1]Stix's unusually defined $N_\perp$, $N_\parallel$ are here written as $M_\perp$, $M_\parallel$

$$M_\perp^2 \equiv \frac{V_A^2}{(\omega_{rf}/k_\perp)^2} = \left[\frac{k_\perp}{\omega_{rf}}\frac{B^2}{\mu_0 mn}\right]^2, \tag{A.3}$$

and

$$A = \frac{\omega_{ci}^2}{\omega_{ci}^2 - \omega^2}.$$

The value of $k_\parallel$ for the launched wave is 11 m^{-1}, as set by the structure of the antenna. Using $n_e = 10^{20}$ m^{-3}, $B_0 = 5.3$ T at R_0, and $k_\parallel = 11$ m^{-1} in Eq. A.2, we find a value for

$$M_\parallel^2 \simeq 4 \times 10^{-4} \ll 1.$$

Neglecting terms of order $M_\parallel^2$, the dispersion relation, Eq. A.1, becomes

$$M_\perp^2 = 1. \tag{A.4}$$

Using the above parameters in Eq. A.3 and solving Eq. A.4, $k_\perp \simeq 65$ m^{-1}.

The next term needed is the polarization of the electric field, $\vec{E}$, which is given by[12]

$$\frac{E_x + iE_y}{E_x - iE_y} \simeq \frac{\frac{\omega_{ci}}{\omega_{rf}+\omega_{ci}} + M_\parallel^2}{\frac{\omega_{ci}}{\omega_{rf}-\omega_{ci}} - M_\parallel^2}. \tag{A.5}$$

Neglecting $M_\parallel^2$ compared to unity, and rearranging terms

$$\frac{E_x}{E_y} = \frac{i\omega_{rf}}{\omega_{ci}}. \tag{A.6}$$

The parallel component of the electric field, E_z, is shorted out by electron motion, resulting in $E_z \ll E_x$[12].

Substituting for B from Faraday's law and neglecting E_z, the time averaged Poynt-

ing vector is given by

$$\vec{P} = \frac{1}{2\mu_0} \mathrm{Re}\, \vec{E} \times \vec{B} = \frac{1}{2\mu_0} \mathrm{Re} \left[\vec{E} \times \left(\frac{1}{\omega_{rf}} \vec{k} \times \vec{E} \right) \right] = \frac{1}{\mu_0 \omega_{rf}} (E_y^2 k_x \hat{x} + |E|^2 k_z \hat{z}). \tag{A.7}$$

The surface area of each antenna is roughly 0.25 m^2. Using the values obtained above for $\vec{k}$ and the polarization, Eq. A.7 allows us to calculate that the electric field in the propagating part of the plasma is approximately 12 kV/m at an RF power of 500 kW.

Appendix B

Ponderomotive Force in a Magnetized Plasma

Here we derive the ponderomotive force exerted on an ion in a radio-frequency electric field in a magnetized plasma. Because we are concerned with the motion of ions in the near field of a RF antenna, the RF component of the magnetic field is assumed to be smaller than the electric field. For simplicity, we assume that $\vec{E}(\vec{r}_0, t) = E_x \cos(\omega t)\hat{x}$ and $\vec{B}_0 = B_0\hat{z}$. Thus the result is not completely general, but is applicable to the situation of interest. The standard derivation for the ponderomotive force in an unmagnetized plasma is followed[60].

First, the electric field is expanded about the particle guiding center, so

$$\vec{E}(\vec{r}_0 + \vec{r}_1, t) \simeq \vec{E}(\vec{r}_0) + (\vec{r}_1 \cdot \vec{\nabla})\vec{E} + \ldots \tag{B.1}$$

The position of the particle is $\vec{r} = \vec{r}_0 + \vec{r}_1$.

The Lorentz force law is split, using $(\vec{r}_1 \cdot \vec{\nabla})$ as an order parameter (using "dots", as in $\dot{\vec{r}}$, to refer to time derivatives), we find

$$m\ddot{\vec{r}}_1 = q\vec{E}(\vec{r}_0, t) + q(\dot{\vec{r}}_1 \times B_0) \tag{B.2}$$

as the first order in the expansion, and

$$m\ddot{\vec{r}}_2 = q(\vec{r}_1 \cdot \vec{\nabla})\vec{E}(\vec{r},t) + q(\dot{\vec{r}}_2 \times B_0) + q(\dot{\vec{r}}_1 \times B_1(\vec{r}_0,t)) \tag{B.3}$$

as the second order equation.

The solution to Eq. B.2 is

$$\vec{r}_1 = \frac{-qE_x}{\omega^2 - \omega_c^2}\left(\cos(\omega t)\hat{x} - \frac{\omega_c}{\omega}\sin(\omega t)\hat{y}\right), \tag{B.4}$$

as can be easily verified by substitution into Eq. B.2.

This equation for $\vec{r}_1$, and hence $\dot{\vec{r}}_1$, can be substituted into Eq. B.3. Also, for $\vec{E}(\vec{r},t) = \vec{E}(\vec{r})\,\cos(\omega t)$, Faraday's law tells us that

$$\vec{B}_1(\vec{r},t) = -\left(\vec{\nabla} \times \vec{E}(\vec{r})\right)\frac{\sin(\omega t)}{\omega}.$$

The drift due to the ponderomotive force occurs over many wave periods, $\tau = 1/\omega$, so Eq. B.3 can be averaged over a period ($\langle \ldots \rangle$) to show only the drift motion. Only terms proportional to $\cos^2(\omega t)$ or $\sin^2(\omega t)$ survive the averaging, as $\langle \cos(\omega t)\sin(\omega t)\rangle = 0$. Upon averaging,

$$\left\langle (\vec{r}_1 \cdot \vec{\nabla})\vec{E}(\vec{r})\cos(\omega t)\right\rangle = \frac{-qE_x}{2(\omega^2 - \omega_c^2)}\frac{\partial E_x}{\partial x} \tag{B.5}$$

and

$$\left\langle \dot{\vec{r}}_1 \times B_1(\vec{r}_0,t)\right\rangle = \frac{-qE_x}{2(\omega^2 - \omega_c^2)}\frac{\partial E_x}{\partial y}. \tag{B.6}$$

These two terms have dimensions of force, and we define this as the ponderomotive

force,

$$\vec{F}_P = \frac{-q^2}{4m(\omega^2 - \omega_c^2)} \vec{\nabla}_\perp (E^2). \tag{B.7}$$

Substituting in for the period-averaged term, we can rewrite Eq. B.3 as

$$m\ddot{\vec{r}}_2 \simeq \vec{F}_P + q(\dot{\vec{r}}_2 \times \vec{B}_0). \tag{B.8}$$

To get this, we must assume that the wave frequency and the cyclotron frequency are somewhat separable. The solution to Eq. B.8 is

$$\vec{r}_2 = \rho\big(\cos(\omega_c t + \phi)\hat{x} + \sin(\omega_c t + \phi)\hat{y}\big) + \frac{\vec{F}_P \times \vec{B}_0}{qB_0^2} t, \tag{B.9}$$

as is easily shown by substitution.

Appendix C

Near Field of RF Antenna

C.1 Vacuum Field

It is possible to calculate the near field of the antenna in the absence of plasma. By definition, we will be interested in regions much less than a wavelength from the antenna. The height of the antenna, about half a meter, is also much less than the vacuum wavelength, which is 3.75 meters at 80 MHz.

Starting from Maxwell's equations,

$$\vec{\nabla} \times \vec{E} = -\frac{\partial \vec{B}}{\partial t} \qquad \text{and} \qquad \vec{\nabla} \times \vec{B} = \frac{1}{c^2}\frac{\partial \vec{E}}{\partial t} + \mu_0 \vec{j}, \tag{C.1}$$

we solve in terms of $\vec{E}$ and $\vec{j}$. Assuming zero charge density in space, the solution is

$$\nabla^2 \vec{E} + \frac{\omega^2}{c^2}\vec{E} = \frac{1}{\mu_0}\frac{\partial \vec{j}}{\partial t}. \tag{C.2}$$

In the near field, scale lengths are small compared to the wavelength of a propagating wave (by definition), so the second term on the left hand side may be neglected,

leaving

$$\nabla^2 \vec{E} = \frac{1}{\mu_0} \frac{\partial \vec{j}}{\partial t}. \tag{C.3}$$

This may be written as the integral equation

$$\vec{E}(x_0) = \frac{\mu_0}{4\pi} \int d^3x \frac{\dot{\vec{j}}}{|\vec{x} - \vec{x}_0|}. \tag{C.4}$$

In the absence of a plasma, the current density is just that in the current strap, and Eq. C.4 can be integrated numerically to find the electric field at any point in space in the near field region.

Specifically, the profile shown in Fig. 2.8 was calculated using a simple model. The current in the current strap was used with the correct 3-D shape, but feeders, the vacuum vessel, and similar structures were neglected. The current strap was broken into 200 objects poloidally and 20 toroidally. The second strap with the opposite phasing is also included, though this had little effect on the profile in the region of interest. The current density was assumed to be a constant in the strap.

C.2 Effect of the Plasma

In the presence of a plasma, the solution cannot be written in a simple integral form, because there are currents in the plasma which must be consistent with the field. The differential equation Eq. C.3 can be written approximately as

$$\nabla^2 \vec{E} - \frac{\vec{E}}{L^2} = \frac{1}{\mu_0} \frac{\partial \vec{j}}{\partial t}. \tag{C.5}$$

The additional term is the electric field due to the currents driven in the plasma.

In a cold unmagnetized plasma, the current is approximately[12]

$$\vec{j}_{pl} = i\omega\epsilon_0 \frac{\omega_{pe}^2}{\omega^2}\vec{E}. \tag{C.6}$$

Using this, we find that

$$L = c/\omega_{pe} \simeq 2 \text{ mm},$$

assuming $\omega = \omega_{rf} = 2\pi 80 \times 10^6 \text{ s}^{-1}$.

In a cold magnetized plasma, the RF current is not purely parallel to the electric field. In the near field, however, the screening by the plasma is mostly due to the RF plasma current driven parallel to $\vec{E}$. Hence, for purposes of estimating the near field when $\vec{E} \perp \vec{B}_0$,

$$\vec{j}_{pl} = i\omega\epsilon_0 \frac{\omega_{pi}^2}{\omega^2 - \omega_{ci}^2}\vec{E}. \tag{C.7}$$

In this case, the scale length is

$$L = \frac{c}{\omega_{pi}}\left(1 - \frac{\omega_{ci}^2}{\omega^2}\right)^{1/2}.$$

For $n = 1 \times 10^{19} \text{ m}^{-3}$ and B_0 of 5.3 T, $L \simeq 8$ cm.

This term E/L^2 is the screening of the electric field by the plasma. Thus the edge plasma screens out RF fields parallel to $\vec{B}_0$ very efficiently, but perpendicular RF fields are unaffected on the relevant edge scale lengths.

To determine the near field of the RF antenna in the poloidal direction, we use Eq. C.4 with no corrections for the effects of the plasma.

Bibliography

[1] CONN, R. W., Magnetic fusion reactors, in TELLER, E., editor, *Fusion*, volume 1, Part B, pp. 194–410, Academic Press, New York, 1981.

[2] PORKOLAB, M., Radio-frequency heating of magnetically confined plasma, in TELLER, E., editor, *Fusion*, volume 1, Part B, pp. 151–193, Academic Press, New York, 1981.

[3] KUNKEL, W. B., Neutral beam injection, in TELLER, E., editor, *Fusion*, volume 1, Part B, pp. 103–150, Academic Press, New York, 1981.

[4] TAKASE, Y. et al., Plasma Phys. Control. Fusion **38** (1996) 2215.

[5] PERKINS, F. W., IEEE Transactions on Plasma Science **Vol. PS-12, no. 2** (1984) 53.

[6] NOTERDAEME, J.-M. and VAN OOST, G., Plasma Phys. Control. Fusion **35** (1993) 1481.

[7] HUTCHINSON, I. H., *Principles of Plasma Diagnostics*, Cambridge University Press, 1987.

[8] PORKOLAB, M., Fusion Eng. Des. **12** (1990) 93.

[9] FURTH, H. P., The tokamak, in TELLER, E., editor, *Fusion*, volume 1, Part A, Academic Press, New York, 1981.

[10] LABOMBARD, B. et al., J. Nucl. Mater. **241-243** (1997) 149.

[11] LAO, L. L., ST. JOHN, H., STAMBAUGH, R. D., KELLMAN, A. G., and PFIEFFER, W., Nucl. Fusion **25** (1985) 1611.

[12] STIX, T. H., Nucl. Fusion **15** (1975) 737.

[13] LEHRMAN, I. S. and COLESTOCK, P. L., Fusion Eng. Des. **12** (1990) 51.

[14] RYAN, P. M., ROTHE, K. E., WHELATON, J. H., and SHEPARD, T. D., Fusion Eng. Des. **12** (1990) 37.

[15] MURPHY, A. B., Fusion Eng. Des. **12** (1990) 79.

[16] HUTCHINSON, I. H. et al., Phys. Plasmas **1** (1994) 1511.

[17] IRBY, J. H. et al., Rev. Sci. Instrum. **59** (1988) 1568.

[18] MAY, M. L. et al., Rev. Sci. Instrum. **66(1)** (1995) 561.

[19] GOETZ, J. A., LIPSCHULTZ, B., GRAF, M. A., et al., J. Nucl. Mater. **220-222** (1995) 971.

[20] NIEMCZEWSKI, A. P., *Neutral particle dynamics in the Alcator C-Mod tokamak*, PhD thesis, Massachusetts Institute of Technology, 1995.

[21] TOWNER, H. H. et al., Bull. Am. Phys. Soc. **26** (1981) 857.

[22] RICE, J. E., BOMBARDA, F., GRAF, M. A., MARMAR, E. S., and WANG, Y., Rev. Sci. Instrum. **66(1)** (1995) 752.

[23] RIVIERE, A. C., Nucl. Fusion **11** (1971) 363.

[24] ROQUEMORE, A. L. et al., Fusion Eng. Des. **12** (1990) 93.

[25] MILLER, J. C., Calibration and parametric study of the Alcator C-Mod charge exchange neutral particle analyzers, Master's thesis, Massachusetts Institute of Technology, 1995.

[26] COLCHIN, R. J., ROQUEMORE, A. L., and SCOTT, S. D., Rev. Sci. Instrum. **59** (1988) 1667.

[27] STILLERMAN, J. A., FREDIAN, T. W., KLARE, K. A., and MANDUCHI, G., Rev. Sci. Instrum. **68** (1997) 939.

[28] GOLDSTON, R. J. and TOWNER, H. H., Journal of Plasma Physics **26** (1981) 283.

[29] GREENWALD, M., Personal Communication.

[30] HEIDBRINK, W. W. and SADLER, G. J., Nucl. Fusion **34** (1994) 535.

[31] TRUBNIKOV, B. A., Particle interactions in a fully ionized plasma, in LEONTOVICH, M. A., editor, *Reviews of Plasma Physics*, volume 1, p. 105, Consultants Bureau, 1965.

[32] BOIVIN, R., Personal Communication.

[33] KENNEL, C. F. and ENGELMANN, F., Phys. Fluids **9** (1966) 2377.

[34] BUZANKIN, V. V. et al., Magnetosonic-heating experiments in tokamak T-4 plasma, in *Plasma Physics and Controlled Nuclear Fusion Research 1976 (Proc. 6th Int. Conf. Berchtesgaden, 1976)*, volume 3, p. 61, Vienna, 1977, IAEA.

[35] KAITA, R. et al., Nucl. Fusion **23** (1983) 1089.

[36] HAMMETT, G. W., *Fast ion studies of ion cyclotron heating in the PLT tokamak*, PhD thesis, Princeton University, 1986.

[37] NOTERDAEME, J.-M. et al., The role of the Faraday screen in ICRF antennae, in *European Conference on Controlled Fusion and Plasma Heating*, volume 10C part I, p. 137, European Physical Society, 1986.

[38] WESNER, F., PROZESKY, V. M., BEHRISCH, R., and STAUDENMAIER, G., Fusion Eng. Des. **12** (1990) 193.

[39] VAN NIEUWENHOVE, R., VAN OOST, G., NOTERDAEME, J.-M., et al., Nucl. Fusion **28** (1988) 1603.

[40] VAN OOST, G. et al., Fusion Eng. Des. **12** (1990) 149.

[41] FUJII, T. et al., Fusion Eng. Des. **12** (1990) 139.

[42] PINSKER, R. I., PETTY, C. C., MAYBERRY, M. J., PORKOLAB, M., and HEIDBRINK, W. W., Nucl. Fusion **33** (1993) 777.

[43] TAKASE, Y., PORKOLAB, M., SCHUSS, J. J., et al., Phys. Fluids **28** (1985) 983.

[44] PORKOLAB, M. et al., Phys. Rev. Lett. **38** (1977) 230.

[45] ASDEX Team, Nucl. Fusion **29** (1989) 1959.

[46] SNIPES, J. A. et al., Plasma Phys. Control. Fusion **38** (1996) 1127.

[47] LABOMBARD, B. et al., Phys. Plasmas **2** (1995) 2242.

[48] STANGEBY, P. C. and MCCRACKEN, G. M., Nucl. Fusion **30** (1990) 1225.

[49] COLESTOCK, P., GREENE, G. J., HOSEA, J. C., et al., Phys. Plasmas **12** (1990) 43.

[50] PORKOLAB, M., Plasma heating by fast magnetosonic waves in tokamaks, in *Advances in Plasma Physics, Thomas H. Stix Symposium*, number 314 in AIP Conference Proceedings, p. 99, Princeton, NJ, 1992, American Institute of Physics.

[51] D'IPPOLITO, D. A. and MYRA, J. R., Phys. Plasmas **3** (1996) 420.

[52] TAKASE, Y. et al., Phys. Rev. Lett. **59** (1987) 1201.

[53] SKIFF, F., ONO, M., COLESTOCK, P., and WONG, K. L., Phys. Fluids **28** (1985) 2453.

[54] OKADA, H., ABE, H., ITATANI, R., and ONO, M., Phys. Fluids **29** (1986) 489.

[55] ONO, M., PORKOLAB, M., and CHANG, R. P. H., Phys. Rev. Lett. **38** (1977) 962.

[56] SKIFF, F., ONO, M., and WONG, K. L., Phys. Fluids **27** (1984) 2205.

[57] BERNSTEIN, I. B., Phys. Rev. **109** (1958) 10.

[58] PORKOLAB, M., Parametric instabilities and anomolous absorption and heating of plasmas, in *Symposium on Plasma Heating and Injection*, p. 46, Varenna, Italy, 1972.

[59] REARDON, J. et al., Bul. Am. Phys. Soc. **41** (1996) 1549.

[60] CHEN, F. F., *Introduction to Plasma Physics and Controlled Fusion*, Plenum Press, 1984.